Memoirs of the Faculty of Science, Kyoto University, Series of Physics, Astrophysics, Geophysics and Chemistry, Vol. XXXIV, No. 1. Article 4, 1972.

DIFFERENTIAL CROSS SECTIONS FOR THE PROCESS $\gamma+n\rightarrow\pi^{\circ}+n$ AT PHOTON ENERGIES BETWEEN 500 AND 900 MeV

By

Hideki OKUNO*

Department of Physics, Faculty of Science, Kyoto University

(Received March 12, 1971)

ABSTRACT

The differential cross sections for the process $\gamma+n\rightarrow\pi^{\circ}+n$ have been measured at six pion center of mass angles; 45°, 60°, 90°, 105°, 120° and 140°. Values were obtained with a liquid deuterium target at intervals of 50 MeV from approximately 500 MeV to 900 MeV for incident photon energies.

To determine the kinematics of the above process completely, the momenta of both π° mesons and recoil neutrons were measured accurately. π° mesons were detected with a pair of photon detectors, each of which consisted of a lead glass Cerenkov counter and a lead sandwiched spark chamber. Neutrons were detected with an array of 16 plastic scintillation counters and their flight times were measured.

The obtained data were compared with the result of the phenomenological partial wave analysis by Walker. On the whole, angular distributions around the second resonance could be well fitted by Walker's resonance parameters. And these support the conclusion that D_{13} (1520) resonance can be excited from nucleons mainly by isovector photons. As for P_{11} (1470), no remarkable enhancement of the cross section was found for the process $\gamma+n\rightarrow\pi^{\circ}+n$.

TABLE OF CONTENTS

* Now at Institute for Nuclear Study, University of Tokyo, Tokyo.

I. Introduction

I–1. *General*

The photoproduction of single pions from nucleons has long been a fruitful source of informations about the pion-nucleon and the photon-nucleon interactions. Many experimental and theoretical investigations of the photoproduction processes have been performed in the pion-nucleon resonance regions ($E_\gamma < 1.5$ GeV). And their results have provided useful knowledges to the models of elementary particles such as a SU (3) symmetry, a quark model, and a current algebra. The purpose of this experiment on the photoproduction of neutral pions from neutrons is to offer the informations for clarifying the isospin character of the photoproduction amplitudes.

Among four processes of the single pion photoproduction from nucleons;

$$\gamma + p \longrightarrow \pi^+ + n \qquad (\pi^+ n) \qquad (1)$$
$$\gamma + p \longrightarrow \pi^\circ + p \qquad (\pi^\circ p) \qquad (2)$$
$$\gamma + n \longrightarrow \pi^- + p \qquad (\pi^- p) \qquad (3)$$
$$\gamma + n \longrightarrow \pi^\circ + n \qquad (\pi^\circ n), \qquad (4)$$

the experimental knowledges on the processes (π^+n), (π°p) and (π^-p) have been extensively accumulated. The differential cross sections for the processes (π^+n), (π°p) and (π^-p), the polarizations of the recoil protons for the processes (π°p) and (π^-p), and the polarized photon asymmetry for the processes (π^+n) and (π°p) have been measured and the experimental results until 1966 were complied by Beale, Ecklund and Walker.[1] The data for the proton target processes are more abundant and precise than that for the neutron target processes.[2] Among the neutron target processes, the process (π°n) has been scarcely investigated.[3-6]

The investigations of the neutron target processes can provide the useful imformations on the isospin dependence of the photoproduction amplitude. A matrix element of the electromagnetic interaction for the single pion photoproduction can be decomposed into an isoscalar part S and an isovector part V in the isospin space. Using Watson's formalism,[7] the matrix element for the single pion photoproduction can be written in a general form as;

$$A=M(\tau(t,\ t_3)|S+V|\nu(n,\ n_3))\ , \tag{5}$$

where $\nu(n,\ n_3)$ and $\tau(t,\ t_3)$ are the isospin function of the initial nucleon state and the final pion-nucleon state, respectively. If we define the isoscalar and the isovector amplitudes by the following expressions;

$$A^{\mathrm{S}}=M(\tau(1/2,\ \pm1/2)|S|\nu(1/2,\ \pm1/2)) \tag{6}$$

$$\mp A^{\mathrm{V1}}=M(\tau(1/2,\ \pm1/2)|V|\nu(1/2,\ \pm1/2)) \tag{7}$$

$$A^{\mathrm{V3}}=M(\tau(3/2,\ \pm1/2)|V|\nu(1/2,\ \pm1/2))\ , \tag{8}$$

the amplitude for each pion photoproduction process can be expressed as follows;

$$A^\circ\equiv A(\gamma+\mathrm{p}\rightarrow\pi^\circ+\mathrm{p})=\sqrt{2/3}A^{\mathrm{V3}}+\sqrt{1/3}(A^{\mathrm{V1}}-A^{\mathrm{S}}) \tag{9}$$

$$A^+\equiv A(\gamma+\mathrm{p}\rightarrow\pi^++\mathrm{n})=\sqrt{1/3}A^{\mathrm{V3}}-\sqrt{1/3}(A^{\mathrm{V1}}-A^{\mathrm{S}}) \tag{10}$$

$$A^-\equiv A(\gamma+\mathrm{n}\rightarrow\pi^-+\mathrm{p})=\sqrt{1/3}A^{\mathrm{V1}}-\sqrt{2/3}(A^{\mathrm{V1}}+A^{\mathrm{S}}) \tag{11}$$

$$A^{n\circ}\equiv A(\gamma+\mathrm{n}\rightarrow\pi^\circ+\mathrm{n})=\sqrt{2/3}A^{\mathrm{V3}}+\sqrt{1/3}(A^{\mathrm{V1}}+A^{\mathrm{S}})\ . \tag{12}$$

In these expressions, A^{S} is the isoscalar amplitude which leads to a $T=1/2$ pion-nucleon final state. A^{V1} and A^{V2} are the isovector amplitudes which lead to $T=1/2$ and $T=3/2$ pion-nucleon final states, respectively. These three amplitudes are the function of the energy and the transfered momentum, and depend on the total angular momentum. In partial wave analysis, these complex amplitudes are expanded in several electric and magnetic multipoles.

In order to determine these isospin amplitudes separately, one must investigate all four processes. Especially for the separation of A^{S} and A^{V1}, the measurements on both proton and neutron target processes are necessary.

As is shown in eqs. (6)-(8), $T=3/2$ resonances in the pion-nucleon state can be excited from nucleons by the isovector interaction only. On the other hand, $T=1/2$ resonances can be resulted from both isovector and isoscalar interactions. Our main purpose of this experiment on the π° photoproduction from neutrons is to study the isovector and isoscalar contributions to the photo-excitation of $T=1/2$ pion-nucleon resonances. For the detailed analysis of the electromagnetic structure of nucleon resonances, only the resonance contributions must be extracted from the photoproduction amplitude. The interactions of the initial particles in the neutral pion production are somewhat less complicated than those of charged pion production, because the charged pion photoproduction amplitude contains a pion exchange term (also known as a Born or a retardation term). For the simplicity of the analysis, our efforts were concentrated on the investigation of the neutral pion production processes.

In the energy range below $E_\gamma=1$ GeV, the existence of several pion-nucleon resonances are well known from the pion-nucleon scattering experiments. These are summarized in Table 1.[8] In the single pion photoproduction, some of them, $P_{33}(1236)$, $D_{13}(1520)$, $D_{15}(1670)$ and F_{15} (1688), appeared as prominent peaks in the energy dependence of the total cross section, which are usually called the first, second and third resonances. However two $T=1/2$ resnances, P_{11} (1470) and S_{11} (1535), which were found from the phase shift analysis of the pion-nucleon scattering data, have not been established in the photoproduction process.

Table 1. Summary of the pion-nucleon resonances[8]. Multipoles for the photo-excitation are also presented.

Resonance		Width (MeV)	Elasticity	Multipole amplitude for the photo-excitation	
				CGLN amplitude	Helicity amplitude
	P_{11} (1470)	200 to 400	0.60	E_{1-}, M_{1-}	A_{1-}, B_{1-}
	D_{13} (1520)	105 to 150	0.50	E_{2-}, M_{2-}	A_{2-}, B_{2-}
$T=1/2$	S_{11} (1535)	50 to 160	0.34	E_{0+}	A_{0+}
	D_{15} (1670)	105 to 175	0.42	E_{2+}, M_{2+}	A_{2+}, B_{2+}
	F_{15} (1688)	105 to 180	0.60	E_{3-}, M_{3-}	A_{3-}, B_{3-}
$T=3/2$	P_{33} (1236)	120 ± 2	1.00	E_{1+}, M_{1+}	A_{1+}, B_{1+}
	S_{31} (1650)	130 to 250	0.27	E_{0+}	A_{0+}
	D_{33} (1670)	175 to 300	0.13	E_{2-}, M_{2-}	A_{2-}, B_{2-}

The detailed investigation of the photo-excitation of these resonances from protons and neutrons can play an important role in checking the symmetry theories[9] and current commutator sum rules.[10]

I–2. *Survey of the phenomenological analysis on the single pion photoproduction*

Theoretical analyses of the single pion photoproduction from nucleons have been extensively developed in the resonance regions. The first resonance, P_{33} (1236), has been well established. However, the analyses around the second and third resonances are limited to be phenomenological.

In the low energy region, from the pion production threshold to the first resonance, analyses have been performed by many authors in terms of dispersion relations following Chew, Goldberger, Low and Nambu.[11] This region is dominated by the $P_{33}(1236)$ resonance only, and which is purely elastic. Therefore the photoproduction amplitude is related to the pion-nucleon scattering amplitude and the dispersion relations can be evaluated. Along this line, Schmidt and Hohler,[12] Berends, Donnachie and Weaver,[13] and Kondo *et al.*[14] have been made the detailed evaluation of various multipole amplitudes. In general, the quantitatively good agreements between the experimental results and the theoretical analyses were obtained. The gross feature is that the P_{33} (1236) resonance is excited mostly by the magnetic dipole radiation, M_{1+} and the electric quadrupole amplitude E_{1+} is small. (Hereafter $E_{l\pm}$ and $M_{l\pm}$ denote the electric and magnetic multipole amplitudes leading to the pion-nucleon final states of total angular momentum $J=l\pm1/2$).

Recently, Sanda and Shaw[15] suggested the presence of the isotensor amplitude in the pion photoproduction in the P_{33} (1236) resonance region by analyzing the experimental results on the processes (π^+n) and (π^-p). To clarify these problems, more accurate experimental studies on the neutron target processes are needed. Especially the large effect in the process (π°n) was pointed out by these authors.

In the second resonance region (500 MeV$<E_\gamma<$900 MeV) there are three $T=1/2$ resonances, P_{11} (1470), D_{13} (1525) and S_{11} (1535), which are known to be appreciably inelastic. Therefore the analysis becomes inevitably more phenomenological. A number of analyses of pion photoproduction data have recently been presented. Gourdin and Salin[16] analyzed the processes (π^+n) and (π°p) with an isobar model in the energy region from 200 MeV to 800 MeV. In their analysis, only P_{33} and D_{13} resonances and some background terms were considered. As the experimental data have been accumulated, their theory can not reproduce the differential cross sections in the whole energy region. Yamaki[17] also presented the calculation based on the C.G.L.N. amplitudes and by assuming the phenomenological form on the E_{2-} and M_{2-} amplitudes. His analysis of the process (π°p) suggested that the data were fitted when the Roper's set of πN phase shifts was used and the ratio E_{2-}/M_{2-} was taken to be 5$\sim$3. He also calculated the differential cross section on the process (π°n) by neglecting the isoscalar amplitudes.

Chau, Dombey and Moorhouse[18] (hereafter we will refer to as CDM) also analyzed the processes (π°p) and (π^+n) with the generalized isobar model. Proia and Sebastiani[19] made a phenomenological analysis of the process (π^-p) using the CDM isobar model. Combining the results of CDM, they showed that the isovector part was clearly dominant in the $T=1/2$ resonant amplitude. By separating the photoproduction amplitude into isoscalar and isovector components, they presented the previsions on the process (π°n). Walker[20] also performed the partial wave analysis on the processes (π^+n), (π°p) and (π^-p) phenomenologically. His results also suggested that the most significant and well-determined $T=1/2$ resonance were excited by mainly isovector photons in accordance with the Proia's results.

Recently, Moorhouse and Rankin[21] made re-analysis using the more recent data on the processes (π^+n) and (π°p) based on the scheme of CDM. Their result of the phenomenological analysis on the electromagnetic excitation of the D_{13} (1520) resonance agreed well with the Walker's result. The D_{13} (1520) resonance is excited mostly by the helicity 3/2 amplitude or $E_{2-}/M_{2-}\simeq 3$. Therefore, the second resonance has a small effect on the cross sections at 0° and 180°. As for the P_{11} (1470) and S_{11} (1535) resonances, however, the different conclusions from the Walker's analysis were presented. The solutions of CDM showed large P_{11} contributions both in the processes (π^+n), (π°p) and (π^-p), but Walker found a very small amplitude for the P_{11} resonance. Moorhouse obtained both solutions. The analyses based on the dispersion relations by Berends and Donnachie,[13] and Kondo *et al.*[14] recently suggested a small contribution in both proton and neutron processes. From the present stage of the analysis, the P_{11} (1470) and S_{11} (1535) resonances have not well been established in the photoproduction. The more accurate experimental data, especially on the neutron target processes are necessary in addition to the recoil nucleon polarization, polarized photon asymmetry and polarized target asymmetry.

I–3. *Previous experiment on the π° photoproduction from neutrons*

Previously in order to investigate the isospin character in the pion photoproduction processes, we measured the differential cross sections for the process $\gamma+d\rightarrow\pi^\circ+d$ in the energy range from 500 MeV to 800 MeV.[22] For the elastic pion photoproduction from deuterons, only the isovector photons can contribute to the $T=1$ pion-deuteron final state, because the isospin of the initial deuteron state is 0. From the measurement of this process, we obtained the results that the isovector part was dominant in the D_{13}-wave amplitude of the single pion photoproduction from nucleons around the D_{13} (1520) resonance. In order to obtain the more accurate conclusions, there are some difficulties to be overcome, such as the small cross section and the ambiguity of the deuteron form factor at large momentum

transfers. To evaluate the ratio of the isoscalar amplitude to the isovector amplitude more directly, we proceeded to the experiment on the process $\gamma+n\to\pi^\circ+n$. The preliminary measurement of the above process was carried out at $\theta^c_{\pi^\circ}=90^\circ$ around the second resonance.[6]

In these measurement, because of the poor energy resolution, the definite conclusions could not be extracted.

At other laboratories, the differential cross sections for the process $\gamma+n\to\pi^\circ+n$ have been scarcely measured in the pion nucleon resonance region. Cocconi and Silverman[4] measured the ratio of the π° yield from the deuterium and hydrogen targets at the photon energy of 300 MeV. Clinesmith, Hatch and Tollestrup[4] at Cal. Tech. also measured the π° yield from the deuterium target by detecting two photons from the pion decay at the incident photon energies of 1150 MeV and 1350 MeV. At more high energies, recently Bolon *et al.*[5] at M.I.T. measured the differential cross section for the process $\gamma+n\to\pi^\circ+n$ by detecting both π° mesons and neutrons in coincidence. They obtained four values of the ratio $\frac{d\sigma}{d\Omega}(\pi^\circ n)/\frac{d\sigma}{d\Omega}(\pi^\circ p)$ for $0.2\leq -t\leq 1.6$ (GeV/c)^2 at $E_\gamma=4$ GeV. However no measurements were carried out in the energy region of $300\leq E_\gamma\leq 1000$ MeV, because of the difficulty in the detection of π° mesons and the complexity of the kinematics from the use of the deuterium target.

I–4. *Purpose and brief description of this experiment*

This experiment was aimed to measure the differential cross sections for the process $\gamma+n\to\pi^\circ+n$ in the energy range from 500 to 900 MeV. It was hoped that the accurate measurement of the above process could reveal the isotopic spin dependence of the pion photoproduction amplitudes and contribute to the more profound understanding of the electromagnetic structures of the pion nucleon resonances. Especially in the above energy region, our interest was concentrated on the P_{11} (1470) and D_{13} (1520) resonacnces, which have been established from the pion-nucleon scattering. As for the electromagnetic properties of these resonances, many theoretical predictions based on the quark model and the current algebra have been made, but no definite conclusions have been obtained. Partial wave analyses of the single pion photoproduction have given many valuable informations to these predictions, but the data of the neutron target processes are poor and can not give the critical test for the isospin dependence of the photoproduction.

This paper presents the results of the measurement of the differential cross section on the process $\gamma+n\to\pi^\circ+n$. The data were obtained at $\theta^c_{\pi^\circ}=45^\circ$, 60°, 90°, 105°, 120° and 140° for incident photon energies from 500 MeV to 900 MeV. To achieve the accurate energy resolution, both π° mesons and recoil neutrons were detected and their momenta were precisely measured. The energy and angular resolutions obtained with our apparatuses were $\Delta E=\pm 32$ MeV and $\Delta\theta^c_{\pi^\circ}=\pm 3.5^\circ$ at the incident photon energy of 750 MeV for instance. In order to reduce the absolute cross sections, the dectection efficiencies of the π° detector and of the neutron detector were calibrated by the coincidence measurements of the processes $\gamma+p\to\pi^\circ+p$ and $\gamma+p\to\pi+n$, respectively, using the liquid hydrogen target. The effects due to the internal motion of the target nucleon were also measured with the process $\gamma+d\to\pi^\circ+p+n_s$ using the liquid deuterium target, where s denotes the spectator nucleons. The geometrical detection efficiencies were calculated by the Monte Carlo method, where the spectator model and the Hulthen wave function for the deuteron were assumed. The validities of these calculations and assumptions were checked with the measurement of the processes $\gamma+p\to\pi^\circ+p$ and $\gamma+d\to\pi^\circ+p+n_s$. The cross sections obtained from

the above two processes agreed with each other within the experimental accuracy. It was confirmed that the effect due to the internal motion of the target nucelon inside the deuteron was correctly considered and that the spectator model was valid.

The ratios of the differential cross section for the processes $\gamma+\mathrm{n}\rightarrow\pi^\circ+\mathrm{n}$ and $\gamma+\mathrm{p}\rightarrow\pi^\circ+\mathrm{p}$,

$$R_{00}=\frac{\frac{d\sigma}{d\Omega}(\pi^\circ\mathrm{n})}{\frac{d\sigma}{d\Omega}(\pi^\circ\mathrm{p})}\ , \tag{13}$$

were presented elsewhere.[23]

In this paper, we present the absolute values of the differential cross section for the processes $\gamma+\mathrm{p}\rightarrow\pi^\circ+\mathrm{p}$ and $\gamma+\mathrm{n}\rightarrow\pi^\circ+\mathrm{n}$. The results were also compared with the partial wave analyses by Yamaki, Walker, and Proia and Sebastiani. Some modifications based on the Walker's analysis are also discussed.

II. Experimental Equipments

II–1. *General*

The bremsstrahlung beam used in this experiment was obtained from the 1.3 GeV electron synchrotron at the Institute for Nuclear Study, University of Tokyo. The average intensity of the photon beam was about 10^9 equivalent quanta/sec at the maximum photon energy of 950 MeV. The experiment was performed at the r_2 area as is shown in Fig. 1. As a free neutron target is not available, bound neutrons in a liquid deuterium target were used in this experiment. At photon energies above 500 MeV, proton and neutron in deuterium can be treated as an independent particles. So we measured the following processes;

$$\gamma+\mathrm{d}\rightarrow\pi^\circ+\mathrm{n}+\mathrm{p_s} \tag{14}$$

$$\gamma+\mathrm{d}\rightarrow\pi^\circ+\mathrm{p}+\mathrm{n_s}\ , \tag{15}$$

where subscript s denotes the spectator nucleons. To determine the kinematics of the above processes completely, it is necessary to measure both momenta of the π° meson and the recoil nucleon when the spectator nucleon can not be detected. As is schematically shown

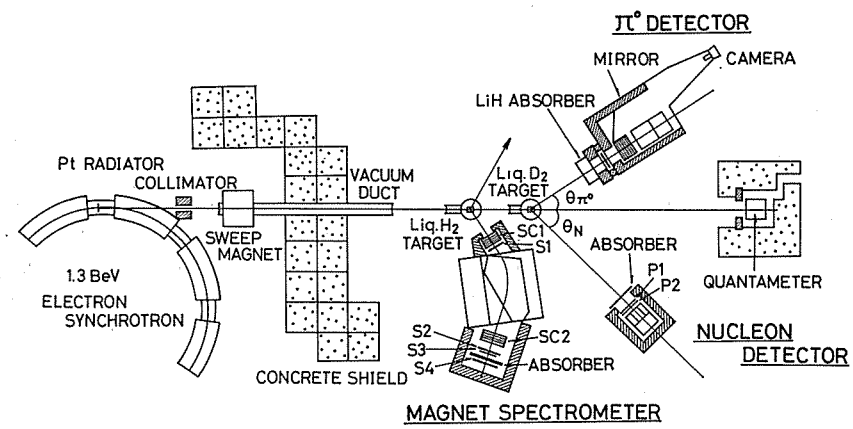

Fig. 1. Plan view of the experimental area. The magnet spectrometer was used for the calibration measurements of the π° detector and the nucleon hodoscope.

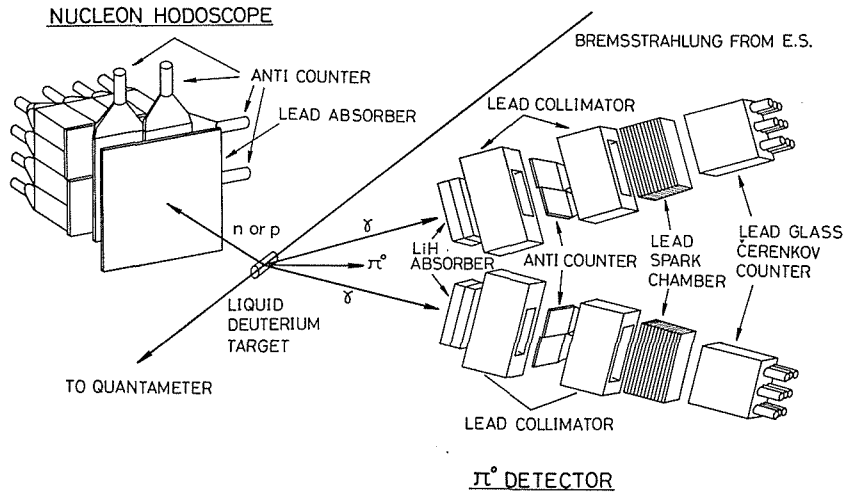

Fig. 2. Schematic arrangement of the experimental apparatuses.

in Fig. 2, the π° meson produced at the deuterium target was detected by observing two decay photons with a pair of photon detectors. Each photon detector consisted of a total absorption type lead glass Cerenkov counter,[24] a lead-sandwiched spark chamber, a veto-counter and a LiH absorber.

The recoil nucelon, the proton and the neutron, was detected with a plastic scintillation hodoscope which consisted of 16 modules (each module was $10\times10\times20$ cm^3). Discrimination between the proton and the neutron was carried out with two layers of thin plastic scintillation counters placed before the hodoscope. The flight time of the recoil nucleon was measured to obtain its kinetic energy. To achieve the accurate time resolution, the pulse height compensation device was used, and the resultant time resolution amounted to ±0.5 ns (FWHM) for both neutrons and protons.

When the coincidence between the π° detector and the nucleon hodoscope occured, the informations on the pulse heights, the flight time and the address of the nucelon hodoscope were stored event by event in the data processor PDP-5, and the lead spark chambers were triggered.

II-2. *Photon beam*

When the synchrotron magnetic field is reached to its maximum value and the accelerating R.F. voltage is turned off, the circulating electrons in the synchrotron magnetic field strike the platinum radiator of 50μ thick at 20 mm apart from the central orbit. This collision produces a bremsstrahlung photon beam in the direction of the electron motion. The platinum radiator was placed at the straight section S5. The beam spill time was usually kept to be about 4 ms by controlling the damping of the R.F. voltage. To reduce the bunching of the beam, the oscillating frequency modulation was applied on the R.F. voltage. The electron energy E_0 was obtained from the radial position of the radiator and the value of the magnetic field in the synchrotron at the time of collision. The latter quantity was reduced from the value of the current exciting the synchrotron magnet. The spread of the field strength during the collision was estimated to be about 1%, therefore the same for the energy spread. The correspondence between the maximum photon energy and the exciting current of the synchrotron magnet was measured with a pair spectrometry by Takamatsu *et al.*[25] for the

energies from 200 MeV to 1200 MeV. The uncertainties of the maximum photon energies depend, mainly, on the accuracy of reading the current meter, and the estimated uncertainty was about ± 5 MeV. The stability of the synchrotron magnetic field was $\pm 0.1\%$.

The photon beam was collimated into a circular shape with a lead collimator of 5 mm in diameter which was placed at 2.5 m apart from the internal radiator. It then passed through a sweep magnet whose field strength was about 7 kG and the charged particles were swept away. At the position of the target, 14 m downstream from the radiator, the beam as defined by the collimator was 25 mm in diameter. The beam profile was observed on a Polaroid film and the intensity distribution was measured with a X-ray film.

The intensity of the photon beam was continuously monitored with a Wilson-type quantameter. The absolute value of the calibration constant was measured recently by Miyachi *et al.*[26] using a Faraday cup as an absolute electron monitor. The values thus obtained agreed well with the Wilson's constant of 4.79×10^{18} MeV/coulomb within the experimental accuracy of 3%.

The common unit of the beam is the MU (monitor unit). A MU is the amount of the beam necessary to produce the output of 5.00×10^{-7} coulomb from the quantameter. The total energy of the photon beam is obtained from the collected charges q in the quantameter as follows;

$$\begin{aligned} U(\mathrm{MeV}) &= 4.79\times 10^{18}\times q\ (\mathrm{coulomb}) \\ &= 2.40\times 10^{12}\times \mathrm{MU}\ . \end{aligned} \tag{16}$$

An equivalent quanta Q is obtained from the following equation;

$$Q=\frac{U(\mathrm{MeV})}{E_0(\mathrm{MeV})}\ , \tag{17}$$

where E_0 is the maximum energy of the bremsstrhlung spectrum.

II–3. *Liquid hydrogen and deuterium target*

The liquid hydrogen and deuterium target used in this experiment was the INS–3 target, whose details were described by Kitami *et al.*.[27] The apparatus mainly consists of a vacuum

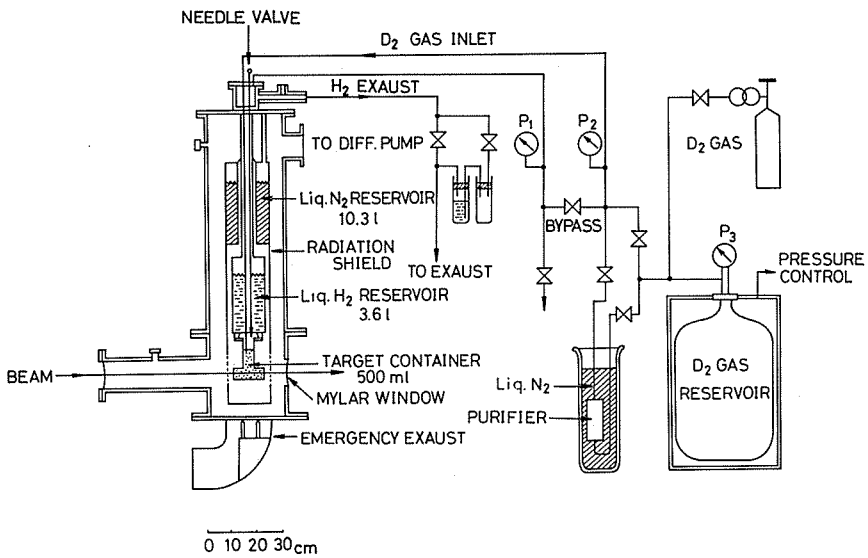

Fig. 3. Liquid hydrogen and deuterium target.

jacket, a liquid nitrogen reservoir, a liquid hydrogen reservoir and a target container (or an appendix) as is shown in Fig. 3. For the hydrogen target operation, liquid hydrogen in the liquid hydrogen reservoir was supplied into the target container through the needle valve. On the otherhand, for the deuterium target operation, deuterium gas in the gas reservoir was liquefied by passing through liquid hydrogen.

The target container was a cylindrical shape of 50 mm in diameter. The length of the container was measured to be 103 mm. The thickness of the Mylar cup holding liquid hydrogen and deuterium was 125 μ. Also the thickness of the Mylar window of the vacuum jacket was 250μ, through which photon beam entered and left. Liquid hydrogen in the target container was usually kept at an atomospheric pressure, and their density was 0.0707 g/cm. On the otherhand, liquid deuterium was kept nearly at liquid hydrogen temperature of 20.4 °K because of the close thermal contact to the liquid hydrogen reservoir. The temperature of the liquid deuterium was obtained by observing the vapour pressure of liquid deuterium. The density of liquid deuterium at 20.4 °K is 0.169 g/cm^3.[28] The background runs were taken with the target container evacuated down to the order of 10^{-3} mmHg with the rotary vacuum pump.

II–4. *π° meson detection system*

(a) Principle

The π° meson was detected by observing two decay photons with a pair of photon detectors. Perspective view of photon detectors is shown in Fig. 2. With the total absorption Cerenkov counter[28] and the lead spark chamber, the energies and the correlation angle for the two decay photons from the π° were measured. The informations on the pulse height of the Cerenkov counter and the correlation angle between two decay photons made it possible to evaluate the energy and production angle of the π° meson with large precision.

The π° meson decays into two photons isotropically at its rest system. At the laboratory system, the decay photons concentrate to the minimum correlation angle $\varphi_{\min}$, which is given by,

$$\sin\left(\frac{\varphi_{\min}}{2}\right)=\frac{\mu}{E}\,, \tag{18}$$

where μ and E denote the rest mass and the total energy of the π° meson, respectively. Therefore, two photon detectors were placed symmetrically for the flight direction of the π° meson, and the opening angle of these detectors was set to the minimum correlation angle.

The π° momentum reduction was carried out with the method discussed by Tau.[29] The details are described in IV–3.

(b) Lead-sandwiched spark chamber

Construction of the lead-sandwitched spark chambers is shown in Fig. 4. Chambers consisted of 12 units, and among them 10 layers of lead converters (1 mm thick each) were distributed as is shown in Fig. 4. Total thickness of the lead converter was 2 in radiation length, and about 70% of photons with energy around 250 MeV can be converted into electron-positron pairs in the spark chamber. Plates of each chamber were made of 50 μ aluminium sheets and were separated by a Lucite frame. A gap width of the chamber was 1 cm and the useful area was 25 cm $\times$ 25 cm. Between the aluminium plate and the lead converter, thin (75 μ) Mylar film was placed to suppress the electrical discharges.

Helium gas continuously flowed parallel through each chamber at the total flow rate of 100 ml/min. A clearing fiield of 80 V/cm was applied to obtain the shorter sensitive time. High voltage pulses of 12.5 kV in height and 1.2 μs in width were obtained with a nitrogen-

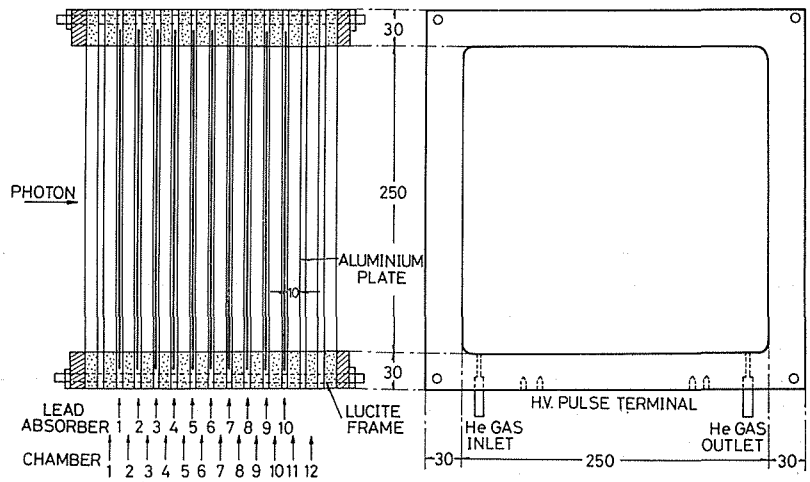

Fig. 4. Mechanical construction of the lead-sandwiched spark chamber. The thickness of the lead converter is 1mm each. The gap width of each unit chamber is 10 mm.

filled spark gap, which was triggered by an output from a Krytron pulser. The delay time of the triggering pulse after the particle passage through the chamber was measured to be 200 ns, and under these conditions the sensitive time of 1 μs was obtained.

Stereoscopic views (top and side) of the spark chamber were photographed on one frame with an Automax high speed camera, which was located at the rear of the photon detector. The image of the entire spark chamber arrangement was reflected to the camera with a 40 cm$\times$70 cm mirror. A system of fiducials, which was scribed on Lucite plates over the chambers, was used to determine spark positions from the measurements of spark and fiducial images on the film. A set of "indication lamps" was displayed on each frame to identify the frame number, the run number and the chamber number.

When the fast pion-nucleon coincidences occurred, the spark chambers were triggered. At the same time, indicator lamps were fired and flash lamps illuminated the fiducials. And after a photograph of the spark chamber was taken, the film was advanced at the rate of 22.5 ms per one frame.

(c) Lead glass Cerenkov counter[24]

A mechanical construction of the total absorption lead glass Cerenkov counter is

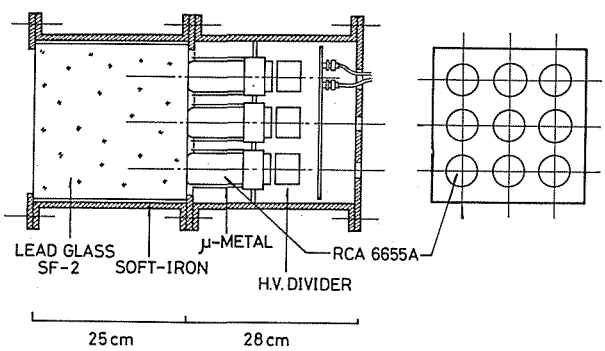

Fig. 5. Construction of the total absorption lead glass Cerenkov counter.

Table 2. Characteristic features of the lead glass SF–2.

Dimension	25cm×25cm×25cm
Density	$\rho=3.84$ g/cm^3
Refractive index	$n_D=1.6477$
Radiation length	$X_0=10.9$ g/cm^2 (2.84 cm)
Critical energy	$\varepsilon=16.9$ MeV

shown in Fig. 5. The Cerenkov material was lead glass SF–2* and whose characteristic features are shown in Table 2. The surfaces of lead glass were painted with CM enamel (TiO_2 paint) for the efficient reflection of Cerenkov light, which was collected on nine 2″ photomultipliers, RCA 6655A's. Each photomultiplier was kept in close contact with lead glass through silicon oil. Photomultipliers were magnetically shielded with a μ-metal cylinder of 1 mm thick and an iron cylinder of 5 mm thick. Lead glass and photomultipliers were assembled in an iron box of 8 mm thick.

Pulse heights and timings of output signals from nine photomultipliers were adjusted to be equal with each other by using attenuators and delay lines. Then output signals were added together and served as a Cerenkov signal. The charactristic features of performances were investigated with a momentum analyzed electron beam and these results are presented in Appendix 1.

The gain of the Cerenkov counter was periodically monitored by analyzing the pulse height of the cosmic ray signals.

(d) Additional apparatuses and set up

In front of the lead spark chamber, veto-counters were placed for the rejection of charged particles. They consisted of two plastic scintillation counters, and each scintillator (10 cm×20 cm×0.5 cm) was viewed with photomultiplier Phillips 56 AVP through Lucite light guide. Also for the rejection of low energy background particles, electrons and photons, two layers of lithium hydride (LiH) absorber were placed and the thickness of these absorbers was 0.1 radiation length each. The absorption efficiency of LiH for photons are discussed in Appendix 2. Two sets of lead slits (20 cm in length) defined the solid angle of each photon detector.

A photograph of the whole system of the π° detector is shown in Fig. 6. Components of each photon detector were assembled on the steel plate of 176 cm×177 cm. These plates were hanged with chain blocks from the top of the steel frame, which was movable with four viecles. The opening angle of two photon detectors was adjusted so as to satisfy the maximum detection efficiency. This adjustment could be performed by sliding the photon detector vertically and by rotating it around the horizontal axis. An accuracy of setting the whole apparatuses was kept usually within ± 1 mm. To change the arrangement from one experimental run to another, it took about 10 hours by six to eight persons.

II–5. *Nucleon detection system*

Recoil nucleons, protons and neutrons, were detected with a hodoscope consisting of 16 modules. A plastic scintillator "National Scintillite"** of each module was a rectangular shape of 10 cm×10 cm×20 cm. Construction of a unit is shown in Fig. 7. The scintillation light was collected to the photomultiplier RCA 6655A through a Lucite light guide. Scintillators and light guides were wrapped with aluminium foils for efficient light collection.

* Lead glass SF–2 was manufactured by Ohara Optical Glass Mfg. Co., Ltd. Kanagawa, Japan.

** "National Scintillite" was manufactured by Matsushita Electric Works, Ltd. Osaka, Japan.

Fig. 6. Photograph of the π° detector.

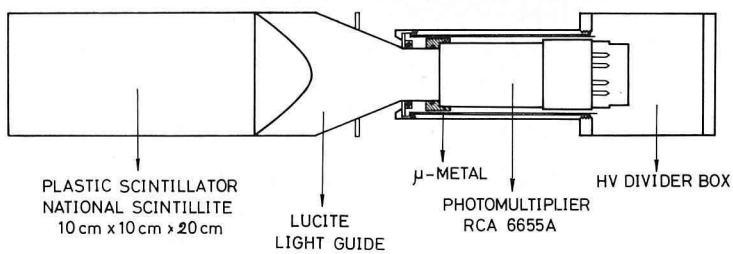

Fig. 7. Cross sectional view of the single module of the nucleon hodosope.

16 modules were assembled in square (4×4 matrix) as is shown in Fig. 2 and were packed in a soft iron box.

In front of this hodoscope, two layers of thin plastic scintillation counters were placed for the discrimination between the proton and the neutron. Each layer consisted of two counters; in the first layer they formed two rows in horizontal and in the second two columns in vertical as is shown in Fig. 2. Each scintillator (21 cm×42 cm×0.5 cm) was viewed with a photomultiplier Phillips 56 AVP through a Lucite light guide.

Ahead of these counters a lead absorber was placed to reduce the low energy background particles. When the nucleon hodoscope was set at the small angle to the beam line, the lead sheet of 0.5 cm thick was placed, and at larger angles that of 0.2 cm thick was placed.

Gains of the nucleon hodoscope were calibrated with a momentum analyzed proton beam and the bias level of each module was adjusted to be equal with each other. The detection efficiency for neutrons depends strongly on the bias level imposed on the continuous pulse height spectrum. Therefore the variation of the bias level was periodically monitored

by measuring the counting rate of each counter due to a ^{60}Co source placed at the fixed position with respect to the counter. The detection efficiencies for neutrons were calibrated by utilizing the process $\gamma+p\rightarrow\pi^{+}+n$ and the results were presented in section III. The detection efficiencies for protons were measured with the momentum analyzed proton beam.

To determine the kinetic energy of the recoil nucleon, their flight time was measured, in which the signals from the Cerenkov counter and from the nucleon hodoscope served as start and stop pulses for a time-to-pulse-height converter (TPC), respectively. In general, time measurement depends on the pulse height of start and stop signals when TPC is used. As the pulses from the nucleon hodoscope for neutrons have a continuous pulse height spectrum, an accuracy of the time measurement was limitted to several nano second with a usual way. In order to surmount these difficulties, a pulse height compensation method was developed and the time resolution of ± 0.5 ns (FWHM) was achieved for neutrons. Details are described in Appendix 3.

II–6. *Electronics*

A block diagram of the electronics used to anlyze the counter outputs from the π° detector and the neutron hodoscope is shown in Fig. 8. Standard modules of electronics; such as attenuators, delay lines, discriminators, coincidences, fast gates and fanouts, were supplied from the electronics shop of the High Energy Division of Institute for Nuclear Study.

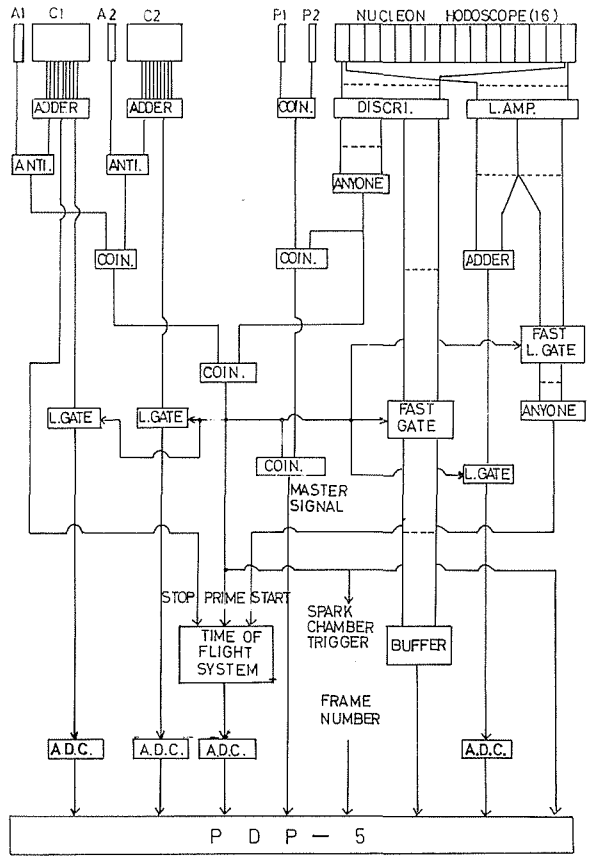

Fig. 8. Simplified block diagram of electronics.

Output signals from nine photomultipliers of each Cerenkov counter were summed up and served as Cerenkov signals, C_1 and C_2. Each of C_1 and C_2 was splitted into three parts; they were used for the fast logics, the pulse height analysis and the stop signals for the TPC. Each of anode signals from 16 photomultipliers of the nucleon hodoscope, $N_1,\cdots\cdots, N_{16}$, was also splitted into three parts; they were used for the fast logics, the pulse height analysis and the start pulses for the TPC. At first, master signals controlling the computer and triggering the spark chamber were obtained with the following fast logics; the veto-counter signals, A_1 and A_2, rejected charged particles and the fast (10 ns) anti-coincidences, $\overline{A}_1\cdot C_1$, $\overline{A}_2\cdot C_2$, were adopted as two photon signals, where an upper line indicate the anti-coincidence. The π° signal was obtained from the fast (15ns) coincidence as follows; $\pi^{\circ}=(\overline{A}_1\cdot C_1)\cdot(\overline{A}_2\cdot C_2)$. When any one of the nucleon hodoscope was fired, the nucleon signal was generated; N=(any one of N_i). The rather slow (120 ns) coincidence between π° and N, $\pi^{\circ}\cdot N$, was used as a master signal for all other slow electronics. No farther selection of the event was perfomed with the fast logics.

When the master signal was generated, the following informations for each event were analyzed and fed into the data processor PDP–5;

1. Pulse heights of two Cerenkov counters. Anode signals from nine photomultipliers of each counter were added together, and after passing through the linear gates, two Cerenkov signals were pulse-height-analyzed with a two dimensional (64×64 channels) analogue-to-digital converter (ADC, Nuclear Data 160F).

2. Pulse height of the nucleon hodoscope. Signals from 16 modules were summed up, and after gated by the master signal, the nucleon signal was also analyzed with the ADC (Nuclear Data 160F, F-side, 64 channels).

3. Flight time of the recoil nucleon. A start signal for the TPC was obtained from the nucleon hodoscope. Output pulse from each module was at first linearly gated by each discriminator signal and then added together. With these handling of 16 signals, pulses from the fired modules could be picked out and the disturbances for the time measurement from the piling up of small pulses could be removed. A stop signal for the TPC was obtained from one of Cerenkov counters. Output pulse from the time of flight system was analyzed with the ADC of 64 channels (Nuclear Data 160F, M-side).

4. Address of the hodoscope. Discriminator outputs from the nucleon hodoscope were gated by the master signal and triggered the flip -flop of the buffer memory (16 channels).

5. Identification of the nucleon charge; recoil protons were distinguished from neutrons with two scintillation counters, P_1 and P_2. The fast coincidence $P_1\cdot P_2\cdot N$ served as a proton signal and $(\overline{P_1\cdot P_2})\cdot N$ served as a neutron signal. These two signals were gated by the master pulse and stored in the buffer memory (2 channels).

6. Frame number of spark chamber films; these were obtained from the scaler output.

These data on ADC's and on the buffer memory were transfered into PDP–5 with a program interrupt mode. As a capacity of PDP–5 memory was not so large (4K words), that no calculation of the data was performed. After only compilation, the data were transfered on a paper tape with a Tally perforator. The perforation time of the data on one event was about 0.2 s.

Spark chambers were triggered also with the master signal. After triggering, the whole electrocics system was inhibited for 0.4s from accepting the detector signals. During this time, spark pictures were photographed and films were advanced, the condenser bank of the high voltage pulsers for spark chambers were recharged and the paper tape was perforated.

III. Experimental Procedure

III–1. *Calibration of the π° detector*

The detection efficiency and the momentum resolution of the π° detector were measured utilizing the process $\gamma+p\rightarrow\pi^\circ+p$, in which rrecoil protons were analyzed with a magnet spectrometer. The experimental arrangement is schematically shown in Fig. 9. The trajectory of protons in the magnet spectrometer was determined with two multiplate optical spark chambers, one of them was placed before the magnetic field and the other was placed at the focal point. The coincidence signal of the plastic scintillation counters, $S_1 \cdot S_2 \cdot S_3 \cdot \overline{S_4}$, triggered these spark chambers. Between S_3 and S_4, the lead absorber was placed to distinguish the proton from the π^+ meson and the positron. The flight time of particles between S_1 and S_2 was also measured and served to the particle identification. The measured proton yield from the hydrogen target was used to reduce the differential cross section for the process $\gamma+p\rightarrow\pi^\circ+p$. The results agreed well with the experimental data at other laboratories.

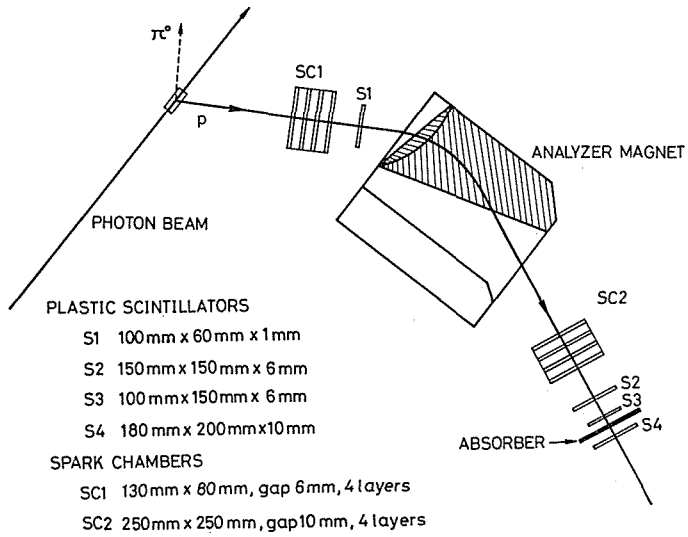

Fig. 9. Magnet spectrometer for the calibration measurements of the π° detector and the nucleon hodoscope. With this spectrometer, the recoil proton from the process $\gamma+p\rightarrow\pi^\circ+p$ and the π^+ meson from the process $\gamma+p\rightarrow\pi^++n$ were detected for the calibration of the π° detector and the nucleon hodoscope, respectively. The spark chambers SC1 and SC2 were removed for the detection of π^+ mesons.

The detection efficiency was obtained only from the counter data. The coincidence rate between the proton and the π° was measured. To increase the time resolution, the TOF between S_1 and one of the Cerenkov counters was measured. The detection efficiency was obtained from the following relation;

$$\eta_{\pi^\circ}=\frac{N(\pi^\circ p)}{N(p)}, \tag{19}$$

where N (p) is the counting rate of the proton, and N (π°p) is the coincidence rate between the π°meson and the proton. The results are listed in Table 3, where the results of the Monte

Table 3. The measured detection efficiencies, momentum resolutions and angular resolutions of the π° detector. Calculated values by the Monte Carlo simulation are also listed. The resolutions are all given by the full-width at half-maximum. The momentum and angular resolutions of the magnet spectrometer for protons are shown in the last three lines.

Experimental arrangement	P_p =294 MeV/c P_{π°=318 MeV/c		P_p =463 MeV/c P_{π°=502 MeV/c		P_p =546 MeV/c P_{π°=600 MeV/c	
	experimental	calculated	experimental	calculated	experimental	calculated
Detection efficiency (%)	0.224 ± 0.015	0.240 ± 0.012	0.393 ± 0.020	0.405 ± 0.023	0.340 ± 0.039	0.378 ± 0.019
Resolution for P_{π°(%)	6.0	2.9	7.7	2.9	4.8	3.4
Resolution for θ_{π°(degree)	3.0	2.3	2.8	2.0	2.5	1.4
Resolution for φ_{π°(degree)	8.0	7.5	8.5	5.0	4.8	4.0
Resolution for P_p (%)		2.6		1.7		1.6
Resolution for θ_p (degree)		1.1		0.7		0.6
Resolution for φ_p (degree)		1.1		0.8		0.7

Carlo simulation are also shown. Details of the Monte Carlo Simulation are presented in Appendix 4. The measured values and the calculated one agreed within the experimental accuracy. The systematic errors included in this measurement were estimated to be about 10%, in which the inaccuracy of evaluating the effective solid angle, the detection efficiency of the Cerenkov counter were the main error sources.

The momentum resolution of the π° detector was evaluated from the spark chamber data. The coincidence signals of the π° meson and the proton triggered four spark chambers, two of which were used to determine the proton trajectory and the other two were lead spark chambers of the π° detector. The momentum of the π° meson was evaluated event by event by the following two ways;

1) from the π° detector, and
2) from the momentum of the recoil proton, $\boldsymbol{P}_p$, using the two body kinematics of the reaction $\gamma+p\rightarrow\pi^\circ+p$.

The first method is described in the next chapter. When $\boldsymbol{P}_{\pi^\circ}$ was derived from the recoil proton momentum, the reaction point, X_T, in the liquid hydrogen target could not be uniquely determined. Proton trajectory intersects with the surface of the effective target volume at two points. The mid-point of these two was assumed as a reaction point.

The distribution of the differences between $\boldsymbol{P}_{\pi^\circ}$'s derived with the above methods, $\Delta\boldsymbol{P}_{\pi^\circ}$, is shown in Fig. 10. In Table 3, the summary of results is shown. The experimental results on the momentum resolution thus obtained can be separated into two parts: the intrinsic resolution of the π° detector and the accuracies of the π° momentum deduced from the measurement of the recoil proton. The latter depends largely on the uncertainty of the reaction point, on the straggling of the proton trajectory and on the accuracy of the spark chamber tracks. Uncertainties were estimated and are shown in Table 3. These show that the uncertainty of π° momentum deduced from the measurement of the recoil proton is relatively large. To achieve more definite conclusions on the resolution of the π° detector, more precise measurements of recoil protons must be needed. However, the results show

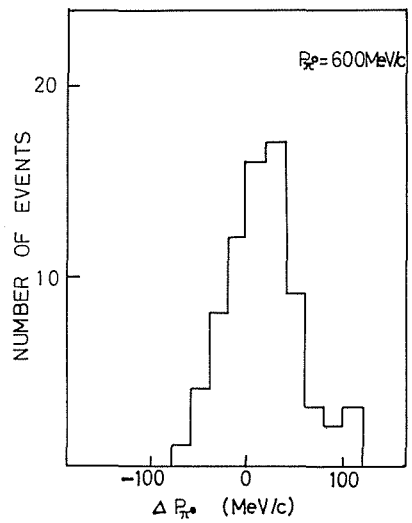

Fig. 10. Momentum resolution of the π° detector. The number of events is plotted as a function of ΔP_{π°.

that the momentum resolution of the π° detector $\Delta \boldsymbol{P}_{\pi^\circ}/\boldsymbol{P}_{\pi^\circ}$ (FWHM) is at least smaller than 5~7% in the energy range between 300~700 MeV.

Angular resolutions of π° detector were also estimated to be 2°~3° in polar angles and to be 4°~8° in azimuthal angles.

The momentum resolution of the π° detector was also calculated by the Monte Carlo simulation using the measured Cerenkov counter resolution and assuming the uncertainty of the reaction point. The results are consistent with the experimental data if the resolution of the proton analyzer is taken into account.

III–2 *Calibration of the neutron detection efficiency*

The neutron detection efficiency of the plastic scintillation counter hodoscope was calibrated by utilizing the process $\gamma+p\rightarrow\pi^+ + n$. The experimental arrangement for the coincidence measurement of the above process was almost the same for the π° detector calibration, where the π° detector was replaced by the nucleon hodoscope and spark chambers were removed. The π^+ meson was detected with the magnet and the scintillation counter telescope of S_1, S_2, S_3 and S_4. The π^+ meson was clearly separated from the proton with the time of flight measurement between S_1 and S_2. In addition, the lead absorber was placed between S_3 and S_4 to absorb protons. The production angle of the π^+ meson in lab. system was chosen to be 64° and 76.7° in accordance with the kinetic energy of the associated neutron. And at these angles, positron contamination in the π^+ meson was estimated to be negligible, so no identification of the positron was carried out. From the measurement of the π^+ meson, the momentum and recoiled angle of the neutron were reduced by using the two body kinematics.

The nucleon hodoscope was placed about 200 cm apart from the liquid hydrogen target so as to satisfy the above kinematical conditions. The fast coincidence between the π^+ meson and the neutron was realized with the TOF measurement. The data on the TOF of the π^+ meson, TOF of the neutron, the address of the hodoscope, the pulse height of the hodoscope and the signal from the veto-counter were stored in PDP–5 event by event.

The neutron detection efficiency was calculated from the following formula;

$$\eta_{\mathrm{n}}=\frac{N(\pi^{+}\cdot\mathrm{n})}{g\cdot N(\pi^{+})}, \tag{20}$$

where $N(\pi^{+})$ is the counting rate of the π^{+} meson, $N(\pi^{+}\cdot\mathrm{n})$ is the coincidence rate between the π^{+} meson and the neutron, and g denotes the geometrical factor, which is reduced from the distribution of the neutron associated with the π^{+} meson. The value of g was calculated with the Monte Carlo simulation, in which the uniform angular and momentum distribution of the emitted π^{+} mesons within the solid angle of the counter telescope were assumed. The typical result on the neutron angular distribution is shown in Fig. 11, where the measured distribution obtained from the hodoscope informations is also shown. The values of g were estimated to be 0.98~1.00 for most arrangements.

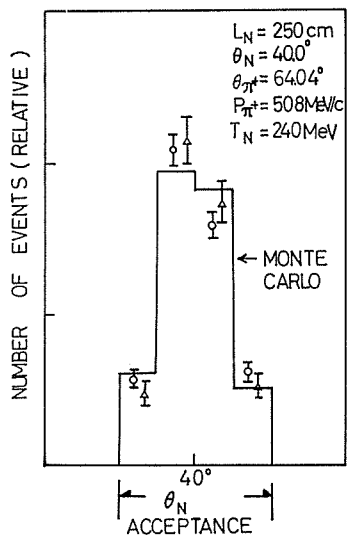

Fig. 11. Hodoscope distribution of recoil neutrons for the calibration measurement utilizing the process $\gamma+\mathrm{p}\rightarrow\pi^{+}+\mathrm{n}$. Points ⊖ and ⊼ represent the results of different runs with the same experimental arrangements for $T_{\mathrm{n}}=240$ MeV. Histogram shows the results of the Monte Carlo simulation.

The relative gain and bias of each module was adjusted to be equal with the momentum analyzed electron beam. The absolute bias level was also measured with the momentum analyzed proton beam. The stability of the electronics system was periodically monitored with the ^{60}Co source.

The corrections for the following items were carefully considered;

1) accidental coincidence; the accidental coincidence rate for the π^{+} meson was smaller than 0.1% of the true one and that for the $\pi^{+}\cdot$n coincidence was about 1% of the true one.
2) empty run; the π^{+} meson production rate from the empty target was 4~5% of that from the full target and the $\pi^{+}\cdot$n coincidence rate from the empty target was negligibly small.
3) misjudge of the veto-counter; if the veto-counter was fired accidentally in coincidence with the neutron counter or by protons generated at the lead absorber,

neutrons can be identified as protons. This misidentification was measured to be about 4%.

The detection efficiency was measured at three values of bias level; 5 MeV, 10 MeV and 20 MeV in terms of the proton energy. The kinetic energy of neutrons ranged from 50 MeV to 400 MeV. The results on each module are shown in Fig. 12, where the errors are due to the statistical one. The other errors, such as the uncertainty of g, the uncertainty of background subtraction, etc. were estimated to be smaller than 1%. The energy spreads of the neutron beam are also shown.

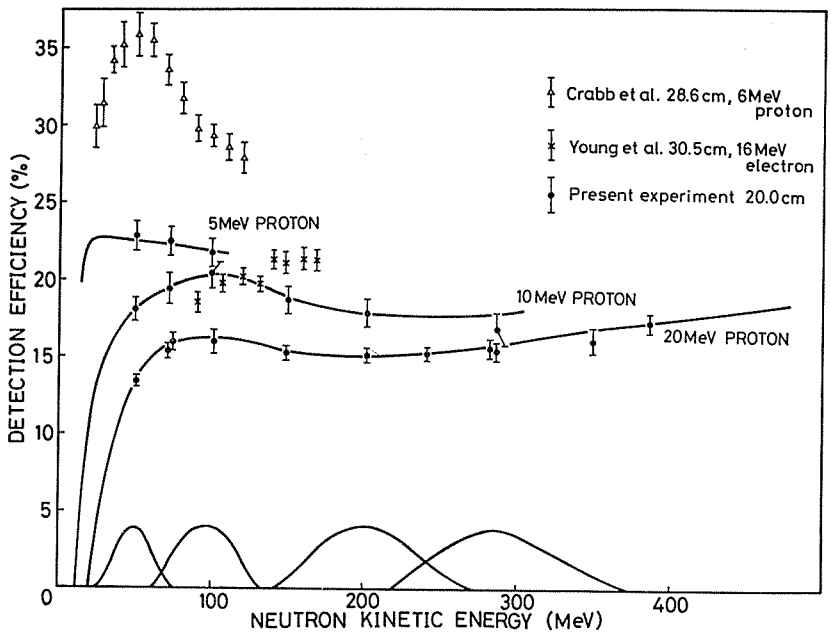

Fig. 12. Neutron detection efficiency vs. neutron kinetic energy. The points ⊕ refer to the present experiment with a 20.0 cm thick plastic scintillator and biases of 5 MeV and 20 MeV in terms of the proton energy. The solid lines corresponding to each set of data are calculated by least squares method with the power-series polynomial. The points ⊼ are the results of Crabb *et al.*[31] for a 28.6cm thick plastic scintillator and bias of 6 MeV proton energy. The points ⋈ are the results of Young *et al.*[32] for a 30.5cm thick plastic scintillator and bias of 16 MeV for the electron energy.

The results show that the neutron detection efficiency is nearly constant at high energies (T_n>100 MeV). Above 300 MeV, the efficiency seems to increase slightly and this fact may be understood as the opening of the pion production channel in the neutron-proton and neutron-carbon collisions.

The calculation of the detection efficiency by the Kurtz's program[30] shows a fairly good agreement with the present data. Previous results at other laboratories are also shown in the same figure.

The rate of firing two or more modules of the nucleon hodoscope was measured as a function of the neutron kinetic energy.[23] The results show that this multiple rate increases almost linearly with the kinetic energy. These rates are about 10% for 100 MeV, 25% for 200 MeV and 35% for 300 MeV of neutron kinetic energy. These multiple events worsened the space resolution of the nucleon hodoscope.

III-3 *Data taking*

The differential cross sections for the processes (14) and (15) were measured at 12 experimental arrangements listed in Table 4, where the kinematical parameters are summarized. In each arrangement, the π° detector and the nucleon hodoscope were located so as to fulfil the two body kinematics of the process $\gamma+n\rightarrow\pi^\circ+n$ at the photon energies of 750 MeV and 600 MeV in the laboratory system. The opening angle of two photon detectors was adjusted to be a minimum correlation angle of two decay photons from the π° meson. The π° detector was placed at about 1.5 m apart from the liquid deuterium target. On the other hand the nucleon hodoscope was placed 4m apart from the target in order to obtain the accurate energy resolution.

Table 4. Kinematical parameters and setup parameters for each arrangement. Kinematical parameters were obtained by assuming the two body process from the rest target. K denotes the incident photon energy; $\theta^c_{\pi^\circ}$, the π° production angle in the cm system; P_{π°, the π° momentum; T_N, the kinetic energy of the recoil nucleon; θ_{π° and θ_N, the setup angles of the π° detector and the nucleon hodoscope, respectively. L_{π° and L_N; the distance of the π° and nucleon detectors from the target, respectively. φ_S: the opening angle of two photon detectors.

Kinematical parameters				Setup parameters of the detector				
K (MeV)	$\theta^c_{\pi^\circ}$ (degree)	P (MeV/c)	T_N (MeV)	θ_{π° (degree)	θ_N (degree)	L_{π° (cm)	L_N (cm)	φ_S (degree)
500	100	333	141	76.8	37.4	178.8	301.6	22.0
600	60	509	74	38.8	57.5	237.8	285.5	14·9
550	90	408	129	62.6	44.0	192.0	300.0	18.8
600	105	383	193	76.8	36.1	176.8	400.0	19.4
600	120	340	234	92.7	28.9	175.9	399.0	21.6
600	140	298	273	113.1	20.9	170.4	347.5	24.4
750	45	670	66	28.5	63.4	278.5	296.4	11.4
750	60	624	112	38.8	55.9	235.3	297.6	12.2
750	90	508	224	62.6	41.2	188.4	397.9	14.9
750	105	448	281	76.8	34.0	173.4	395.2	16.8
750	120	391	335	92.7	27.0	173.2	400.0	19.0
750	140	328	396	112.7	17.8	186.8	352.6	22.4

The bias levels of the discrimators for Cerenkov counters were varied according to the π° momentum. Typical example of the pulse height spectrum of the Cerenkov counter is shown in Fig. 13 for 750 MeV–90° set up.

At most runs of the experiment, the bias level of the nucleon hodoscope was set to be 20 MeV to reduce the accidental rate. When the nucleon hodoscope was set at larger angles to the beam line, at 750 MeV–45° and 600 MeV–60° arrangements, the kinetic energy of recoil nucleons decreased and the bias level was lowered to 10 MeV. Pulse height spectra of the nucleon hodoscope for protons and neutrons are shown in Fig. 14. The spectrum for protons a broad peak corresponding to the kinetic energy spread. On the other hand the spectrum for neutrons is continuous because the charged particles produced by the neutron-proton and neutron-carbon collisions have various kinetic energies. The flight time spectra for protons and neutrons are shown in Fig. 15. Time spreads are almost the

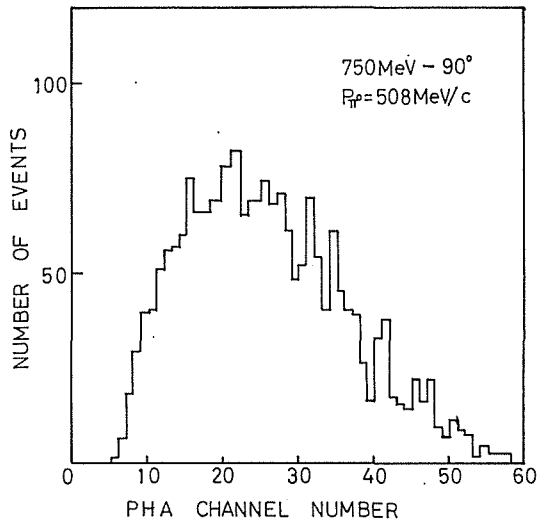

Fig. 13. Pulse height spectrum of the Cerenkov counter for the 750 MeV–90° arrangement. The central value of the momentum is 508 MeV/c.

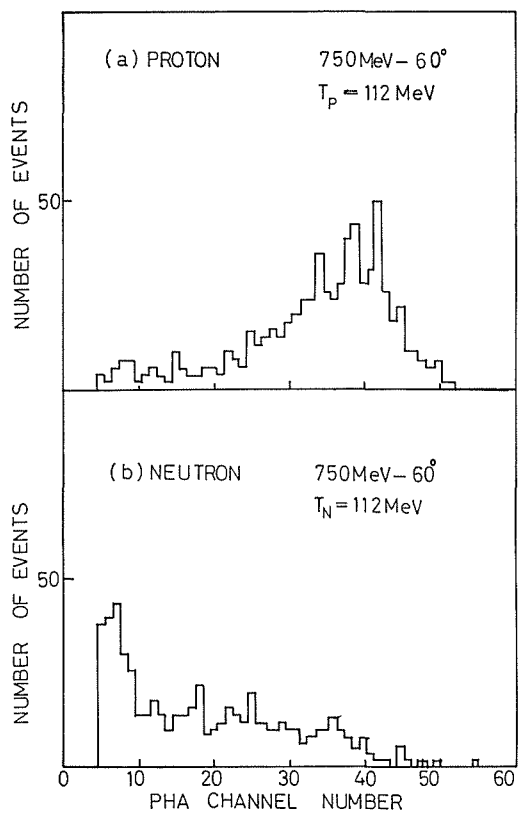

Fig. 14. Pulse height spectra of the nucleon hodoscope for (a) protons and (b) neutrons. Results are presented for the 750 MeV–60° arrangement. The central value of the neutron kinetic energy is 112 MeV.

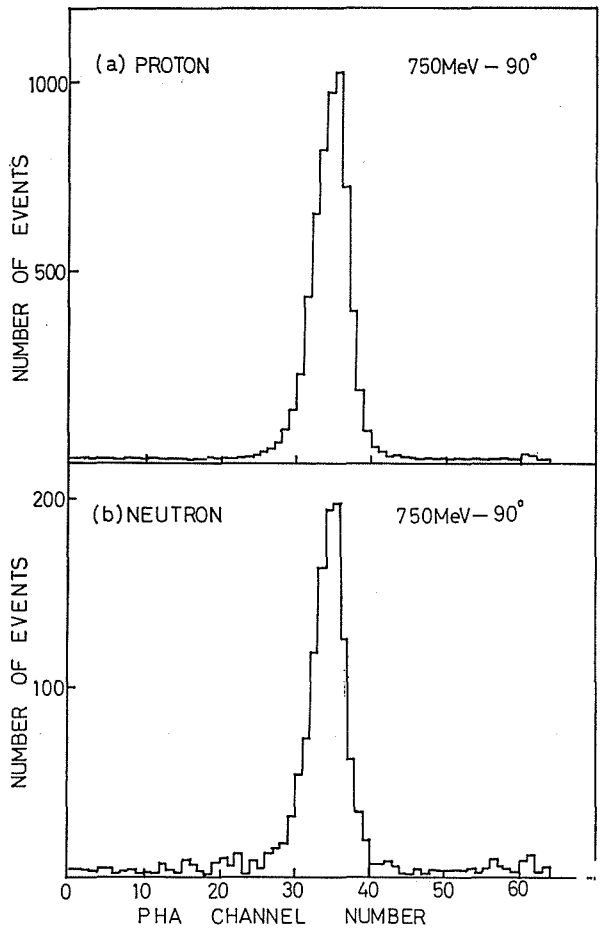

Fig. 15. Time of flight spectra of (a) protons and (b) neutrons for the 759 MeV–90° arrangement.

same for protons and neutrons, and this indicates the success of the pulse height compensation method.

The maximum energy of the bremsstrahlung beam was usually kept to be 950 MeV and the beam spill length was kept to be about 4ms so as to decrease the accidental coincidence rate. The stability of each detector was monitored by counting the single and coincidence rate at every run.

The machine time of about 1 week (108 hours) was spent for the data collection on one experimental arrangement. Several thousands of pictures were photographed for each arrangement. The trigger rate for the process $\gamma+\mathrm{p}\rightarrow\pi^{\circ}+\mathrm{p}$ was five to six times larger than that for the process $\gamma+\mathrm{n}\rightarrow\pi^{\circ}+\mathrm{n}$, because of the small neutron detection efficiency.

III-4 *Hydrogen target calibration*

The detection efficiency of the whole system was calibrated by utilizing the process $\gamma+\mathrm{p}\rightarrow\pi^{\circ}+\mathrm{p}$. The measurements were carried out with the liquid hydrogen target at 750 MeV–105°, and 600 MeV–105° arrangements. The whole system was kept the same for the

deuterium run only except that liquid deuterium in the target container was replaced by liquid hydrogen.

By comparing the experimental results on the processes $\gamma+p\rightarrow\pi^\circ+p$ and $\gamma+d\rightarrow\pi^\circ+p+n_s$, the following effect was realized;

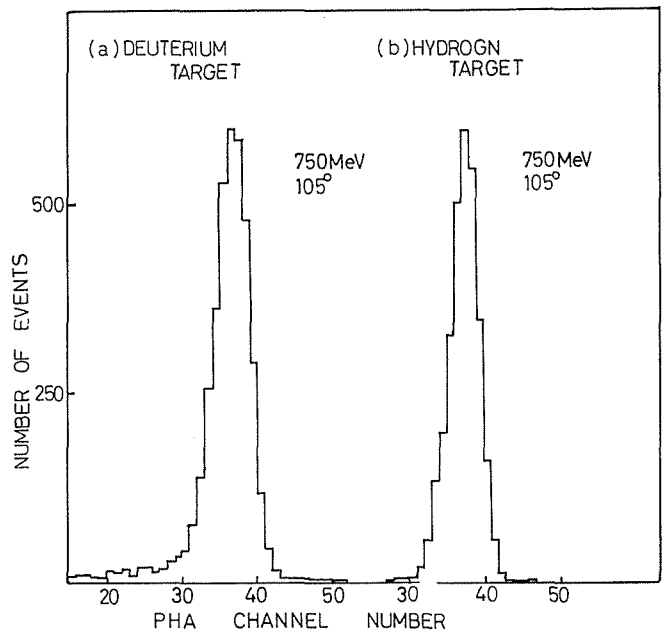

Fig. 16. Comparison of the time of flight spectrum of protons from the hydrogen target with that from the deuterium target.

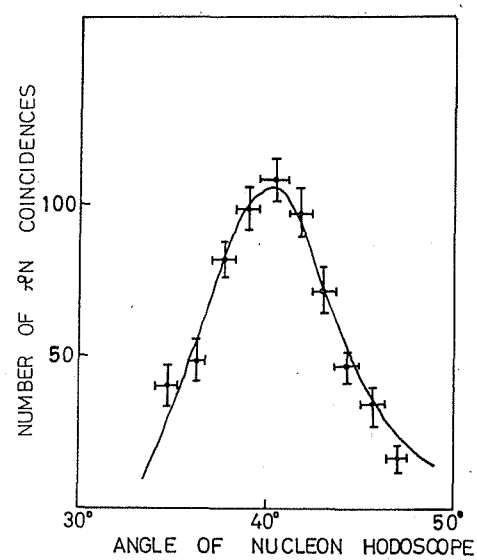

Fig. 17. Angular correlation between recoil protons and π° mesons from the deuterium target. The solid line denotes the calculated distribution by the Monte Carlo simulation.

1) kinematical effect due to the internal motion of target nucleons inside the deuteron,

2) dynamical effect due to target nucleons bound in the deuteron, which is discussed in VI–3.

Kinematical effect was found in the energy distribution and angular distribution of recoil protons. The time of flight spectra of recoil protons for the hydrogen and deuterium target processes are shown in Fig. 16, where the time spreads for 750 MeV–105° arrangement are 4.5 ns and 5.5 ns, respectively. Angular distributions of recoil protons were measured by rotating the nucleon hodoscope around the target and the results are shown in Fig. 17. Due to the internal motion of target protons in the deuteron, recoil protons from the deuterium target are more widely distributed than those from the hydrogen target. Kinematical effect on these distributions was evaluated with a Monte Carlo simulation described in Section V, and the results are in good agreements with the experiment. Further, additional checks on the momentum reduction of π° meson and the recoil proton were performed by utilizing the hydrogen target process.

IV Data Reduction

IV–1. *General*

The differential cross sections on the processes $\gamma+\mathrm{d}\to\pi^\circ+\mathrm{p}+\mathrm{n_s}$ and $\gamma+\mathrm{d}\to\pi^\circ+\mathrm{n}+\mathrm{p_s}$ were derived from the informations stored on the paper tapes of PDP–5 and on the spark chamber films by the following way:

(1) scanning and measuring of the spark chamber pictures,
(2) reduction of the π° momentum,
(3) reduction of the recoil nucleon momentum,
(4) reconstruction of the kinematical variables,
(5) correction of the measured counting rate,
(6) calculation of the detection efficiency with the Monte Carlo simulation,
(7) reduction of the differential cross sections.

Block diagram for the kinematical reconstruction of each event is shown in Fig. 18. Final goal of this scheme is to rearrange the obtained events in terms of two kinematical variables, the incident photon energy and the π° emission angle at the coordinate system where the target nucleons are at rest. Hereafter the above coordinate system is called as a target-at-rest system. Detailed descriptions on the kinematical reconstruction were presented by Hemmi[23]. In this section, we present only the outline.

IV–2. *Scanning and measuring of the spark chamber pictures*

The handling of the spark chamber films started with the rough sketch of spark pictures on the coding form by scanners. From these sketches, physicists selected the shower pictures by the following criteria;

1. there must be more than two sparks at the succeeding gaps.
2. there must be no sparks at the first gap.

Typical example of the shower tracks is shown in Fig. 19. For the most cases, photon shower events were easily discriminated from the spurious sparks or from the charged particle tracks. Some questionable events such as the overlap of spurious sparks (5%) and double photon showers (2%) were found. The sparks whose coordinates should be measured were selected by the above preliminary scanning.

About 70% of pictures from one photon detector were good events, and this value corresponded to the photon conversion efficiency in the lead spark chamber. For the reduc-

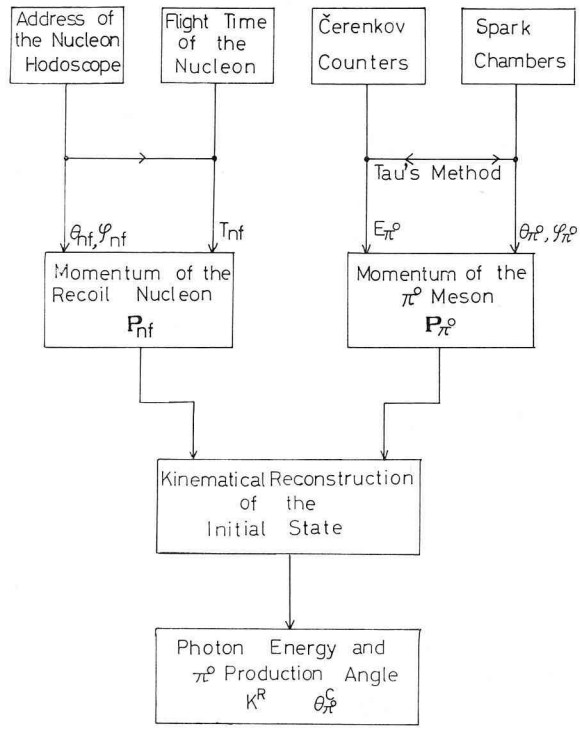

Fig. 18. Block diagram of the kinematical reconstruction of each event.

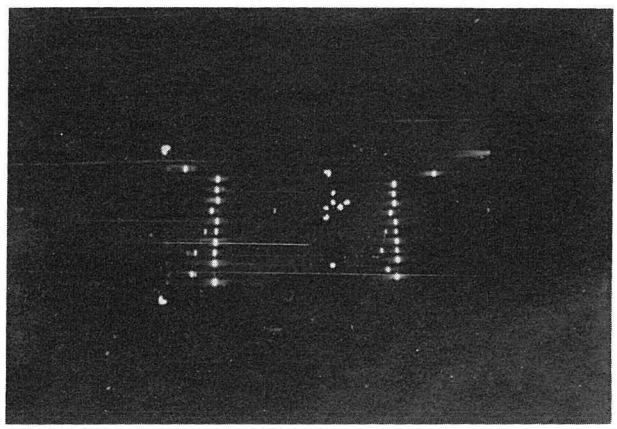

Fig. 19. Typical example of the spark chamber picture.

tion of the π° momentum, both decay photons must be observed in coincidence. Therefore only the event that both pictures were good (about 45~50% of films) was measured.

Manual measurements of the spark coordinates on the film projector were carried out by four scanners. Projected images were 2 times smaller than those in the real spark chamber spaces. The measuring errors of the spark coordinate were estimated to be ± 0.25 cm at the real spark chamber spaces.

Conversion point distribution of photons in the spark chamber is shown as a function

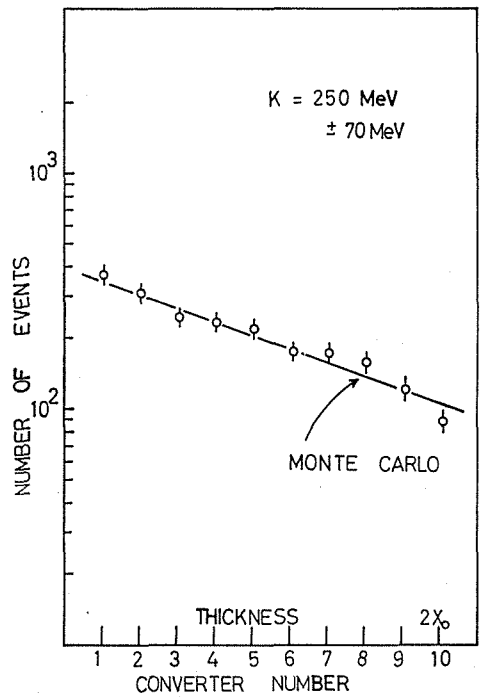

Fig. 20. Distribution of the conversion rate of photons versus the number of the lead layer in the lead-sandwiched spark chamber for the 750 MeV–90° arrangement.

of the thickness of the lead converters in Fig. 20. From this, we confirmed that the photons were clearly detected.

IV–3. *Reduction of the π° momentum*

The π° momentum was calculated from the following four informations about the two decay photons using the Tau's method;[29] the positions where the photons were converted into electron pairs, which were observed by the lead sandwiched spark chambers, and the energies of decay photons which were measured by the total absorption type lead glass Cerenkov counters. Schematical diagram of the π° detection system is shown in Fig. 21. The coordinate system is chosen so that the Z-axis coincides with the π° direction and the Y-axis is a vertical line. The reaction point in the target could not be derived from the shower tracks of photons in the lead snadwiched spark chambers, because the pair electrons meander on account of the multiple scattering. The average deflection angle of the 200 MeV electrons by passing through the lead plate of 5 mm ($1X_0$) is about 2×10^{-2} radian. Therefore the reaction points were assumed to be the center of the effective target volume, which was the origin of our coordinate system. The correlation angle between two decay photons, φ, was calculated from the two conversion points, p_1 (x_1, y_1, z_1) and p_2 (x_2, y_2, z_2), as follows;

$$\cos\varphi=\frac{x_1x_2+y_1y_2+z_1z_2}{\sqrt{x_1^2+y_1^2+z_1^2}\cdot\sqrt{x_2^2+y_2^2+z_2^2}}\,. \tag{21}$$

On the other hand, the photon energies, k_1 and k_2 were evaluated from the pulse heights of the Cerenkov counters and the address of lead converters (z_1 and z_2), because photons which were converted in the spark chamber lost their energies in both spark chambers and

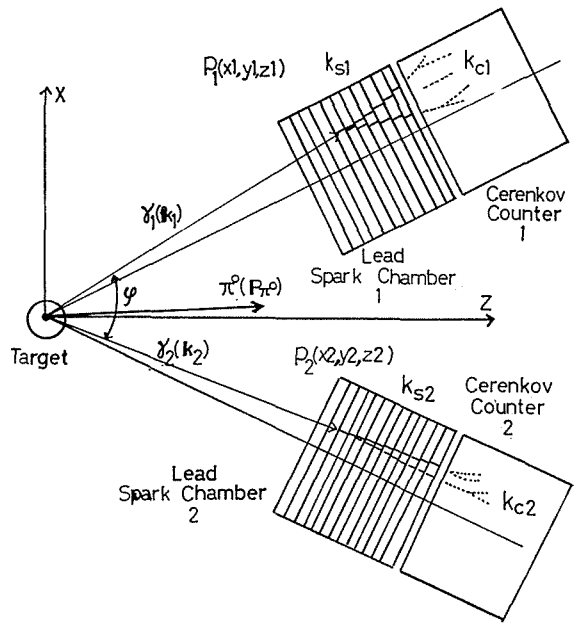

Fig. 21. Schematic diagram of the π° momentum reduction. Conversion points of two decay photons from the π° mesons are denoted by $p_1(x_1, y_1, z_1)$ and $p_2(x_2, y_2, z_2)$. k_{s1} and k_{s2} denote the energy losses in the lead spark chambers. k_1 and k_2 denote the energy losses in the Cerenkov counters.

Cerenkov counters. Thus the energy of the original photon, k, was represented by the following expression;

$$k=k_s(z, k)+k_c\,, \tag{22}$$

where k_s and k_c represent the energy loss in the spark chamber and the energy loss in the Cerenkov counter, respectively. The k_s was evaluated from the shower theory[33]. The ratio k_s/k varied from 0.05 to 0.30 for 250 MeV photons when the photons were converted into electron pairs in the spark chamber.

If φ and k_1, k_2 can be measured without experimental errors, they should satisfy the following relation which can be derived from the energy momentum conservation laws;

$$k_1 \cdot k_2=\frac{\mu}{2(1-\cos\varphi)}\,. \tag{23}$$

The energy resolution of the Cerenkov counter for 250 MeV photons was estimated to be about 30% (FWHM) and $\Delta\varphi$ was estimated to be $\pm 1^\circ$, which was mainly due to the ambiguity of the reaction point in the effective target volume. Therefore in general, the measured values of left-hand and right-hand terms in eq. (23) are not equal each other. The ambiguity of the left-hand term is larger than that of the right-hand term, because the correlation angle can be measured rather accurately with the spark chambers. So the right-hand term in eq. (23) is assumed to represent the true value, which is denoted by A. In Fig. 22, the photon energies k_1 and k_2 are expressed as an abscissa and an ordinate, respectively. The measured photon energies, M (k_1', k_2') does not satisfy the eq. (23). Therefore on the hyperbola the nearest point from the M (k_1', k_2') is adopted as the most probable photon energies, R (k_1'', k_2''). From the above conditions, R (k_1'', k_2'') must satisfy the following relations;

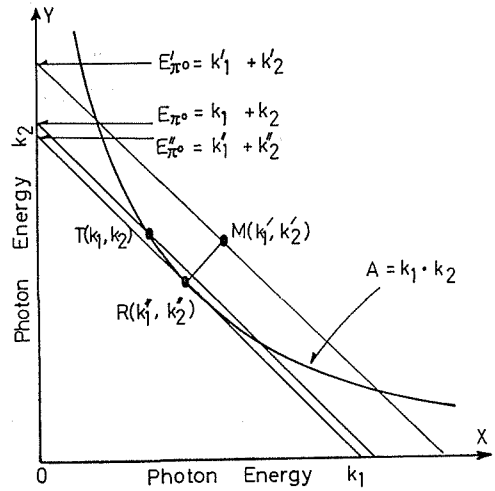

Fig. 22. Reduction of the momentum of the π° meson with Tau's method. $T(k_1, k_2)$ denotes the true phootn energies from the π° meson. $M(k_1', k_2')$ denotes the measured values of photon energies. The hypabolla can be drawn from the measurement of the correlation angle of two decay photons. The point $R(k_1'', k_2'')$ on the hypabola, which is the nearest point from the $M(k_1', k_2')$, can be adopted as the most probable photon energies.

$$k_1''^4-k_1'\cdot k_1''^3+Ak_2'\cdot k_1''-A^2=0\,, \tag{24}$$

$$k_1''\cdot k_2''=A\,. \tag{25}$$

k_1'' and k_2'' are evaluated by solving these equations with the well-known Newton's method or Ferrari's method. The total energy of the π° meson is the sum of two photon energies;

$$E_{\pi^0}=k_1''+k_2''\,. \tag{26}$$

The momentum vector of π° mesons is also calculated from the momentum vectors of two photons, $\boldsymbol{k}_1''$ and $\boldsymbol{k}_2''$ as follows;

$$\boldsymbol{P}_{\pi^0}=\boldsymbol{k}_1''+\boldsymbol{k}''\,. \tag{27}$$

IV–4 *Reduction of the recoil nucleon momentum*

The recoil nucleon momentum, $\boldsymbol{P}_{\mathrm{nf}}$ was obtained from the time of flight measurement and the address of the nucleon hodoscope. Practically the time differences, t, between two pulses, one from the Cerenkov counter and the other from the nucleon hodoscope, were measured. So the velocity of the recoil nucleon, βc, can be derived from the following relation;

$$t=\frac{L_{\mathrm{N}}(i)}{\beta c}-\frac{L_{\mathrm{M}}}{c}\,, \tag{28}$$

where $L_{\mathrm{N}}(i)$ is the distance of i-th module of the nucleon hodoscope from the target and L_{M} is the distance of the Cerenkov counter. c denotes the light velocity.

Th incident position of the recoil nucleon on the hodoscope was defined as the center of the forward face of the plastic scintillator when single module was fired. For the high energy nucleons, two or more modules were often fired simultaneously. In these cases, the center of gravity of the fired modules was adopted as the incident position. The momentum resolution for the recoil nucleon in the flight time measurement can be evaluated as follows;

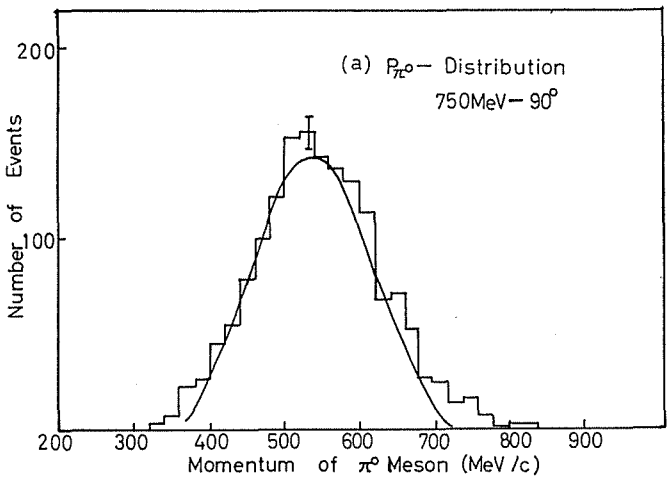
(a) P_{π^0} – Distribution
750MeV – 90°
Number of Events
200
100
200 300 400 500 600 700 800 900
Momentum of π° Meson (MeV/c)

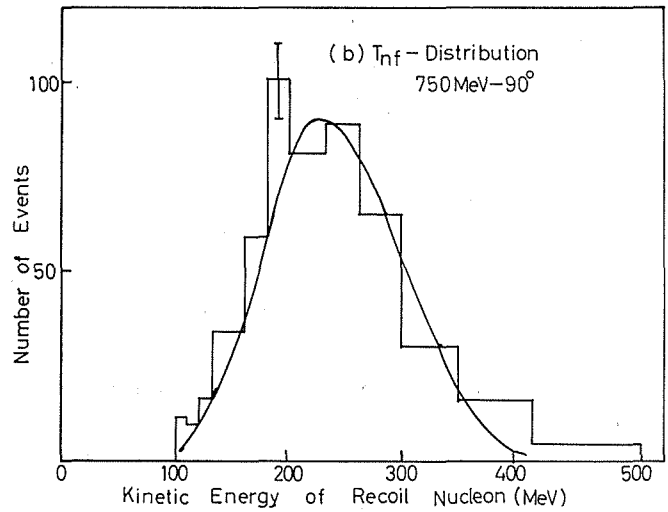
(b) T_{nf} – Distribution
750MeV–90°
Number of Events
100
50
0 100 200 300 400 500
Kinetic Energy of Recoil Nucleon (MeV)

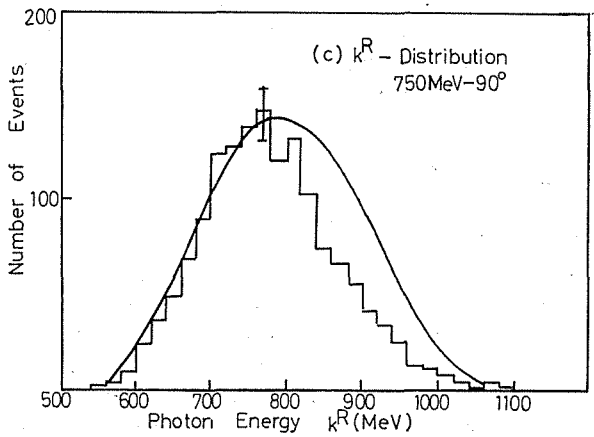
(c) k^R – Distribution
750MeV–90°
Number of Events
200
100
500 600 700 800 900 1000 1100
Photon Energy k^R (MeV)

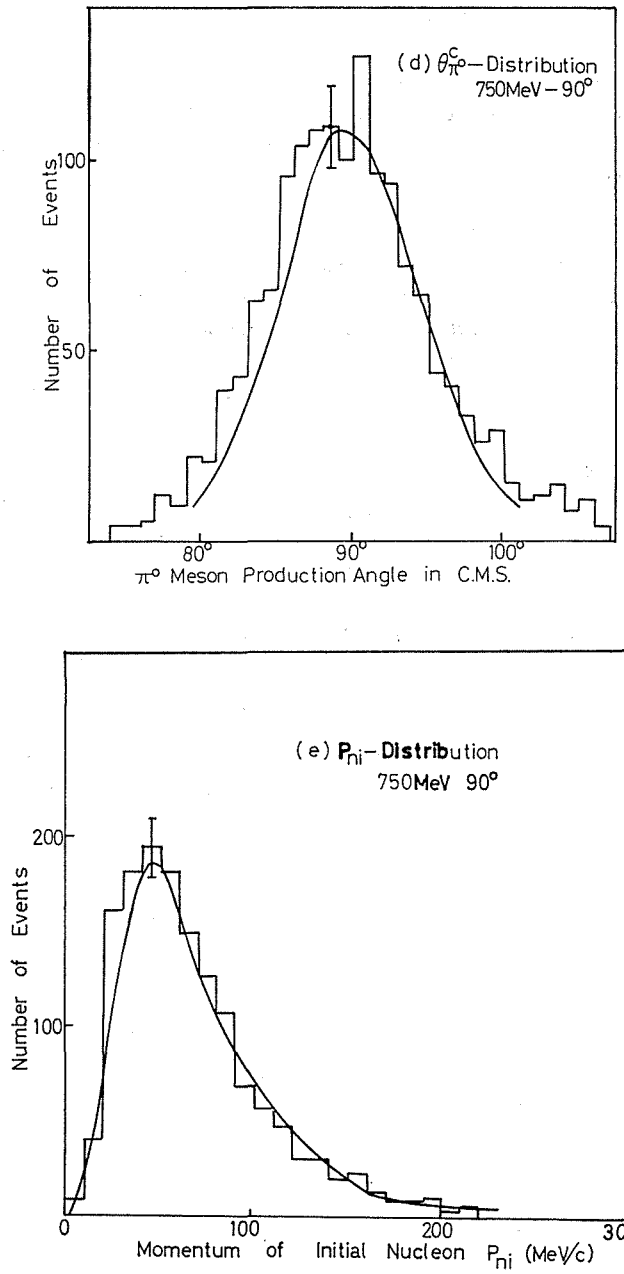

Fig. 23. Results of the kinematical reconstruction for the 750 MeV–90° arrangement. The solid line in each figure shows the results of the Monte Carlo simulation.

(a) momentum distribution of π° mesons.
(b) kinetic energy distribution of recoil nucleons.
(c) energy distribution of incident photons in the target-at-rest system.
(d) production angle distribution of π° mesons in the center of mass system.
(c) momentum distribution of target nucleons in the laboratory system.

$$\frac{\Delta P_{nf}}{P_{nf}}=\frac{-\beta c\cdot\Delta t}{(1-\beta^2)\cdot L_N}. \tag{29}$$

For example, under the time resolution of ± 0.5 ns and L_N of 400 cm, $\Delta P/P$ is evaluated to be ± 0.05 for $\beta=0.7$ (which corresponds to $T_{nf}=380$ MeV). Systematic errors in the time of flight measurement were carefully corrected. Angular resolutions of the nucleon hodoscope were calculated to be $\Delta\theta_{nf}\sim 2°$ and $\Delta\varphi_{nf}\sim 2°$

IV–5 *Kinematical reconstruction*

Momentum distributions of the $\pi°$ meson and the recoil nucleon are shown in Fig. 23 for the 750 MeV–90° arrangement. From these final state momenta, all kinematical variables for the process $\gamma+n\to\pi°+n$ could be completely determined by assuming the spectator model. From the two body kinematics, energy and momentum conservation laws state the following relations;

$$\boldsymbol{k}+\boldsymbol{P}_{ni}=\boldsymbol{P}_{\pi°}+\boldsymbol{P}_{nf} \tag{30}$$

$$k+E_{ni}=E_{\pi°}+E_{nf}, \tag{31}$$

where $(\boldsymbol{k}, k)$, $(\boldsymbol{P}_{ni}, E_{ni})$, $(\boldsymbol{P}_{\pi°}, E_{\pi°})$ and $(\boldsymbol{P}_{nf}, E_{nf})$ are the four momentum vectors of the incident photon, of the initial target nucl on, of the $\pi°$ meson and of the recoil nucleon, respectively. There are 16 variables. However, four conservation equations and four energy-momentum relations decrease the number of independent variables to 8. Among 16 variables in eqs. (30) and (31), 8 variables ($\boldsymbol{P}_{\pi°}$, $\boldsymbol{P}_{nf}$ and the incident direction of photons $\boldsymbol{k}/|\boldsymbol{k}|$) can be measured. So the eqs. (30) and (31) can be solved and other kinematical variables can be derived.

Then these kinematical variables at the laboratory system were transformed into those at the center of mass system, where the Z-axis was chosen to coincide with the incident photon direction. Finally photon energies were expressed as $\boldsymbol{k}^R$ in the target-atrest system

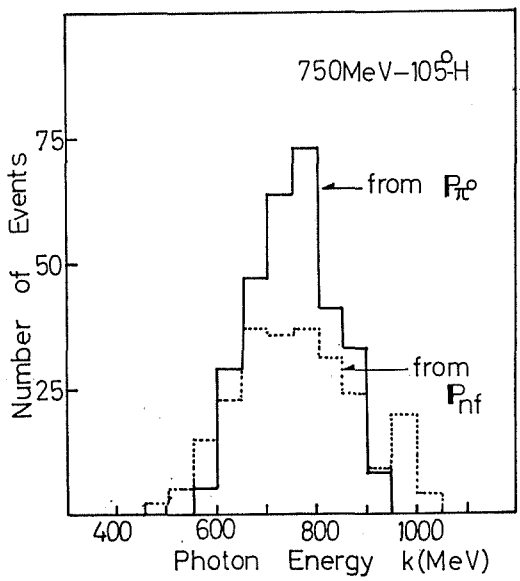

Fig. 24. Energy distribution of incident photons for the 750 MeV–105°–H arrangement. Solid and dotted histogram show the results reduced from the $\pi°$ momentum and from the recoil nucleon momentum, respectively.

for the comparison of results with the free target data. Kinematics is summarized in Appendix 5.

The validity of the kinematical reconstruction was checked with the results on the free target process $\gamma+\mathrm{p}\rightarrow\pi^\circ+\mathrm{p}$. When the target is at rest, incident photon energies can be evaluated either only from $\boldsymbol{P}_{\pi^\circ}$ or only from $\boldsymbol{P}_{\mathrm{nf}}$. Energy distributions of incident photons derived from $\boldsymbol{P}_{\pi^\circ}$ and $\boldsymbol{P}_{\mathrm{nf}}$ were shown in Fig. 24. The agreement between them confirmed us the validity of the kinematical reconstruction.

IV-6 *Counting rate corrections*

Several corrections to the counting rate and to be made to take into account the contributions from the various competing processes.

First, the empty target background was subtracted from the full target counting rate. These corrections were only less than 0.2% and negligibly small.

The largest correction was due to the accidental coincidences between the π° detector and the nucleon hodoscope. For the proton process $\gamma+\mathrm{d}\rightarrow\pi^\circ+\mathrm{p}+\mathrm{n_s}$, it was 2~10% and for the neutron process $\gamma+\mathrm{d}\rightarrow\pi^\circ+\mathrm{n}+\mathrm{p_s}$, it amounted to 5~25% for various experimental arrangements. These accidental backgrounds were subtracted from the TOF spectra.

The off-kinematical background, especially form the double pion production, was checked by rotating the nucleon hodoscope around the target. The measured results agreed well with the Monte Carlo simulation and this confirmed us that the contribution from the multiple pion production was negligibly small.

Dead time correction due to the inhibition time of 0.4 s was calculated to be less than 1% for all experimental runs.

V. Monte Carlo Simulation

V-1 *Differential cross section formulas*

The reduction of the differential cross section was very complicated due to the use of the moving target. In addition, the π° detection efficiency was not constant but an complicated function of many independent variables. So the detection efficiency and the solid angle of the whole detection system were evaluated by the Monte Carlo simulation. At this simulation, the spectator model for the deuteron target process was assumed.

The coincidence rate of the π° meson and the recoil nucleon (proton or neutron) from the deuterium target can be expressed as a multiple integral over the effective target valume, photon energy, initial momentum of the target nucleon, and laboratory solid angle:

$$C=\int\!\!---\int\frac{\mathrm{d}\sigma}{\mathrm{d}\Omega^{\mathrm{c}}_{\pi^\circ}}(k^{\mathrm{R}},\theta)\cdot n_{\mathrm{T}}\cdot\phi(\boldsymbol{P}^{\mathrm{L}}_{\mathrm{ni}})\cdot N(k^{\mathrm{L}})\cdot T(x_{\mathrm{T}},y_{\mathrm{T}})\cdot A(\boldsymbol{P}^{\mathrm{L}}_{\pi^\circ},\boldsymbol{P}^{\mathrm{L}}_{\mathrm{nf}},x_{\mathrm{T}},y_{\mathrm{T}},z_{\mathrm{T}})\cdot\mathrm{d}\Omega^{\mathrm{c}}_{\pi^\circ}\cdot\mathrm{d}k^{\mathrm{L}}\cdot\mathrm{d}\boldsymbol{P}^{\mathrm{L}}_{\mathrm{ni}}\cdot\mathrm{d}x_{\mathrm{T}}\cdot\mathrm{d}y_{\mathrm{T}}\mathrm{d}z_{\mathrm{T}}\,, \tag{32}$$

where

C : coincidence rate of the π° meson and the recoil nucleon per 1000 MU.

$\frac{\mathrm{d}\sigma}{\mathrm{d}\Omega^{\mathrm{c}}_{\pi^\circ}}(k^{\mathrm{R}},\theta^{\mathrm{c}}_{\pi^\circ})\mathrm{d}\Omega^{\mathrm{c}}_{\pi^\circ}$: differential cross section for the single pion photoproduction from nucleons (protons or neutrons) by the photon of energy k^{R}, producing the π° meson in $\mathrm{d}\Omega^{\mathrm{c}}_{\pi^\circ}$ at $\theta^{\mathrm{c}}_{\pi^\circ}$. Hereafter the upper suffices $_{\mathrm{L}}$, $_{\mathrm{c}}$ and $_{\mathrm{R}}$ denote the laboratory system, the center of mass system and the targetat-rest system, respectively.

$n_{\mathrm{T}}\phi(\boldsymbol{P}^{\mathrm{M}}_{\mathrm{ni}})\mathrm{d}\boldsymbol{P}^{\mathrm{M}}_{\mathrm{ni}}$: number of target nucleons with momenta between $\boldsymbol{P}^{\mathrm{L}}_{\mathrm{ni}}$ and $\boldsymbol{P}^{\mathrm{L}}_{\mathrm{ni}}+$

$d\boldsymbol{P}^{L}_{nf}$.

$N(k^L)dk^L$: number of photons per 1000 MU with energies between k^L and k^L+dk^L.

$T(x_T, y_T)$: normalyzed beam intensity at point (x_T, y_T) in a plane perpendicular to the beam at the target.

$A(\boldsymbol{P}^{L}_{\pi^\circ}, \boldsymbol{P}^{L}_{nf}, x_T, y_T, z_T)$: detection efficiency of the π° meson with momentum $\boldsymbol{P}^{L}_{\pi^\circ}$ and the nucleon with momentum $\boldsymbol{P}^{L}_{nf}$ in coincidence. (x_T, y_T, z_T) indicates the reaction point point in the target, where z_T is the distance from the target center in the direction of the incident photon beam.

The limits of integration are determined by the limits of the target beam interaction volume and by the detection efficiency. The number of independent variables in eq. (32) are 9, and 6 of which are related to the kinematical variables for the moving target reaction, 3 of which are related to the reaction point in the target volume. The other variables in the integrand are derived from these 9 variables through the two body kinematics and the Lorentz transformation.
(Appendix 5).

The experimental results on the coincidence rate were obtained as a function of one variable, k^R;

$$C=\int Y(k^R)dk^R\,, \tag{33}$$

where

$Y(k^R)dk^R$: coincidence rate of the π° meson and the nucleon with incident photon energy between k^R and k^R+dk^R.

As the angular acceptance of the detection system was about $\pm 5.0^\circ$ in the center of mass system, the integration on $d\Omega^c_{\pi^\circ}$ was already performed in the above results.

The differential cross sections were obtained from the following equation;

$$\frac{d\sigma}{d\Omega^c_{\pi^\circ}}(k^R)=\frac{\int_{k_2}^{k_2} Y(k^R)dk^R}{\int_{k_2}^{k_2} M(k^R)dk^R}\,, \tag{34}$$

where

$$M(k^R)dk^R=\int\!\!---\!\!\int n_T\phi(\boldsymbol{P}^{L}_{ni})\cdot N(k^L)\cdot T(x_T, y_T)\cdot A(\boldsymbol{P}^{L}_{ni}, \boldsymbol{P}^{L}_{ni}, x_T, y_T, z_T)\cdot d\Omega^c_{\pi^\circ}\cdot dk^L\cdot d\boldsymbol{P}^{L}_{ni}\cdot dx_T\cdot dy_T\cdot dz_T\,. \tag{35}$$

Thus the differential cross sections were obtained as a function of k^R. The values were presented at the energy interval of 50 MeV, which was related to the energy resolution of the whole detection system.

The multiple integral in eq. (35) was evaluated by the Monte Carlo simulation.

V–2 *Monte Carlo simulation process*

The Monte Carlo simulation of the events was performed with a computor FACOM 230/60 at the Computor Center of Kyoto University.

The main flow chart of the computer program is shown in Fig. 25. The event simulation of the process started with the random choice of kinematical variables in the laboratory system, which might represent the real probability distribution;

(a) $T(x_T, y_T)$ was reduced from the intensity distribution of the photon beam at the target.

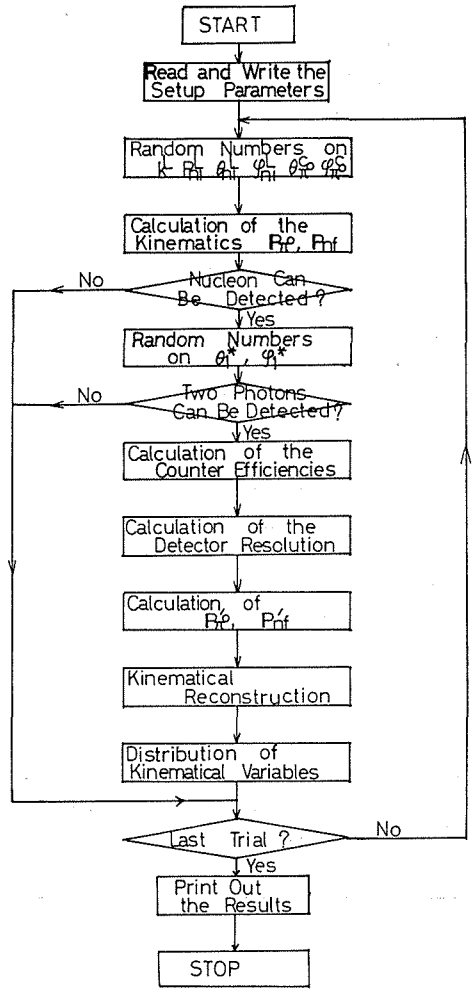

Fig. 25. Flow chart of the Monte Carlo simulation.

(b) $\phi(\boldsymbol{P}_{\mathrm{ni}}^{\mathrm{L}})$ was assumed to be given by the Hulthen wave function for the deuteron.

(c) $N(k^{\mathrm{L}})$ was obtained from the bremsstrahlung spectrum given by the Schiff's thin target formula.

(d) $\theta_{\pi^{\circ}}^{\mathrm{c}}$ and $\varphi_{\pi^{\circ}}^{\mathrm{c}}$, production angles of the π° meson at the center of mass system, was assumed to be distributed uniformly.

From the above kinematical variables, $(x_{\mathrm{T}}, y_{\mathrm{T}}, z_{\mathrm{T}}, \boldsymbol{P}_{\mathrm{ni}}^{\mathrm{L}}, k^{\mathrm{L}}, \theta_{\pi^{\circ}}^{\mathrm{c}}, \varphi_{\pi^{\circ}}^{\mathrm{c}})$, all other variables were calculated.

The detection efficiency A $(\boldsymbol{P}_{\pi^{\circ}}^{\mathrm{L}}, \boldsymbol{P}_{ni}^{\mathrm{L}}, x_{\mathrm{T}}, y_{\mathrm{T}}, z_{\mathrm{T}})$ was decomposed into following four parts;

$$A(\boldsymbol{P}_{\pi^{\circ}}^{\mathrm{L}}, \boldsymbol{P}_{\mathrm{ni}}^{\mathrm{L}}, x_{\mathrm{T}}, y_{\mathrm{T}}, z_{\mathrm{T}})=G(\boldsymbol{P}_{\pi^{\circ}}^{\mathrm{L}}, \boldsymbol{P}_{\mathrm{nf}}^{\mathrm{L}}, x_{\mathrm{T}}, y_{\mathrm{T}}, z_{\mathrm{T}})\cdot\eta_1(k_2)\cdot\eta_2(k_2)\cdot\eta_{\mathrm{n}}(T_{\mathrm{nf}}), \quad (36)$$

where

$G(\boldsymbol{P}_{\pi^{\circ}}^{\mathrm{L}}, \boldsymbol{P}_{\mathrm{nf}}^{\mathrm{L}}, x_{\mathrm{T}}, y_{T}, z_{\mathrm{T}})$: geometrical detection efficiency, whose value is 1 or 0 when the simulated event can be detected or can not be detected, respectively.

$\eta_1(k_1)$ and $\eta_2(k_2)$: the detection efficiency of each photon detector for photons with energies k_1 and k_2.

$\eta_n(T_{nf})$: the detection efficiency of the nucleon hodoscope for the recoil nucleon with kinetic energy of T_{nf}.

The Monte Carlo process evaluating the π° detection efficiency is presented in Appendix 4.

When the simulated event could be detected with the π° detector and the nucleon detector in coincidence, the kinematical reconstruction was performed in taking into account the resolution of detectors. This process was the same as the experimental data reduction. Detector resolutions considered are;

(1) energy resolution of the Cerenkov counter,
(2) resolution of the TOF measurement,
(3) angular resolution of the nucleon hodoscope,
(4) reaction point in the target volume, which was assumed to be the target center for all events.

The results of these simulation were obtained as a function of k'^R, where k'^R denotes the photon energy in the target-at-rest system reconstructed in taking account of the detector resolutions.

The efficiency of the Monte Carlo simulation was about $10^{-6}\sim10^{-7}$ when the π° meson was produced in 4π solid angles in the center of mass system and when the π° meson decayed into two photons in 4π solid angles in the π° rest system. By careful choice of the kinematical regions, however, it was increased to about 10^{-3}.

V–3 *Monte Carlo results*

The results of the Monte Carlo simulation are shown in Fig. 26, where k'^R distributions, $M(k'^R)$, are presented for each arrangement. These distributions have their maxima at the photon energy of 770~800 MeV for the 750 MeV arrangements and 620~650 MeV for the

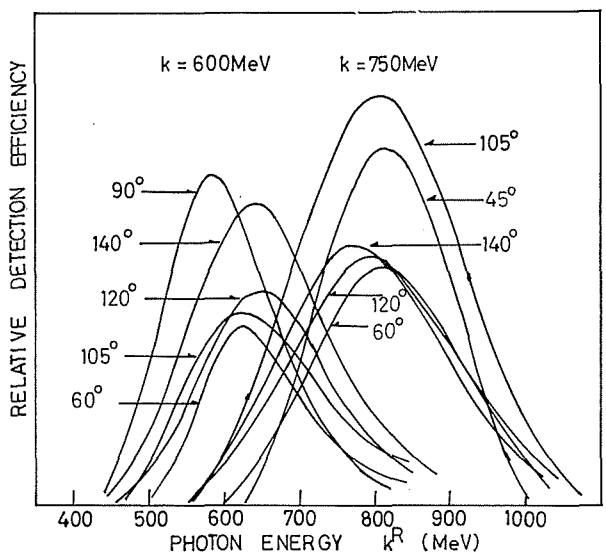

Fig. 26. Acceptance for k^R of each experimental arrangement evaluated with the Monte Carlo simulation; (a) 750 MeV, (b) 600 MeV.

600 MeV arrangements, respectively. Comparisons of the experimental data with the Monte Carlo simulation are presented in Fig. 23 for the 750 MeV–90° arrangement, as an example. In these cases, the resolution of the detectors was folded into the Monte Carlo simulation of each distribution. The results of the experiment and the simulation are in good agreement.

The momentum distribution of the initial nucleons which participate in the reaction detected with the present detection system was studied. Typical example for the 750 MeV–90° arrangement is shown in Fig. 27, where the momentum distribution, $\phi(P_{ni}^{L})$, expected from the Hulthen wave function for the deuteron is also presented. The difference between them indicates that the reaction from the target nucleons with higher momenta is rather difficult to be detected with the present experimental arrangement. As for the distributions

Table 5. Summary of resolutions. Δk^{R} and $\Delta\theta_{\pi^\circ}^{c}$ denote the energy and angular resolution of the detection system for the incident photon energy in the target-at-rest system and for the π° meson production angle, respectively.

Run (MeV)-(degree)	k^{R} (MeV)	$\theta_{\pi^\circ}^{c}$ (degree)	Δk^{R}(FWHM) (MeV)	$\Delta\theta_{\pi^\circ}^{c}$(FWHM) (degree)
500–100	530	98	34	7.0
600– 60	625	56	26	6.0
550– 90	580	86	40	7.0
600–105	625	102	54	7.0
600– 20	650	116	63	7.0
600–140	645	134	82	7.0
750– 45	800	45	34	6.0
750– 60	805	60	40	6.8
750– 90	800	90	64	7.0
750–105	795	105	78	7.0
750–120	790	120	88	7.0
750–140	770	140	109	7.0

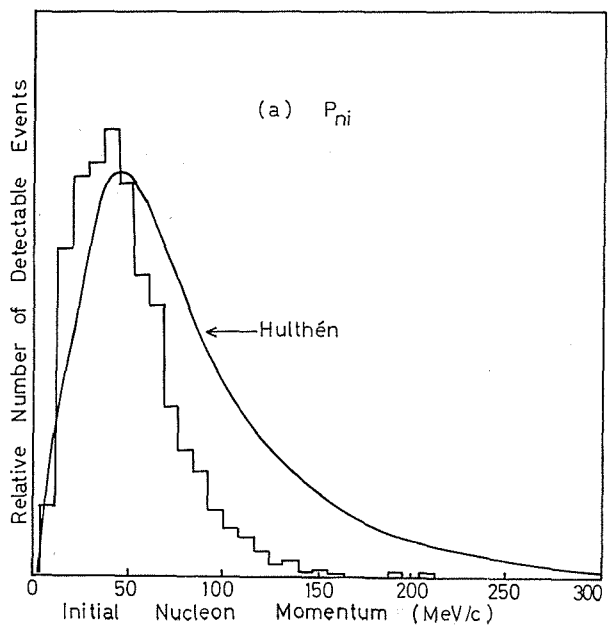

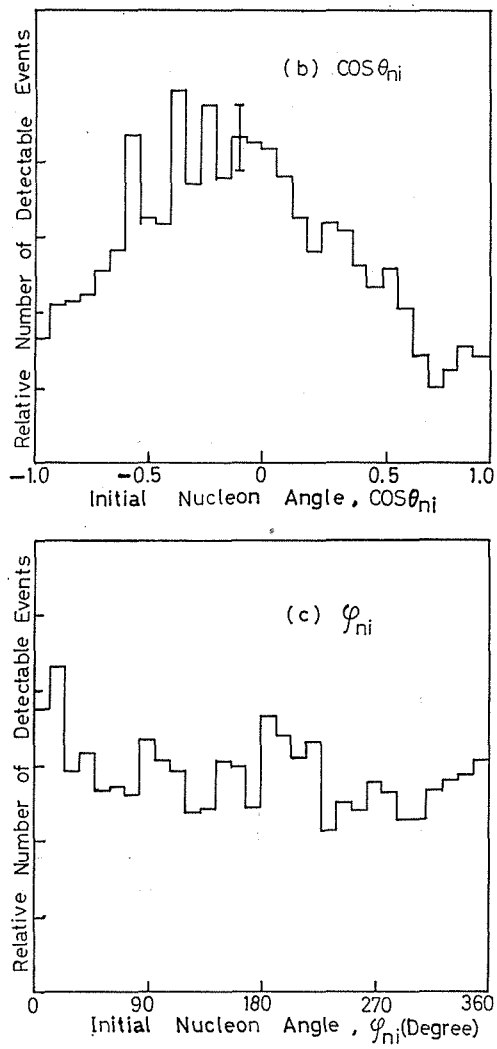

Fig. 27. Typical momentum and angular distribution of target nucleons responsible to the π° meson-nucleon councidence events; (a) P_{ni}, where the distribution expected from the Hulthen wave function for the deuteron is presented by the solid line, (b) $\cos\theta_{ni}$ and (c) φ_{ni}.

of the θ^L_{ni} and φ^L_{ni}, some deviations from the uniform distributions can be seen. These indicate that the reaction with the target nucleons moving along the perpendicular direction to the beam line can be detected efficiently.

The resolutions of the present detection system for the incident photon energy and for the π° production angle were evaluated from the distributions of variables $(k'^R-k^R)/k^R$ and $(\theta'^c_{\pi^\circ}-\theta^c_{\pi^\circ})$ in the above simulations, respectively, where k'^R and $\theta'^c_{\pi^\circ}$ represent the quantities calculated by taking account of the resolution of the detectors. The resolutions for all arrangements are presented in Table 5. The results show that the angular resolutions are almost constant for every arrangement, $\Delta\theta^c_{\pi^\circ}\simeq 3.5^\circ$. On the other hand, in the arrangements of the large π° angles, the energy of the π° meson decreases and consequently

the energy of the recoil nucleon increases. Therefore Δk^R becomes larger as the π° angle increases.

VI Experimental Results

VI–1 *Differential cross sections*

The differential cross sections were measured at 12 experimental arrangements for the processes $\gamma+p\to\pi^\circ+p$ and $\gamma+n\to\pi^\circ+n$. The mean values of the differential cross sections integrated over k^R and $\theta^c_{\pi^\circ}$ were obtained from the counter data only;

$$\overline{\frac{d\sigma}{d\Omega^c_{\pi^\circ}}(k^R,\theta^c_{\pi^\circ})}=\frac{\int_{k_{min}}^{k_{max}}Y(k^R)dk^R}{\int_{k_{min}}^{k_{max}}M(k^R)dk^R}\,, \tag{37}$$

where k_{min} and k_{max} denote the minimum and maximum values of k^R in the k^R-distribution. These counter results are summarized in Table 6.

Table 6. Differential cross sections obtained from the counter data. k^R denotes the incident photon energy in the target at rest system and $\theta^c_{\pi^\circ}$, the π° production angle in the c.m. system. Δk^R and $\Delta\theta^c_{\pi^\circ}$ are the energy and angular spread given by the half-width at half-maximum, respectively.

Run (MeV)-(degree)	$k^R\pm\Delta k^R$ (MeV)	$\theta^c_{\pi^\circ}\pm\Delta\theta^c_{\pi^\circ}$ (degree)	Yield (events/1KMU)		Geometrical detection efficiency ($\times10^{-7}$)	$d\sigma/d\Omega$ (μb/sterad.)	
			$\gamma p\to\pi^\circ p$	$\gamma n\to\pi^\circ n$		$\gamma p\to\pi^\circ p$	$\gamma n\to\pi^\circ n$
500–100	530±95	98±6	64.7	13.7	23.2	4.72±0.47	6.46±0.71
600–60	625±75	56±6	——	——	12.5	——	——
550–90	580±80	86±5	52.2	11.5	22.9	3.36±0.30	4.80±0.48
600–105	625±105	102±6	59.8	10.6	22.5	3.95±0.40	4.58±0.46
600–120	650±100	116±6	33.1	7.58	19.7	3.01±0.30	4.48±0.44
600–140	645±105	134±6	24.1	5.22	21.6	2.30±0.25	3.19±0.38
750–45	800±105	45±5	4.80	1.73	7.90	1.64±0.11	1.69±0.22
750–60	805±117	60±5	31.5	4.55	19.8	2.70±0.22	2.44±0.21
750–90	800±125	90±6	79.9	11.0	40.9	3.48±0.28	3.14±0.30
750–105	795±130	105±6	76.3	12.2	48.6	2.90±0.26	3.12±0.32
750–120	790±130	120±7	48.0	8.40	36.6	2.64±0.24	2.88±0.32
750–140	770±130	140±7	15.28	3.67	23.5	1.57±0.16	2.16±0.26
600–105–H	610±100	102±5	144.0	——	56.6	3.80±0.38	——
750–105–H	775±125	105±5	165.6	——	115.7	2.64±0.24	——

Energy dependences of the differential cross sections $d\sigma/d\Omega(k^R)$ were obtained from the analysis of the spark chamber data. The absolute values were normalized to the counter data in order to exclude the systematic errors in the measurement on the spark chamber films. At the energy regions where the data from two experimental arrangements overlapped each other, the weighted means were adopted for the final results. The values obtained from both tails of the k^R-distributions are less reliable because of the poor statistics and of the inaccuracy of background subtractions. Therefore, the data from the regions where the yields were smaller than 1/3 of its maximum value were excluded. The results are summarized in Table 7. The values were obtained at the photon energy intervals of 50 MeV except for

Table 7. Summary of results on the differential cross sections for the processes $\gamma+p\to\pi^\circ+p$ and $\gamma+n\to\pi^\circ+n$. k^R is the incident photon energy in the target-at-rest system and $\theta^c_{\pi^\circ}$ is the π° production angle in the c.m. system. Combined values of the statistical and systematic errors are shown.

k^R (MeV)	$\theta^c_{\pi^\circ}$ (degree)	$\frac{d\sigma}{d\Omega}(\gamma+p\to\pi^\circ+p)$ (μb/sterad.)	$\frac{d\sigma}{d\Omega}(\gamma+n\to\pi^\circ+n)$ (μb/sterad.)
755±25	45.0±3.0	2.03±0.29	2.12±0.38
805±25	46.0±3.0	2.25±0.29	2.13±0.38
855±25	46.5±3.0	1.64±0.20	1.24±0.29
705±25	59.0±3.4	3.50±0.38	3.00±0.50
755±25	60.0±3.4	4.22±0.40	3.82±0.50
805±25	61.0±3.4	2.88±0.29	2.32±0.33
855±25	61.5±3.4	1.76±0.20	1.86±0.29
555±25	85.5±3.5	3.44±0.38	5.03±0.71
605±25	86.0±3.5	3.14±0.34	2.94±0.49
655±25	87.0±3.5	3.14±0.37	3.38±0.49
705±25	90.0±3.5	4.45±0.49	4.00±0.63
755±25	88.0±3.5	4.40±0.49	3.70±0.55
805±25	89.0±3.5	3.56±0.38	3.61±0.54
855±25	92.0±3.5	2.55±0.29	1.41±0.27
905±25	95.0±3.5	2.04±0.26	1.45±0.33
455±25	97.0±3.5	9.40±1.33	8.05±2.12
505±25	99.0±3.5	4.38±0.54	4.68±0.82
555±25	101.0±3.5	4.46±0.57	5.95±1.01
555±25	102.0±3.5	4.85±0.63	6.47±1.10
605±25	103.0±3.5	4.01±0.50	3.13±0.60
655±25	102.0±3.5	3.52±0.39	4.03±0.58
705±25	104.5±3.5	3.15±0.35	4.04±0.56
755±25	106.0±3.5	3.85±0.43	3.68±0.51
805±25	108.0±3.5	3.42±0.40	2.73±0.40
855±25	109.5±3.5	2.95±0.37	2.78±0.42
905±25	111.0±3.5	2.38±0.35	1.74±0.35
555±25	114.0±3.5	4.36±0.60	8.40±1.68
605±25	116.0±3.5	3.45±0.37	4.72±0.91
655±25	116.5±3.5	2.72±0.32	3.66±0.55
705±25	118.5±3.5	2.60±0.28	2.79±0.43
755±25	120.5±3.5	2.77±0.31	3.04±0.45
805±25	121.0±3.5	2.49±0.29	2.04±0.37
855±25	123.0±3.5	2.45±0.30	2.04±0.38
905±25	125.0±3.5	1.89±0.26	2.13±0.39
510±50	130.5±3.5	3.01±0.47	5.52±1.42
600±40	133.0±3.5	1.73±0.24	3.87±0.78
650±50	134.5±3.5	1.48±0.22	1.86±0.63
690±50	137.5±3.5	1.70±0.25	2.54±0.53
750±50	140.0±3.5	1.50±0.19	2.20±0.42
790±50	140.5±3.5	2.22±0.34	3.12±0.78
850±50	142.0±3.5	1.50±0.19	1.91±0.39
900±50	143.0±3.5	1.96±0.29	2.55±0.68

the 140° measurement. The π° c.m. angles varied with the photon energy in each experimental arrangement. Angular resolutions were estimated to be about ±3.5° in the center of mass system when the spark chamber data were used.

VI–2 *Errors*

The errors in evaluating the differential cross section (considered as standard deviations) are conveniently grouped into following two categories;

1. Errors which are common for all experimental arrangements.
   a. photon beam intensity, $N(k^L)$ 3%
   b. target thickness and density, n_T 1%
   c. effictive solid angle of two photon detectors 6%
2. Errors which depend on the experimental arrangement.
   a. counting statistics 7~15%
   b. photon detection efficiencies of Cerenkov counters 1~5%
   c. photon absorption efficiencies 4%
   d. recoil nucleon detection efficiency, 1~5% (for protons) 4~7% (for neutrons)

The errors for each arrangement are given in Table 8. The systematic errors for the deuterium target runs (the errors except for 2–a) amounted to 8~11% and 9~12% for the differential cross sections of the processes $\gamma+p\rightarrow\pi^\circ+p$ and $\gamma+n\rightarrow\pi^\circ+n$, respectively.

Table 8. Systematic errors. In this table only the errors which depend on the experimental arrangement are listed. Quadrutic sum of systematic errors was obtained by combining these with other constant systematic errors.

Experimental arrangement	(2–b) Error of the photon detection efficiency	(2–d) Error of the recoil nucleon detection efficiency		Quadrutic sum of systematic errors	
		proton	neutron	$\gamma+p\rightarrow\pi^\circ+p$	$\gamma+n\rightarrow\pi^\circ+n$
500 MeV–100°	6%	2%	4%	10%	11%
600 MeV–60°	2%	4%	4%	9%	9%
550 MeV–90°	4%	2%	4%	9%	10%
600 MeV–105°	5%	2%	4%	10%	10%
600 MeV–120°	6%	2%	5%	10%	11%
600 MeV–140°	7%	2%	6%	11%	12%
750 MeV–45°	2%	5%	5%	10%	10%
750 MeV–60°	2%	2%	4%	8%	9%
750 MeV–90°	2%	2%	4%	8%	9%
750 MeV–105°	3%	2%	5%	9%	10%
750 MeV–120°	4%	2%	6%	9%	11%
750 MeV–140°	6%	3%	7%	10%	12%

VI–3 *Discussions on the deuterium target effect*

As a free neutron target could not be realized, the bound neutrons in the deuteron nucleus were utilized. Using the deuterium as a neutron target, the following effects must be taken into account: (1) the kinematical complications from the internal neutron momentum and (2) the dynamical effects such as the final state interaction, the Glauber effect and the Pauli principle.

In this paper, the spectator model was used for the derivation of the differential cross sections. In this model, the incident photon interacts with only one nucleon, and the other nucleon, the spectator nucleon, does not participate to the reaction. The validity of the

spectator model for high energy photon interactions has been established with the cloud and bubble chamber experiments[2,33] for the process $\gamma+d\to\pi^-+p+p_s$, in which the spectator protons could be observed. In this experiment, the Hulthen wave function was used for the deuteron. A choice of the deuteron wave function seems to give a small effect on the cross section compared with the experimental accuracy.

Corrections from the second effects were not included in the final results because all these corrections were estimated to be smaller than 5%. Final state interactions were evaluated by Chappilier[34] and Sumi[35]. In these calculations, π° mesons were treated as real particles. From these calculations it was found that the maximum effects were estimated to be about 5% in the present experiment. Pauli principle plays no role in the π° photoproduction from the deuteron, but in the charged pion photoproduction has some effects on the cross sections at small momentum transfers.

These deuterium target effects were checked experimentally for the process $\gamma+p\to\pi^++n$ by Neugebauer *et al.*[2]. They measured the π^+ yield from the deuterium target and from the hydrogen target. Their results show that the ratio,

$$R^+=\frac{\frac{d\sigma}{d\Omega}(\gamma+p\to\pi^++n,\ D)}{\frac{d\sigma}{d\Omega}(\gamma+p\to\pi^++n,\ H)} \tag{38}$$

(where D and H denote the deuterium and hydrogen target, respectively) was 0.95~1.00 for photon energies of 600 MeV 1000 MeV and at the π^+ c.m. angles larger than 40° except for small angles below 20°, where R^+ decreased to 0.77~0.84.

In this experiment, these checks were carried out by measuring the differential cross sections for the process $\gamma+p\to\pi^\circ+p$ with the deuterium target and with the hydrogen target as follows;

$$R^\circ=\frac{\frac{d\sigma}{d\Omega}(\gamma+p\to\pi^\circ+p,\ D)}{\frac{d\sigma}{d\Omega}(\gamma+p\to\pi^\circ+p,\ H)}\,. \tag{39}$$

These values were measured at 750 MeV–105° and 600 MeV–105° arrangements and the results are listed in Table 6. The results show that R° is equal to unity within the experimental accuracy.

If we assume that the deuterium target effects for the process $\gamma+n\to\pi^\circ+n$ are the same for the process $\gamma+p\to\pi^\circ+p$, the differential cross sections for the process $\gamma+n\to\pi^\circ+n$ from the free neutron target can be written as follows;

$$\begin{aligned}\frac{d\sigma}{d\Omega}(\gamma+n\to\pi^\circ+n,\ n)&=\frac{\frac{d\sigma}{d\Omega}(\gamma+n\to\pi^\circ+n,\ n)}{\frac{d\sigma}{d\Omega}(\gamma+n\to\pi^\circ+n,\ D)}\cdot\frac{d\sigma}{d\Omega}(\gamma+n\to\pi^\circ+n,\ D)\\&=\frac{\frac{d\sigma}{d\Omega}(\gamma+p\to\pi^\circ+p,\ H)}{\frac{d\sigma}{d\Omega}(\gamma+p\to\pi^\circ+p,\ D)}\cdot\frac{d\sigma}{d\Omega}(\gamma+n\to\pi^\circ+n,\ D)\\&\simeq\frac{d\sigma}{d\Omega}(\gamma+n\to\pi^\circ+n,\ D)\,.\end{aligned} \tag{40}$$

VII Discussions on the Results

The experimental results on the differential cross sections for the processes $\gamma+p\to\pi^\circ+p$ and $\gamma+n\to\pi^\circ+n$ are shown in Fig. 28 and Fig. 29. The data for the process $\gamma+p\to\pi^\circ+p$ at other laboratories are also presented in comparison with our data. At a first glance the results show that the excitation and the angular distribution of cross sections for the process $\gamma+n\to\pi^\circ+n$ have similar shapes with those for the process $\gamma+p\to\pi^\circ+p$. As for the detailed features, some trends can be pointed out. At lower energies, the differential cross sections for the process $\gamma+n\to\pi^\circ+n$ are somewhat larger than those for the process $\gamma+p\to\pi^\circ+p$. The data at low energies and at high energies are less accurate because of the poor counting statistics.

In these figures, the results of partial wave analyses by Yamaki[17], Walker[20], and Proia and Sebastiani[19] are presented by the dot-dashed, solid and dashed lines, respectively. For the process $\gamma+p\to\pi^\circ+p$ only the Walker's curve is shown. The other analyses also fit the data on the process $\gamma+p\to\pi^\circ+p$.

a) Yamaki's analysis[17]

In his analysis of the neutral pion photoproduction, six multipole amplitudes were taken into consideration; E_{0+}, M_{1-}, E_{1+}, M_{1+}, E_{2-} and M_{2-}. For E_{0+}, the C.G.L.N amplitude was adopted, and M_{1+} and M_{1-} amplitudes were formulated according to the Chew-Low theory. E_{1+} amplitude was neglected. For E_{2-} and M_{2-}, the phenomenological forms were assumed and their coupling parameter C was determined from the χ^2-test of the data on the process $\gamma+p\to\pi^\circ+p$.

The differential cross sections for the process $\gamma+n\to\pi^\circ+n$ were directly calculated with the parameters obtained from the analysis of the process $\gamma+p\to\pi^\circ+p$ with the following assumptions; (1) $E^S_{2-}=M^S_{2-}=0$ and (2) $M^S_{1-}=0$. His results are shown in Fig. 29. Characteristic features of his prediction are the asymmetry of angular distributions around 90° and rather large cross sections at backward angles for the process $\gamma+n\to\pi^\circ+n$. In this experiment these features were not found. In general, absolute values of the measured cross sections are small compared with his predictions.

b) Walker's analysis[20]

In Walker's analysis, the photoproduction amplitude consists of three separate contributions; (1) Born term, (2) resonance term, and (3) background term. The resonance term was assumed to be described adequately by a Breit-Wigner function;

$$A(W)=A(W_0)\left(\frac{k_0\ q_0}{k\ q}\right)^{1/2}\frac{W_0\Gamma^{1/2}\,\Gamma_\gamma^{1/2}}{s_0-s-iW_0\Gamma}, \tag{41}$$

where

$$\Gamma=\Gamma_0\left(\frac{q}{q_0}\right)^{2l+1}\left(\frac{q_0^2+X^2}{q^2+X^2}\right)^{l}, \tag{42}$$

$$\Gamma_\gamma=\Gamma_0\left(\frac{k}{k_0}\right)^{2j_\gamma}\left(\frac{k_0^2+X^2}{k^2+X^2}\right)^{j_\gamma}, \tag{43}$$

where W_0 is the "mass" of the resonance, and k_0, q_0, s_0 are the values of k, q, and s at the resonance energy $W=W_0$, respectively. A resonance is described by the parameters W_0, Γ_0, $A(W_0)$, l, j_γ, and X. $A(W_0)$ is the parameter which can be determined from the experimental data. The background amplitudes for low angular momentum states $J=\frac{1}{2}$, $\frac{3}{2}$ and $\frac{5}{2}$

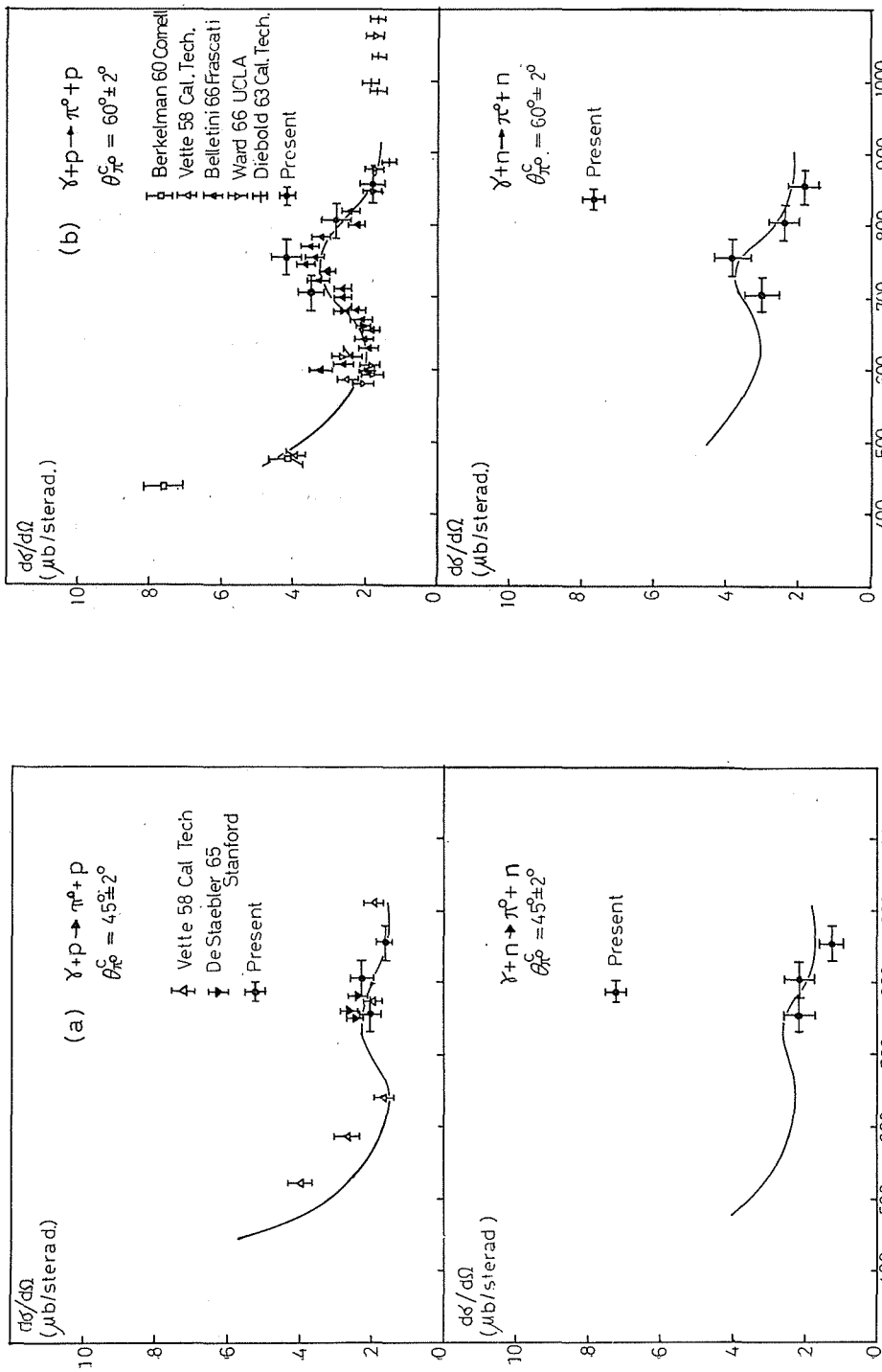

Fig. 28 (a), (b). Energy dependence of the differential cross sections for the processes $\gamma+p\rightarrow\pi^{\circ}+p$ and $\gamma+n\rightarrow\pi^{\circ}+n$. (a) $\theta^{*}_{\pi^{\circ}}=45^{\circ}$, (b) $\theta^{*}_{\pi^{\circ}}=60^{\circ}$ The solid curves show the calculations by Walker.[20] As for the previous data on the process $\gamma+p\rightarrow\pi^{\circ}+p$, see ref. 1.

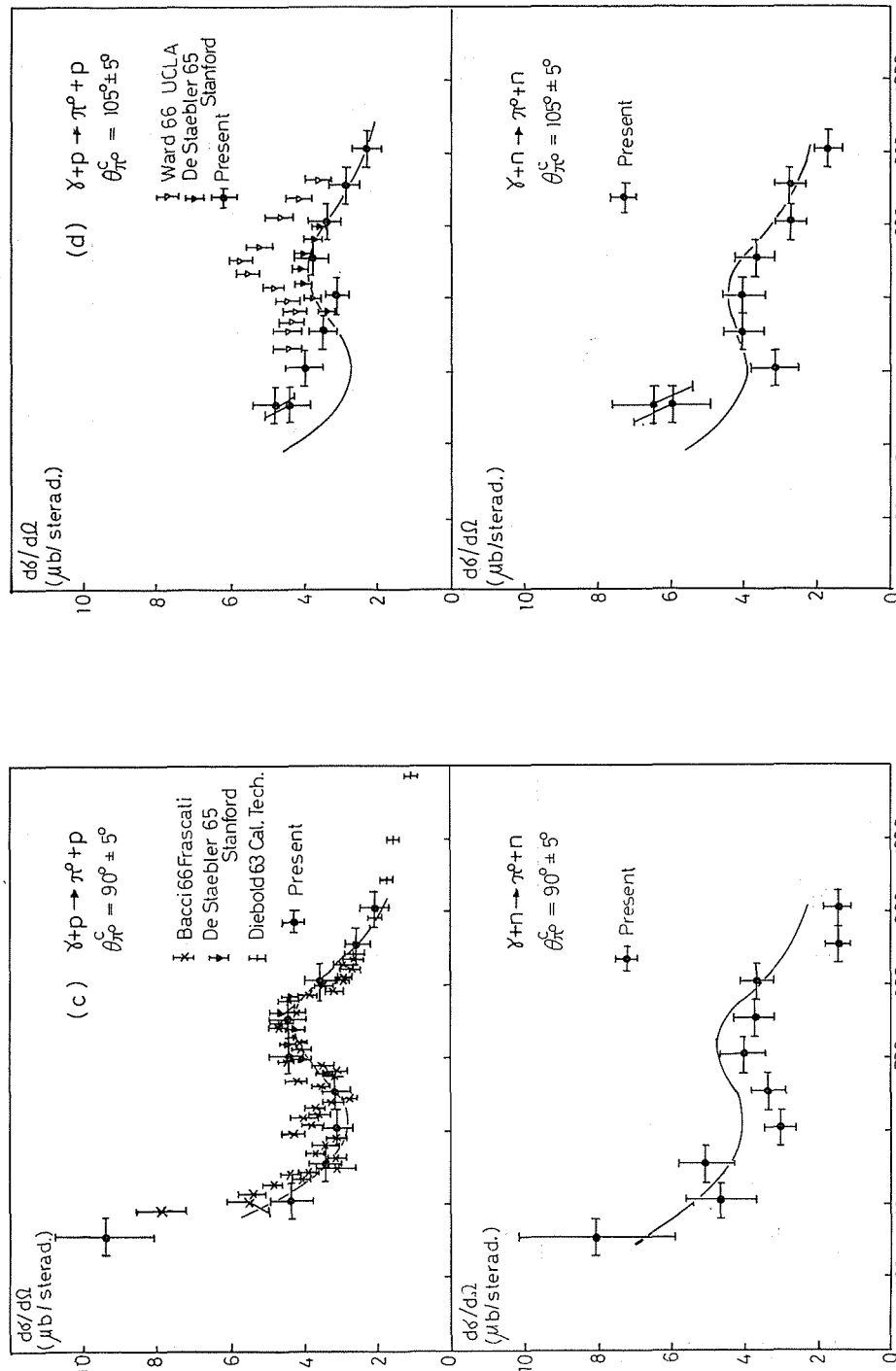

Fig. 28(c),(d). Energy dependence of the differeniial cross sections for the processes $\gamma+p\to\pi^\circ+p$ and $\gamma+n\to\pi^\circ+n$. (c) $\theta^c_{\pi^\circ}=90°$, (d) $\theta^c_{\pi^\circ}=105°$. The solid curves show the calculations by Walker.[20] As for the previous data on the process $\gamma+p\to\pi^\circ+p$, see ref. 1.

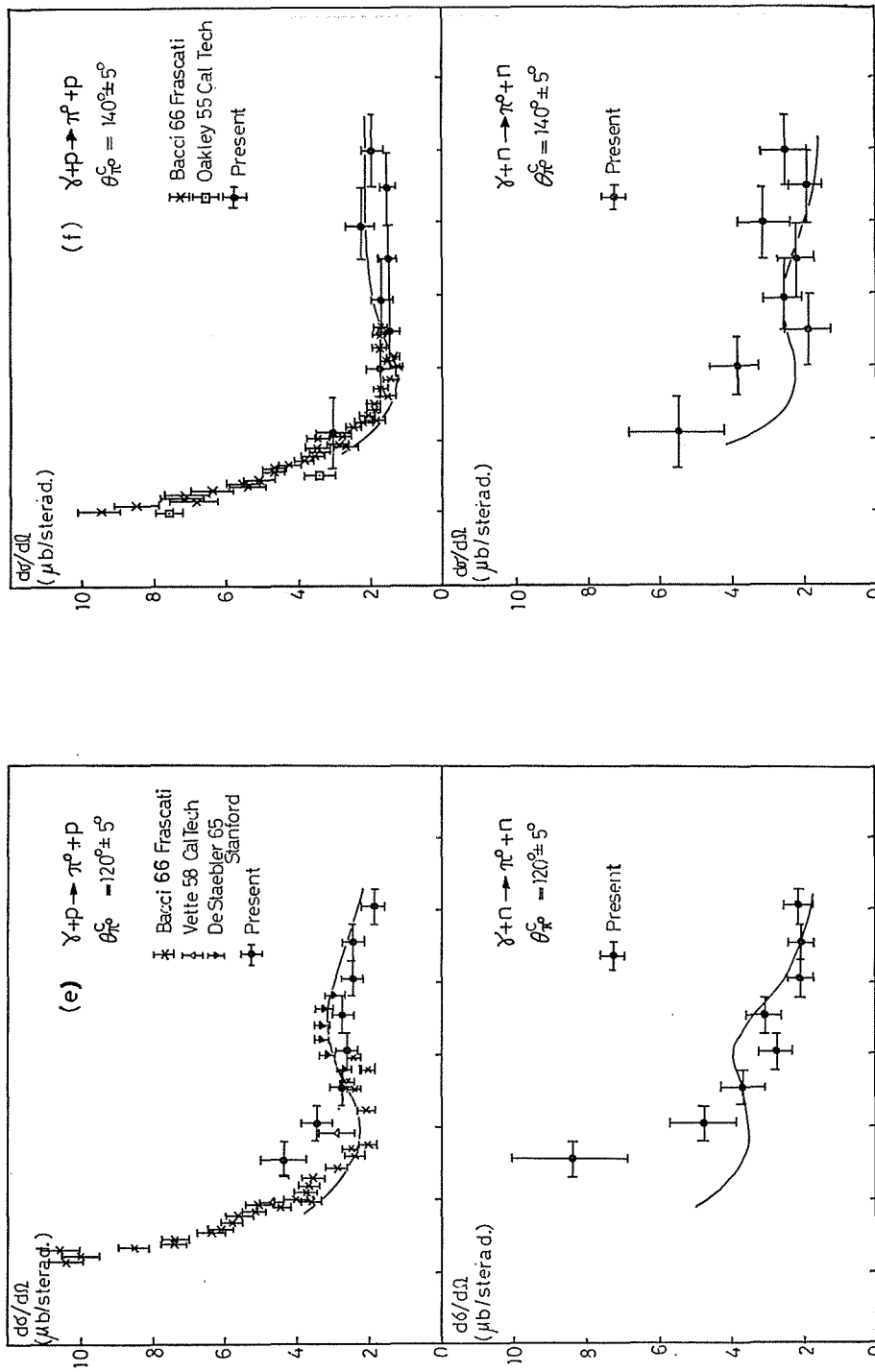

Fig. 28(e),(f). Energy dependence of the differential cross sections for the processes $\gamma+p\to\pi^0+p$ and $\gamma+n\to\pi^0+n$. (e) $\theta^c_{\pi^0}=120°$, (f) $\theta^c_{\pi^0}=140°$. The solid curves show the calculations by Walker.[210] As for the previous data on the process $\gamma+p\to\pi^0+p$, see ref. 1.

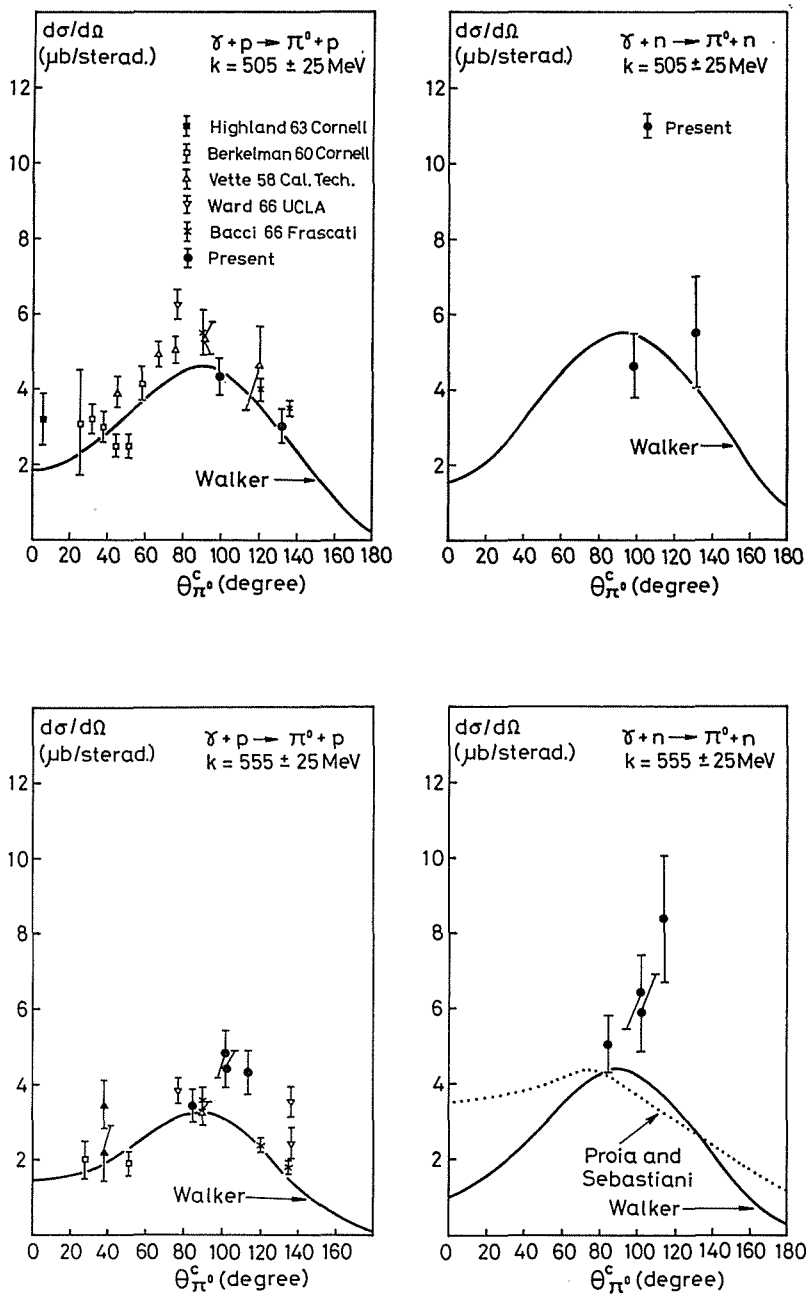

Fig. 29 (a). Differential cross sections for the processes $\gamma+p\to\pi^0+p$ and $\gamma+n\to\pi^0+n$. The solid, dot-dashed and dashed curves show the calculations by Walker[20], Yamaki[17], and Proia and Sebastiani[19]. As for the previous data on the process $\gamma+p\to\pi^0+p$, see ref. 1.

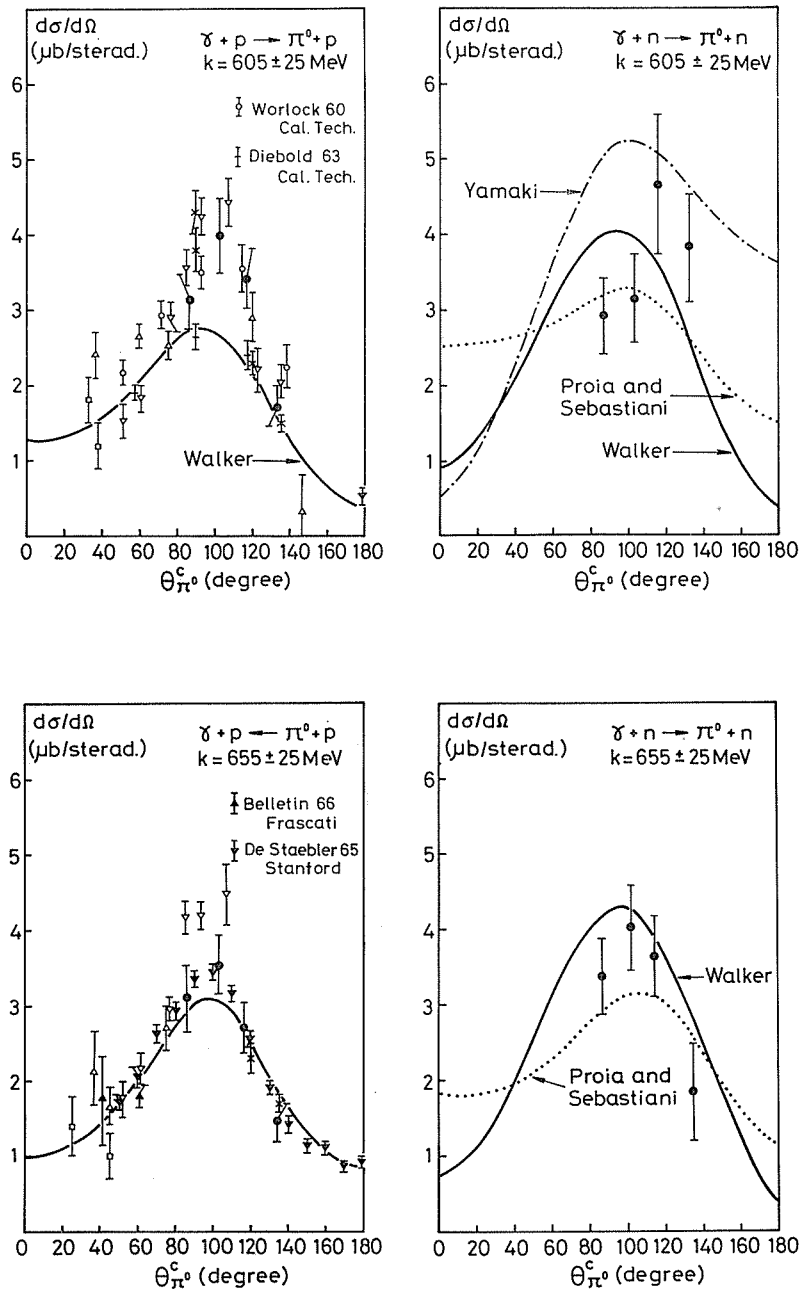

Fig. 29 (b). Differential cross sections for the processes $\gamma+p\to\pi^\circ+p$ and $\gamma+n\to\pi^\circ+n$. The solid, dot-dashed and dashed curves show the calculations by Walker[20], Yamaki[17], and Proia and Sebastiani[19]. As for the previous data on the process $\gamma+p\to\pi^\circ+p$, see ref. 1.

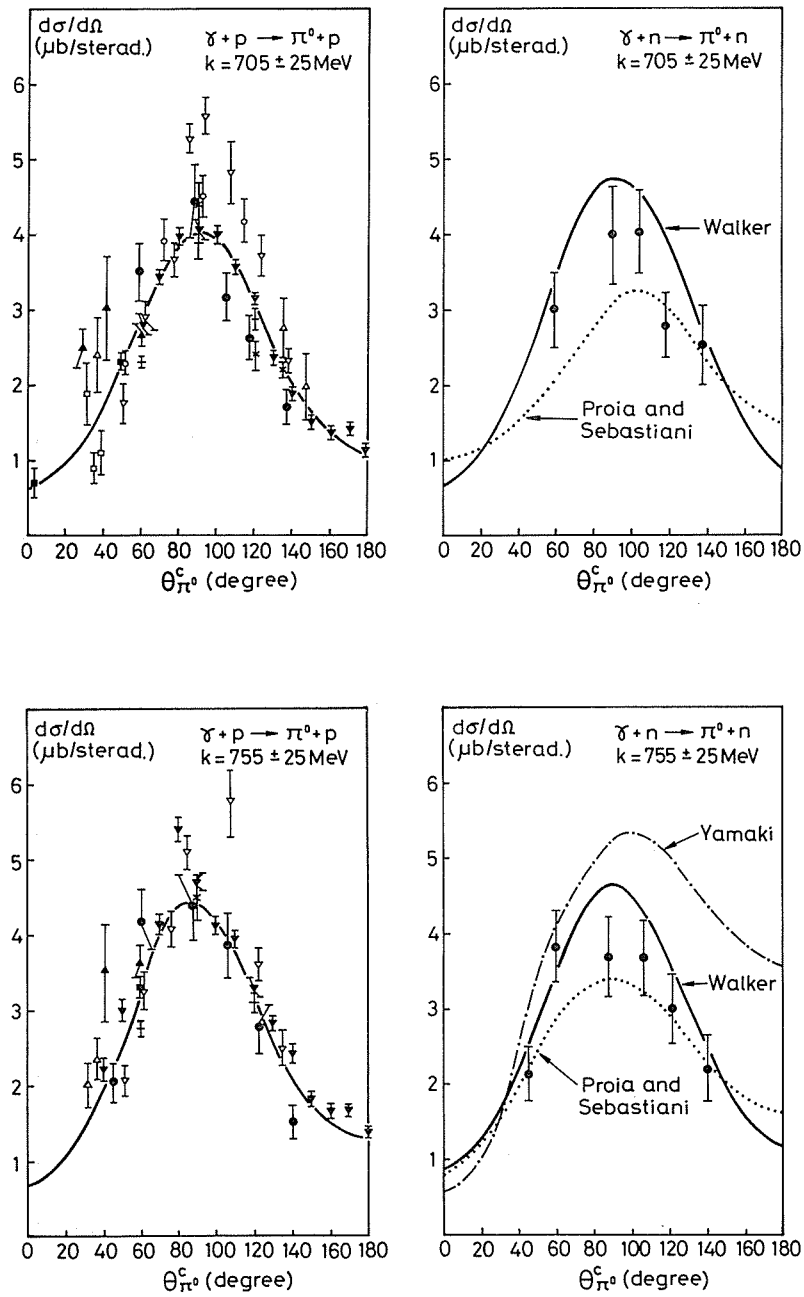

Fig. 29 (c). Differential cross sections for the processes $\gamma+p\to\pi^\circ+p$ and $\gamma+n\to\pi^\circ+n$. The solid, dot-dashed and dashed curves show the calculations by Walker[20], Yamaki[17], and Proia and Sebastiani[19]. As for the previous data on the process $\gamma+p\to\pi^\circ+p$, see ref. 1.

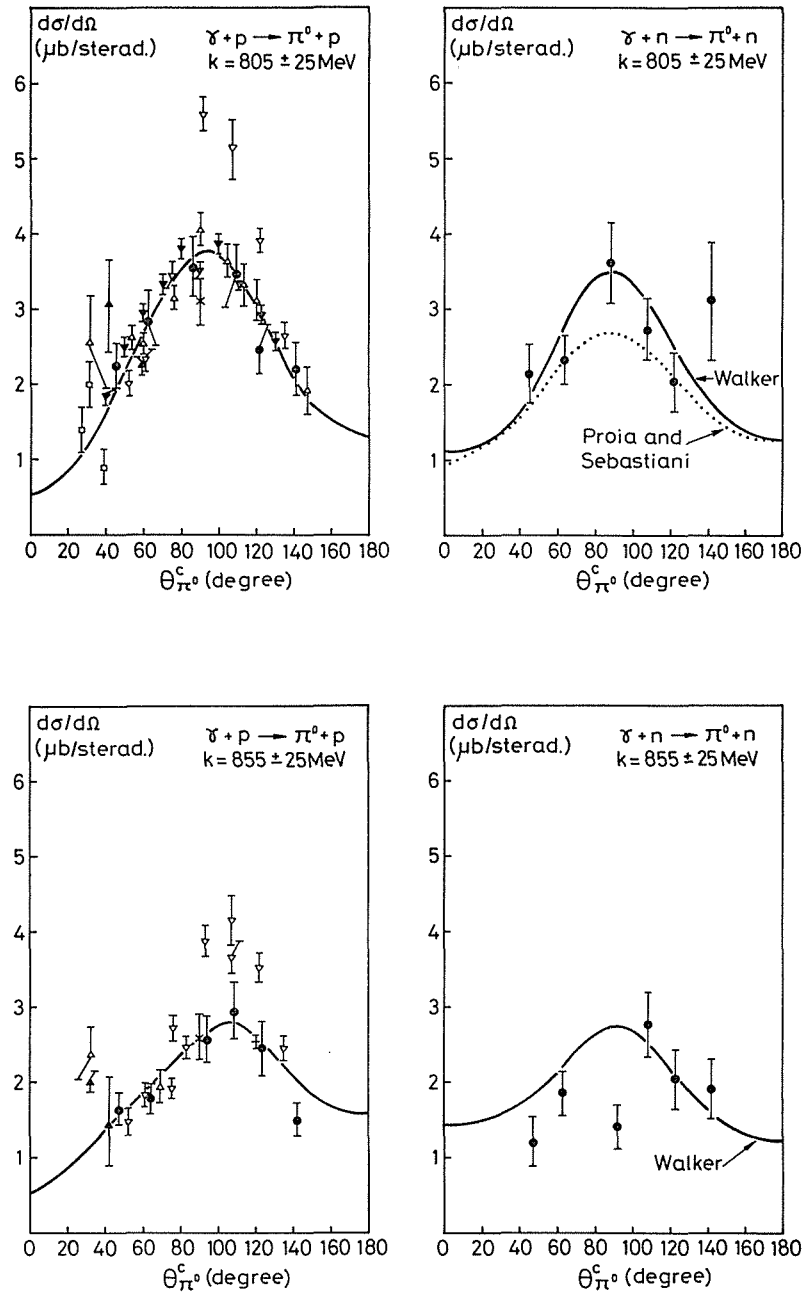

Fig. 29 (d). Differential cross sections for the processes $\gamma+p\rightarrow\pi^{\circ}+p$ and $\gamma+n\rightarrow\pi^{\circ}+n$. The solid, dot-dashed and dashed curves show the calculations by Walker[20], Yamaki[17], and Proia and Sebastiani[19]. As for the previous data on the process $\gamma+p\rightarrow\pi^{\circ}+p$, see ref. 1.

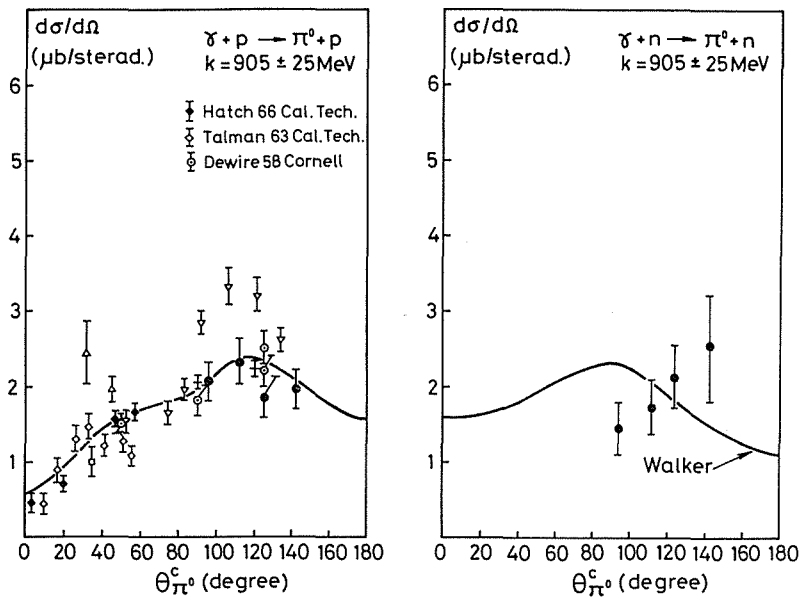

Fig. 29 (e). Differential cross sections for the processes $\gamma+p\to\pi^\circ+p$ and $\gamma+n\to\pi^\circ+n$. The solid, dot-dashed and dashed curves show the calculations by Walker[20], Yamaki[17], and Proia and Sebastiani[19]. As for the previous data on the process $\gamma+p\to\pi^\circ+p$, see ref. 1.

were included as an adjustable parameters. His criterion of success for the model was that these background terms should vary smoothly with energy. He analyzed the processes $\gamma+p\to\pi^++n$, $\gamma+p\to\pi^\circ+p$ and $\gamma+n\to\pi^-+p$. First two processes have been investigated precisely, however, as for the last process, tentative results were presented from the shortage of the experimental data. No consideration was given to the process $\gamma+n\to\pi^\circ+n$. He obtained the sets of parameters by fitting the experimental data separately for the above three processes.

By the isospin decomposition of these parameters given by Walker, we calculated the cross sections for the process $\gamma+n\to\pi^\circ+n$. The results are shown in Fig. 28 and 29 by solid lines. The agreement with the experimental data is fairly good.

c) Proia and Sebastiani's analysis[19]

Their prevision on the differential cross section for the process $\gamma+n\to\pi^\circ+n$ is based on the CDM phnomenological analysis. They analyzed the data on the process $\gamma+n\to\pi^-+p$ with the generalized isobar model, and by combining with the CDM solutions, the cross sections for the process $\gamma+n\to\pi^\circ+n$ were predicted. The data on the process $\gamma+n\to\pi^-+p$ used in their analysis were obtained from the bubble chamber experiment by AB-BHHM callaboration[2].

The results are shown in Fig. 29 by dashed lines. The experimental values are somewhat large compared with their calculations. Characteristic features of their results are; (1) clear dominance of isovector parts for $T=\frac{1}{2}$ resonance amplitudes, which is in agreement with the Walker's analysis, (2) large S_{11} and P_{11} contributions in both proton and neutron target processes.

d) Discussion

Among the above three sets of amplitudes, the Walker's amplitude resproduces the present experimental results for the process $\gamma+n\rightarrow\pi^{\circ}+n$ to some extent.

Using the experimental data for the process $\gamma+n\rightarrow\pi^{\circ}+n$ in the energy range from 650 MeV to 800 MeV, the value of $\sqrt{\chi^2 \text{ per freedom}}$ was calculated to be 2.11 with the Walker's amplitude. In order to obtain better fits to the experimental data, two resonance parameters, B_2-(D_{13}) and A_1- (P_{11}) amplitudes were varied. The minimum value of 1.38 for $\sqrt{\chi^2 \text{ per freedom}}$ was achieved, and the experimental data was well reproduced as is shown in Fig. 30.

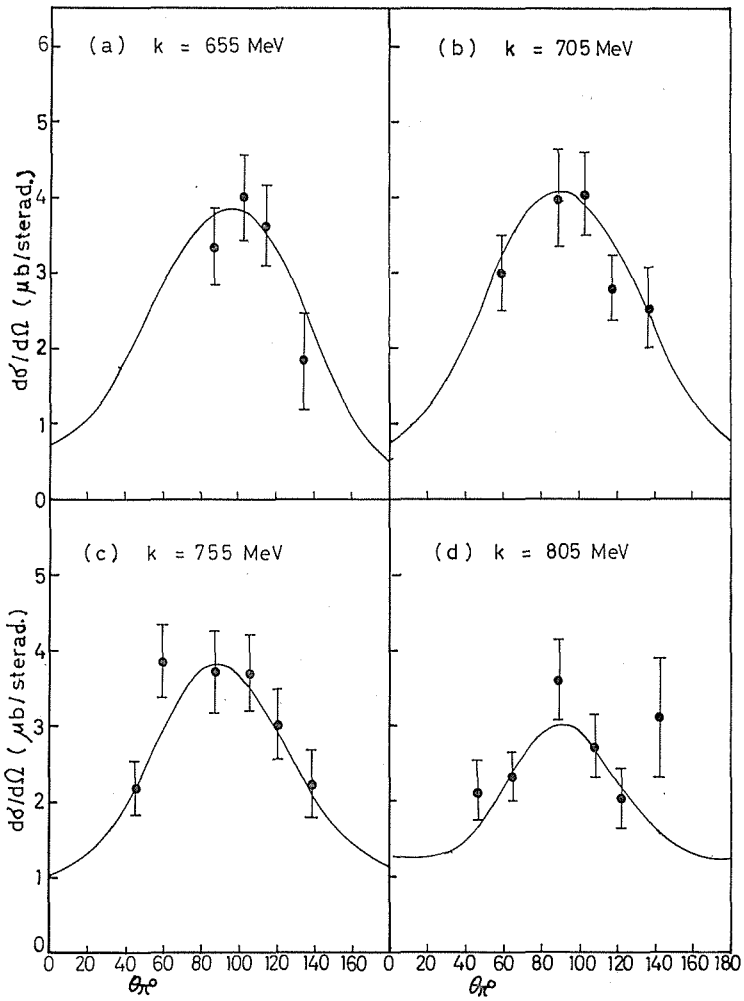

Fig. 30. Fits to the angular distribution for the process $\gamma+n\rightarrow\pi^{\circ}+n$.

The results of these analysis were summarized as follows; (1) by combining the present results with the Walker's amplitude for the process $\gamma+p\rightarrow\pi^{\circ}+p$, the ratio of the isoscalar part to the isovector part for the B_2- amplitude (D_{13} resonance) was found to be about 0.1. This indicate that the D_{13} (1520) resonance can be excited from nucleons mainly by siovector photons. (2) no remarkable enhancement of A_1- the amplitude (P_{11} resonance) was found

for the neutron target process $\gamma+\mathrm{n}\rightarrow\pi^{\circ}+\mathrm{n}$.

ACKNOWLEDGEMENT

This experiment was performed under the supervision of Prof. S. Yasumi. His guidances, suggestions and encouragements in this work are deeply acknowledged.

The immediate experimental group consisted of Prof. K. Miyake, Prof. T. Nakamura, Dr. R. Kikuchi, Mr. Y. Hemmi, Mr. S. Kobayashi, Mr. A. Sasaki, Mr. A. Maki, Mr. T. Inagaki and Mr. N. Tamura, all of whom devoted a large amount of time and effort throughout the experiment. Their excellent collaborations at the every stage of the experiment are greatly appreciated. The author is particularly indebted to Mr. Y. Hemmi for his partnership in the preparation, in the data taking and in the data anlysis of this experiment.

The success of this experiment is also attributed to the electron synchrotron crew under Prof. S. Yamaguchi of Institute for Nuclear Study, University of Tokyo. Their wonderfull operation of the electron syncrotron and their technical assistances in the construction and operation of the experimental apparatuses are much appreciated.

The success of the scanning and measuring of spark chamber pictures is due to the efforts of Miss Y. Asamoto, Miss E. Sugiyama, Miss K. Iwata, Miss Y. Ishikawa and Miss T. Murata. Their patient assistances are greatly aknowledged.

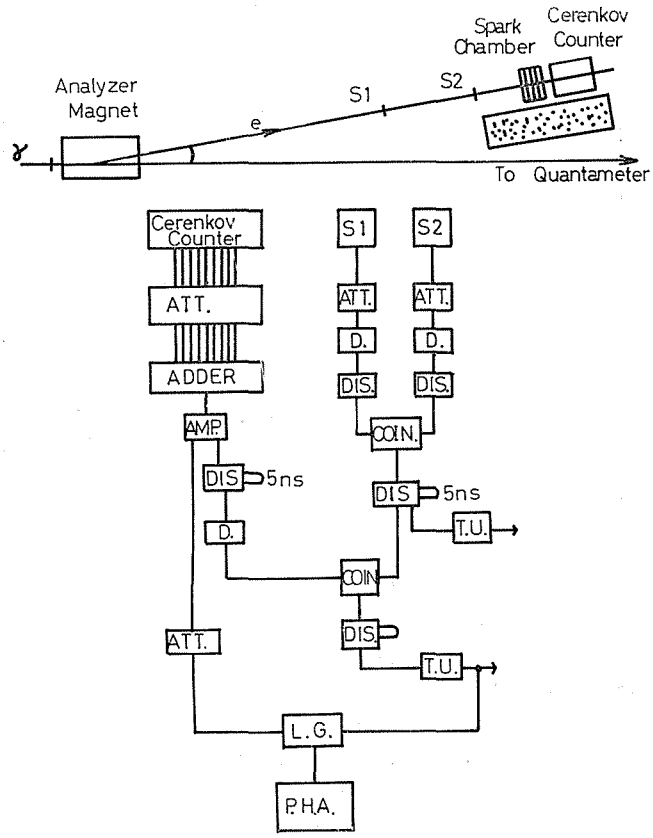

Fig. 31. Schematic diagram of the experimental arrangement for the calibration of the Cerenkov counter.

APPENDICES

A–1 *Performances of the lead glass Cerenkov counter*

The characteristic of the total absorption lead galss Cerenkov counter was measured with electron beam. Schematic diagram of the experimental arrangement is shown in Fig. 31. The electron momentum was analyzed with a magnet and a pair of small scintilation counters, S1 and S2. The momentum spread of the electron beam was 2%. Output signals from nine photomultipliers of the Cerenkov counter were added together and splitted into two parts; one for the fast coincidence ($S_1 \cdot S_2 \cdot C$) and another for the pulse height analysis. The coincidence signal ($S_1 \cdot S_2 \cdot C$) triggered the linear gate through which Cerenkov signals were fed to a PHA.

The pulse height of the Cerenkov counter is plotted as a function of electron energies in Fig. 32. A linear responce for the electron energy up to 800 MeV was obtained. The energy resolutions of these counter are shown in Fig. 33. When the lead ($2X_0$) sandwiched spark chamber was placed in front of the Cerenkov counter, the pulse height decreased and the energy resolution was worsened. These results are also shown in Fig. 32. These results indicate that the energy loss of electrons in the lead spark chamber is 50~80 MeV for the

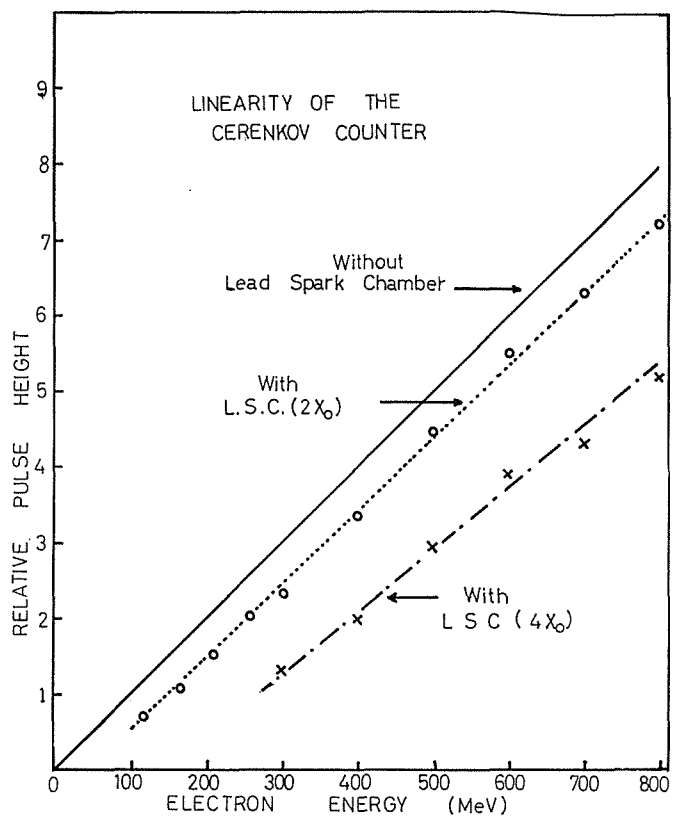

Fig. 32. Responce of the Cerenkov counter for the electron beam. The points ○ and x indicate the results when the lead spark chamber of $2X_0$ and $4X_0$ was placed in front of the lead glass, respectively.

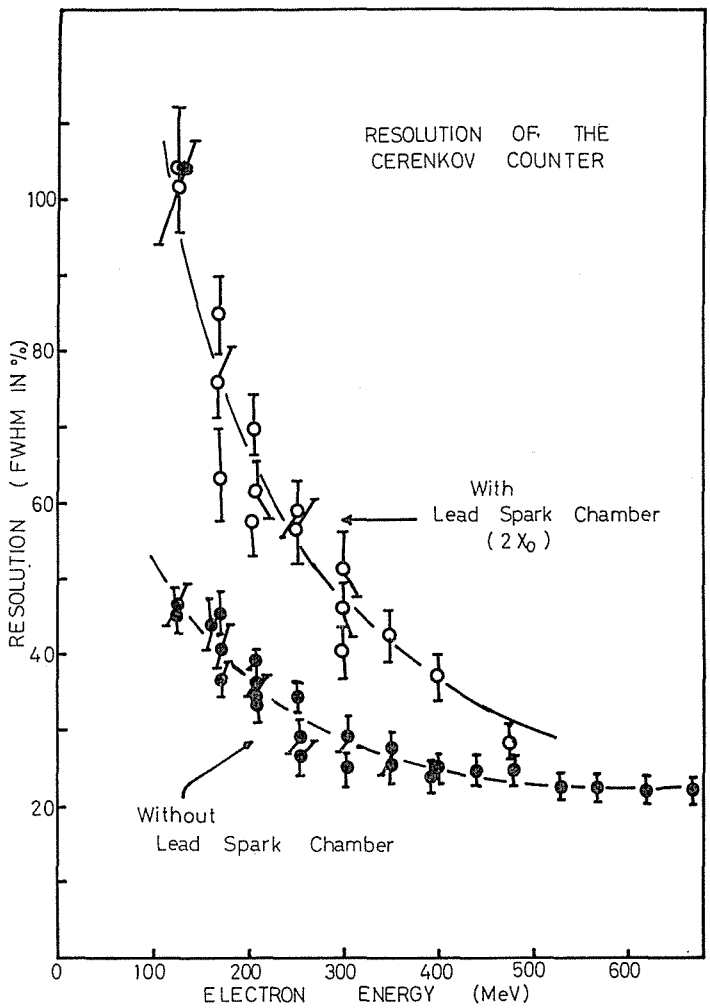

Fig. 33. Evergy resolution of the Cerenkov counter. The points ⊕ and ○ indicate the results without and with the lead spark chamber ($2X_0$), respectively.

incident electron energy of 120~800 MeV.

The energy resolutions of the Cerenkov counter for electrons can be expressed empirically as follows

$$\frac{\Delta E}{E}(\mathrm{FWHM}) \simeq \frac{4.8}{\sqrt{E}}, \tag{A.1}$$

$$\frac{\Delta E}{E}(\mathrm{FWHM}) \simeq \frac{7.0}{\sqrt{E-\Delta E}} \quad \text{(when the lead spark chamber was placed)}, \tag{A.2}$$

where ΔE is the mean energy loss in the lead spark chamber. When the lead spark chamber of $2X_0$ was placed, the resolution was worsened by a factor of about two.

A–2 *LiH absorber*

In order to reduce the background of low energy photons, an adequate absorbers must be placed in front of the photon detectors. This absorber material must attenuate low energy (1∼10 MeV) photons efficiently and must pass high energy (100∼300 MeV) photons without serious attenuation.

Total cross sections for the interaction of photons with various materials have been studied.[37] These data show that liquid hydrogen would be the best substance. However considering the difficulties of practical handling, we selected lithium hydride (LiH) as the absorber material.

As LiH reacts violently with water vapour, it must be sealed off in the closed container. The container box (200 mm × 200 mm × 10 mm in inside measurement) was made of acrylite plates (4 mm thick). Powder of LiH was packed in this box and the total thickness of LiH was measured to be 8.05 g/cm^2 as a mean (density ρ=0.805 g/cm^3). As is shown in Fig. 2, two boxes of the LiH absorber were used for each photon detector. Therefore, the total thickness of LiH and acrylite plates are as follows;

16.10 g/cm^2	for LiH
1.90 g/cm^2	for acrylite.

The total attenuation factor of absorbers for photons was calculated as a function of the photon energy. The results are shown in Fig. 34. These show that the total attenuation factor for photons with energies of 100∼300 MeV was almost constant to be 0.845.

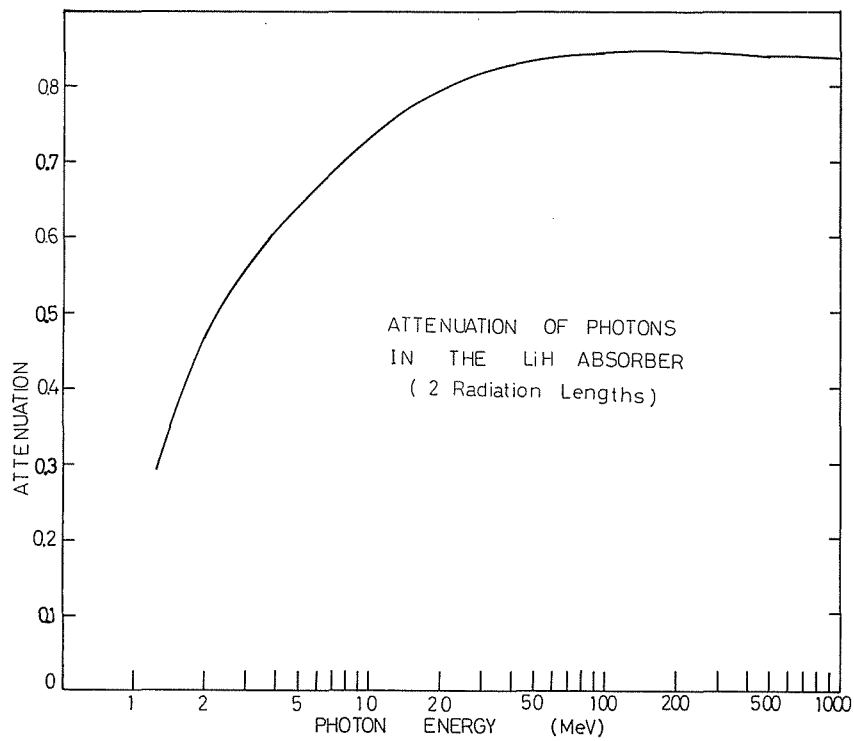

Fig. 34. Attenuation of photons versus photon energies for the LiH absorber.

A-3 *Pulse height compensation method for the time of flight measurement*

The time measurement depends on the pulse height of the start and stop signals when a conventional T.P.C. is used. To reduce the pulse height dependence of the time measurmemt several attempts such as a zero-crossing method and a fast-slow pulse height compensation method have been developed. In this experiment, the output signals from the neutron hodoscope had a continuous pulse height spectrum. Moreover the output from the Cerenkov counter had a rather broad pulse height spectrum for monoenergetic photons. Therefore to obtain the fine resolutions in the time measurement, some devices for the pulse height compensation must be used. Under the intense background signals, the zero-crossing method was not suitable for the signals of continuous pulse height. The fast-slow compensation method by Thieberger[38] was tried, however, there were some difficulties in the pulse stretching. Therefore, the following pulse height compensation method was developed.

1. Principle of the method

We represent the start and stop pulses for the T.P.C. at the input to the discriminators by

$$v_1(t)=V_1 f_1(t) \qquad \text{and}$$
$$v_2(t)=V_2 f_2(t-T)\ , \qquad (A.3)$$

where V_1 and V_2 are the amplitudes, f_1 and f_2 represent the pulse shapes which do not change on each pulse. T is the time difference between two pulses as is shown schematically in Fig. 35.

If F_1 and F_2 are the reciprocal functions of f_1 and f_2, and V_1^0 and V_2^0 are the triggering levels of the discriminators, we obtain the following values for the times t_1 and t_2 at which each discriminator is triggered;

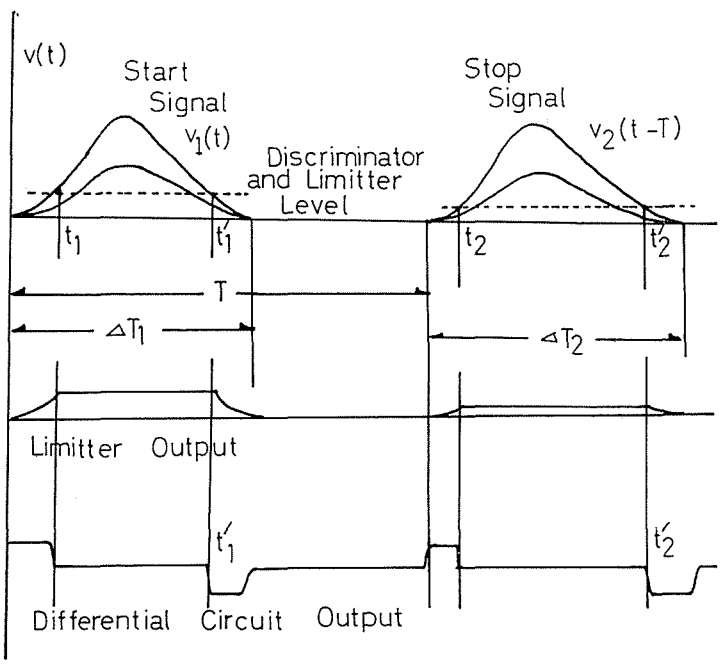

Fig. 35. Schematic diagram of the pulse height compensation method.

$$t_1=F_1\,(V_1^0/V_1)$$
$$t_2=F_2\,(V_2^0/V_2)+T \tag{A.4}$$

The output A_1 from the T.P.C. will be proportional to (t_2-t_1) and is written as follows:

$$A_1=K\,(t_2-t_1)$$
$$=K\,(T+F_2\,(V_2^0/V_2)-F_1(V_1^0/V_1)]\,, \tag{A.5}$$

where K is the constant. This expression shows that A_1 depends on the pulse amplitude V_1 and V_2.

The correction signals are obtained by the following way. The start and stop signals are splitted into two parts. The first is derived to the discriminators for the first T.P.C.. The other signals are at first fed to the limiters, whose limiting level is kept equal to the discriminator level. The output pulses from the limiter are differentiated and serve as inputs for the second T.P.C..

If we assume that the pulse shapes of the falling parts are similar to those of the rising parts as follows;

$$f_1'(t)=f_1\left(\Delta T_1-\frac{t}{c}\right)\,,$$
$$f_2''(t)=f_2\left(\Delta T_2-\frac{t}{c}-T\right)\,, \tag{A.6}$$

where ΔT_1 and ΔT_2 are the full width of each pulse and c is the time stretching constant. Then the times t_1' and t_2'' at which the negative pulses triggers the second discriminators are expressed as follows;

$$t_1'=c\,\Delta T_1-c\,F_1\,(V_1^0/V_1)\,,$$
$$t_2'=c\,\Delta T_2-c\,F_2\,(V_2^0/V_2)+T\,. \tag{A.7}$$

The output from the second T.P.C. is then given by

$$A_2=K'(t_2'-t_1')$$
$$=K'[T+c(\Delta T_2-\Delta T_1)-cF_2(V_2^0/V_2)-cF_1(V_1^0/V_1)]\,. \tag{A.8}$$

If we now attenuate A_2 by a factor $K'c/K$ and add it to A_1, we obtain;

$$A=A_1+\frac{K}{K'c}A_2$$
$$=K\left[\left(1+\frac{1}{c}\right)T+(\Delta T_2-T_1)\right]\,. \tag{A.9}$$

The amplitude dependent terms have thus been eliminated.

2. Performance

The electronic circuits used in our system are shown in the block diagram of Fig. 36. First and second T.P.C.'s are the same type of Culligan and Lipman.[39] No special care was adopted for the discriminator and the limiter. The adjustment of the discrimination level and the limiting level was made empirically.

In order to calibrate the system, a hydrogen tube light pulser was used. The light pulse was divided into two parts, and each was sent to the neutron counter and the Cerenkov counter. The output signals from each detector served as the start and stop pulses for

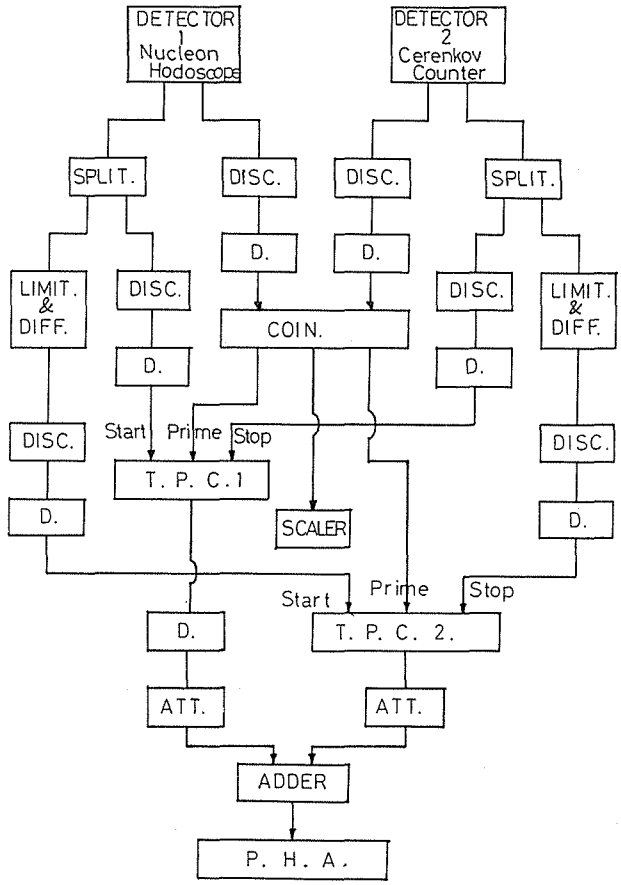

Fig. 36. Simplified block diagram of electronics for the pulse height compensation methods.

T.P.C.'s. The displacement of the peak of the T.O.F. spectrum with and without the compensation, as a function of pulse height of the neutron counter, is shown in Fig. 37. The displacement of the peak is within ± 0.5 ns over the pulse height range of about $0.1\sim 1$. As can be seen in Fig. 37, the results are slightly overcompensated. If the discriminator level, the limiter level and the output attenuator of the T.P.C. are carefully adjusted, a somewhat better correction can be obtained.

In Fig. 38, the two dimensional display between the pulse height and the T.O.F. of the nucleon in the run with the deuterium target is shown. For the proton, the linear relation between the pulse height and the T.O.F. was observed, because the pulse height of the proton depends on its kinetic energy. On the other hand for the neutron, no correlation between them was observed, because the pulse height of neutrons has a continuous spectrum. These facts show that the pulse height dependence of the T.O.F. measurement was well compensated. An example of the T.O.F. spectrum for the recoil protons and neutrons is shown in Fig. 15.

3. Some remarks

The above described method of pulse height compensation in the T.O.F. measurement can increase the resolving power when the signals of the continuous pulse height spectrum

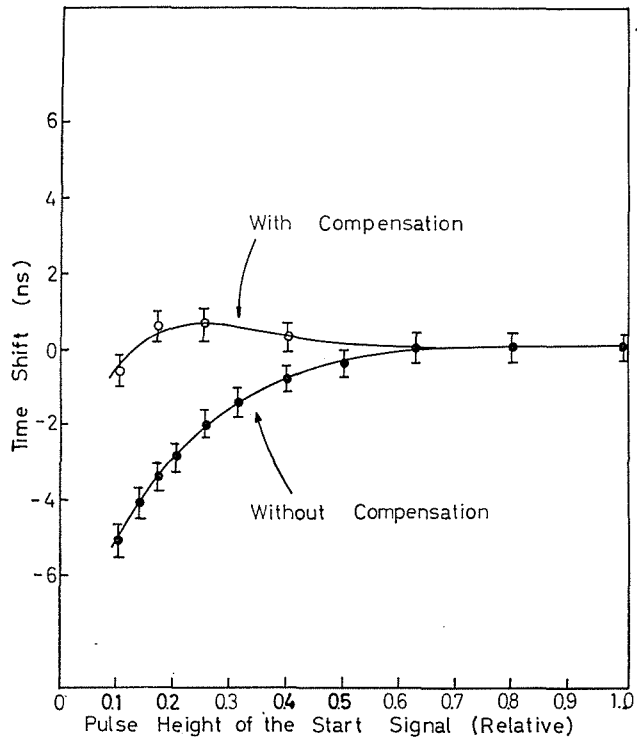

Fig. 37. Displacement of the peak of the T.O.F. spectra with and without compensation as a function of the pulse height of the start signal. The error bars indicate the resolution (FWHM) of the system for the standard light pulser (about 0.7 ns).

are used as a start or stop signals. In the case of the fast-slow method presented by Thieberger, the output amplitude depending on the flight time T is expressed as;

$$A \propto \left(1-\frac{1}{c}\right) T. \tag{A.10}$$

In our case,

$$A \propto \left(1+\frac{1}{c}\right) T, \tag{A.11}$$

where c is the pulse stretching constant for the second T.P.C. and T/c is the compensation term. The above equations show that, to obtain the large proportional constant, the constant c must be much larger than unity for Thieberger method but in our case c may be equal to unity. These facts simplify the electronic circuits.

The resolution of the T.O.F. measurement, in general, depends on other factors such as the spread of the electron transit time in the photomultipliers, the size of the scintillators, the geometry of the light guide and the stability of the electronic circuits. Final results on the time resolutions of our measurements were estimated to be about 1.0 ns (FWHM) for neutrons. The obtained results will be much improved if the fast photomultipliers and the small scintillators are used.

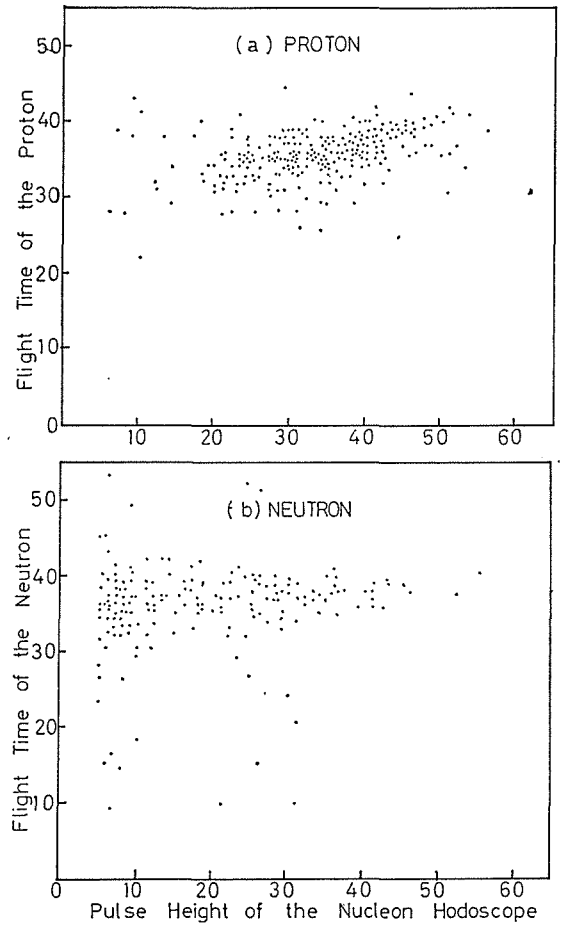

Fig. 38. Two dimensional displays of the TOF and pulse height for (a) recoil protons and (b) recoil neutrons.

A–4 *Monte Carlo calculation of the π^0 detection efficiency*

The detection efficiency of the π^0 detector was calculated with the Monte Carlo method. The detection efficiency for π^0 mesons is expressed as follows;

$$\begin{aligned}\eta_{\pi^0}(\boldsymbol{P}_{\pi^0}, \boldsymbol{x}_T)=&\eta_g(\boldsymbol{P}_{\pi^0}, \boldsymbol{x}_T)\cdot\eta_{S1}(k_1)\cdot\eta_{S2}(k_2)\\ &\times\eta_{C1}(k_{C1},X_{C1},Y_{C1})\cdot\eta_{C2}(k_{C2},X_{C2},Y_{C2})\\ &\times\eta_{H1}(k_1)\cdot\eta_{H2}(k_2)\cdot\eta_O\ ,\end{aligned}\tag{A.12}$$

where

η_g : geometical detection efficiency for π^0 mesons,

η_{S1}, η_{S2} : detection efficiency of the lead sandwiched spark chambers for photons, which is divided into the conversion effeciency and the spark chamber efficiency,

η_{C1}, η_{C2} : detection efficiency of the Cerenkov counter,

η_{H1}, η_{H2} : attenuation factor of the LiH absorber for photons,

η_0 : other factors such as the scanning efficiency,
$\boldsymbol{P}_{\pi^\circ}$: momentum and the direction of the π° meson,
$\boldsymbol{x}_T$: reaction point in the target cylinder,
k_1, k_2 : energies of photons decaying from the π° meson,
k_{C1}, k_{C2} : energies lost in the Cerenkov counters,
$X_{C1}, Y_{C1}, X_{C2}, Y_{C2}$: incident positions of decay photons on the Cerenkov counters.

Among these, η_g is a very complicated function and can not be evaluated by the analytical method. In this appendix, the detailes of the Monte Carlo calculation of the geometrical efficiency η_g are described.

The flow chart for the computer program is shown in Fig. 39.

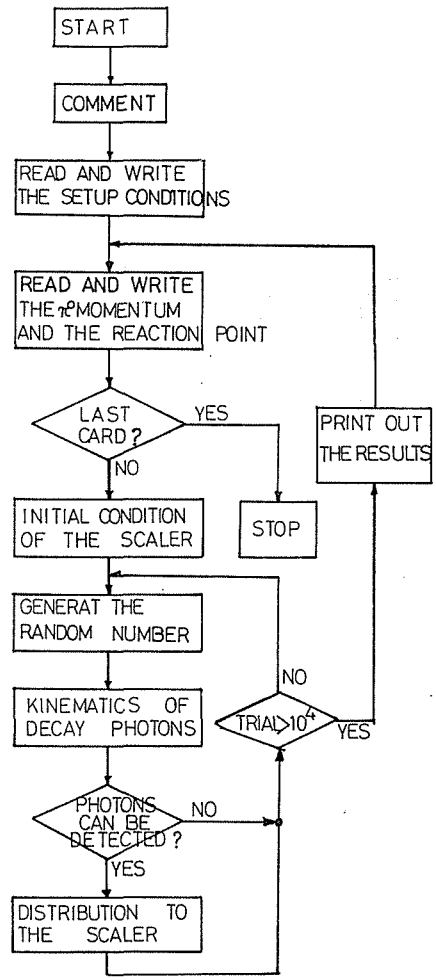

Fig. 39. Flow chart of the computer program for the Monte Carlo simulation.

1. Setup conditions of the π° detector

The coordinate axes of the lab. system are chosen as is shown in Fig. 40, where the Z_E axis is the direction of indident photon beam, $Z_E - X_E$ and $Z_E - Y_E$ are the horizontal and vertical plane, respectively.

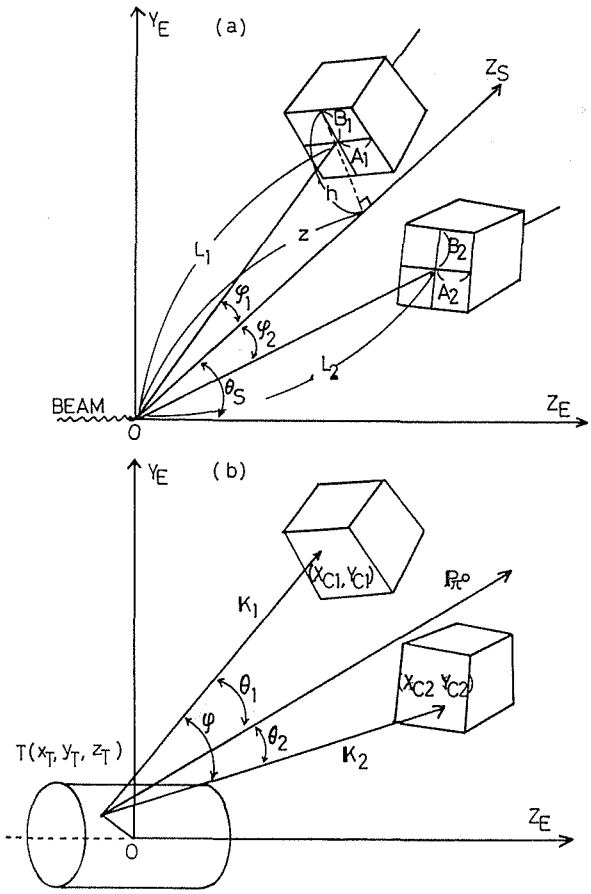

Fig. 40. Setup parameters of the π° detector.

The set up parameaters of the π° detector are summarized as follows;

L_1, L_2 : distances of the two photon detectrors from the target center.

φ_1, φ_2 : opening angles of two photon detectors from the horizontal plane.

A_1, B_1, A_2, B_2 : demensions of the two photon detectors.

θ_S : angles between the π° detector and the incident bremsstrahlung beam (Z_E−axis),

where suffices 1 and 2 denote the upper and lower photon detector, respectively. In general, as two photon detectors are placed symmetrically around the horizontal plane, the set up parameters are reduced to five parameters.

$$L=L_1=L_2$$
$$\varphi_S=\varphi_1=\varphi_2$$
$$A=A_1=A_2$$
$$B=B_1=B_2 \quad \text{and}$$
$$\theta_S\,. \tag{A.13}$$

2. Coarse selection

At first, a coarse selection whether the π° meson can be detected or not was performed under the following conditions;

a. The minimum correlation algle of two photons decaying from the π° meson must be smaller than the maximum opening angle of the photon detectors;

$$2\varphi_{\mathrm{MIN}} \leq 2\varphi_{\mathrm{SMAX}} \ , \tag{A.14}$$

where $2\varphi_{\mathrm{SMAX}}$ is the maximum opening angle of the photon detectors;

$$\varphi_{\mathrm{SMAX}} = \frac{L\cos\varphi_{\mathrm{S}} - B\sin\varphi_{\mathrm{S}}}{\sqrt{A^2+B^2+L^2}} \tag{A.15}$$

And $2\varphi_{\mathrm{MIN}}$ is the minimum correlation angle between two photons decaying from the π° meson which have the momentum of P_{π°;

$$\cos\varphi_{\mathrm{MIN}} = \frac{P_{\pi^\circ}}{\sqrt{P_{\pi^\circ}^2+\mu^2}} \ , \tag{A.16}$$

where μ is the rest mass of the π° meson.
From the eqs. A.14, A.15 and A.16, P_{π° must satisfy the following relation in order that the π° meson can be detected;

$$P_{\pi^\circ} \geq \frac{\mu}{\tan\varphi_{\mathrm{SMAX}}} \ . \tag{A.17}$$

b. The flight direction of π° mesons is also restricted by the geometry of the detectors. The π° direction $(\theta_{\pi^\circ}, \varphi_{\pi^\circ})$ described in the lab. system $(X_{\mathrm{E}}, Y_{\mathrm{E}}, Z_{\mathrm{E}})$ are transformed to the coordinates in the lab. system $(X_{\mathrm{S}}, Y_{\mathrm{S}}, Z_{\mathrm{S}})$, in which the trasformation is a rotation of θ_{S} arround the Y_{E}-axis. Then the directional cosines of the π° momentum vector, $(S_{\mathrm{x}}, S_{\mathrm{y}}, S_{\mathrm{z}})$ in the $(X_{\mathrm{S}}, Y_{\mathrm{S}}, Z_{\mathrm{S}})$ system are represented by;

$$\begin{aligned} S_{\mathrm{x}} &= \sin\theta_{\pi^\circ}\cos\varphi_{\pi^\circ}\cos\theta_{\mathrm{S}} - \cos\theta_{\pi^\circ}\sin\theta_{\mathrm{S}} \\ S_{\mathrm{y}} &= \sin\theta_{\pi^\circ}\sin\varphi_{\pi^\circ} \\ S_{\mathrm{z}} &= \sin\theta_{\pi^\circ}\cos\varphi_{\pi^\circ}\sin\theta_{\mathrm{S}} + \cos\theta\pi_{\pi^\circ}\cos\theta_{\mathrm{S}} \ . \end{aligned} \tag{A.18}$$

Moreover Z and h in Fig. 40 are expressed as follows:

$$\begin{aligned} Z &= L\cos\varphi_{\mathrm{S}} - B\sin\varphi_{\mathrm{S}} \ , \\ h &= L\sin\varphi_{\mathrm{S}} + B\cos\varphi_{\mathrm{S}} \ . \end{aligned} \tag{A.19}$$

Then in order that the π° mesons emitted from the center of the target can be detected, the following relations must be satisfied;

$$\begin{aligned} -A \leq \frac{S_{\mathrm{x}}}{S_{\mathrm{z}}} \cdot Z \leq A \ , \\ -h \leq \frac{S_{\mathrm{y}}}{S_{\mathrm{z}}} \cdot Z \leq h \ . \end{aligned} \tag{A.20}$$

3. Isotropic decay of π° mesons

The π° meson decays into two photons isotropically in the π° meson rest system. If the emission angle of a photon is denoted by $(\theta_1{}^*, \varphi_1{}^*)$ in the π° rest system, the another photon is emitted in the derection $(\theta_1{}^*+\pi, \varphi_1{}^*+\pi)$.

The flight directions of two photons in the lab. system (θ_1, φ_1) and (θ_2, φ_2) are obtained by the Lorentz transformation;

$$\cos\theta_1=\frac{\cos\theta_1^*+\beta}{1+\beta\cos\theta_1^*}\ ,$$

$$\cos\theta_2=\frac{-\cos\theta_1^*+\beta}{1-\beta\cos\theta_1^*}\ ,$$

$$\varphi_1=\varphi_1^*\ ,$$

$$\varphi_2=\varphi_1^*+\pi\ , \qquad \text{(A.21)}$$

where β is the velocity of the π° meson and the Z-axis of the lab. system is chosen to coincide with the π° flight direction. The energies of two photons are also given by

$$E_1=\frac{(1+\beta\cdot\cos\theta_1^*)}{2\sqrt{1-\beta^2}}\cdot\mu\ ,$$

$$E_2=E_{\pi^\circ}-E_1\ . \qquad \text{(A.22)}$$

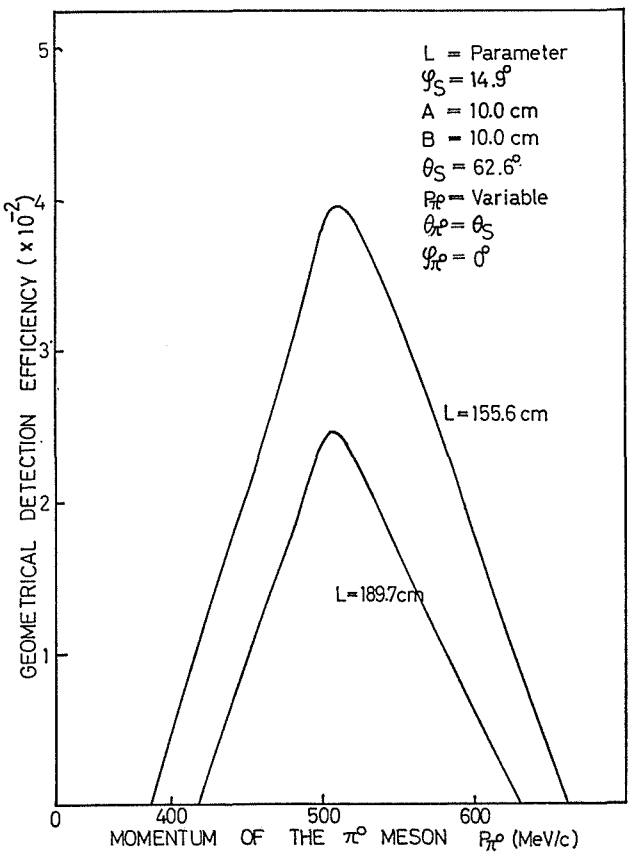

Fig. 41. Geometrical detection efficiency for π° mesons as a function of the π° momentum. The flight direction of π° mesons coincides with the center line of the detector.

To simulate the event, the random numbers on θ_1^* and φ_1^* are generated by the Monte Carlo method. In order that the two photons can be detected in coincidence with two photon detectors, the following restrictions on φ_1, therefore on φ_1^*, can be derived;

$$\pi/2-\varphi_{ACP} \leq \varphi_1 \leq \pi/2+\varphi_{ACP} \ ,$$

where

$$\tan\varphi_{ACP}=\frac{A}{L\sin\varphi_S-B\cos\varphi_S} \ . \tag{A.23}$$

From the decay angle of photons in the π° rest system, photon momentum vectors in the lab. system can be calculated.

4. Selection of events

Whether two decay photons can be detected or not with the π° detector is judged event by event. If we denote the event of which two photons can be detected by a good event, the geometrical efficiency η_g is obtained as follows;

$$\eta_g=\frac{\text{number of good events}}{\text{number of trials}}\times\text{efficiency factor} \tag{A. 24}$$

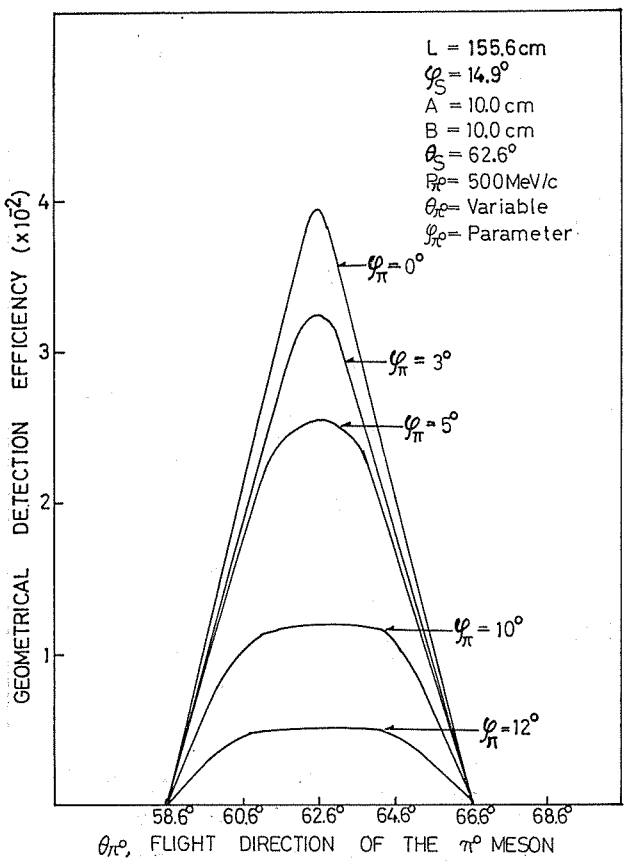

Fig. 42. Geometrical detection efficiency for π° mesons as a function of θ_{π°.

where the efficiency factor comes from the restriction on the random number of φ_1*.

5. Results

The geometrical detection efficiencies for π° mesons were calculated as a function of the π° momentum $\boldsymbol{P}_{\pi^{\circ}}$ and source point $\boldsymbol{x}_T$.

Some results are shown in Figs. 41, 42 and 43. The calculations were carried out for

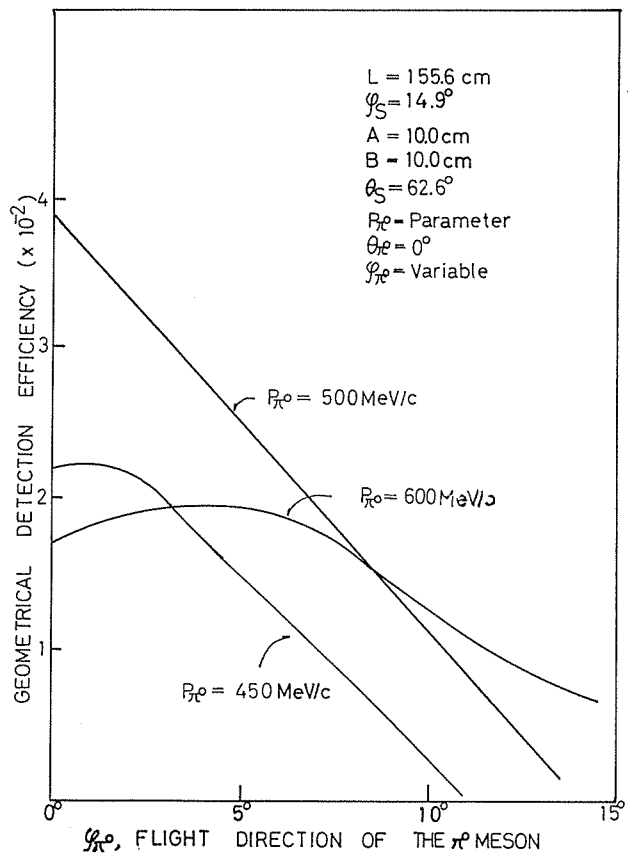

Fig. 43. Geometrical detection efficiency for π° mesons as a function of $\varphi_{\pi^{\circ}}$.

the various detector arrangements. The efficiency of the Monte Carlo simulation was $10^{-1}\sim10^{-2}$. The results were also compared with the values obtained with the graphic method by Yoshimura.[6] And the good agreement between them was obtained. In the case where the π° meson is emitted into the center line of the detector and the opening angle of the detector coincides with the minimum correlation angle, the dependence of η_g on L is expressed roughly as follows;

$$\eta_g \propto L^{-2} \ . \tag{A.25}$$

The detection efficiency is almost constant over the effective target volume and varies only about 6% in the extreme case.

A–5 *Kenematics*

As the target nucleon is moving in the deuteron, the kinematics of the photoproduction

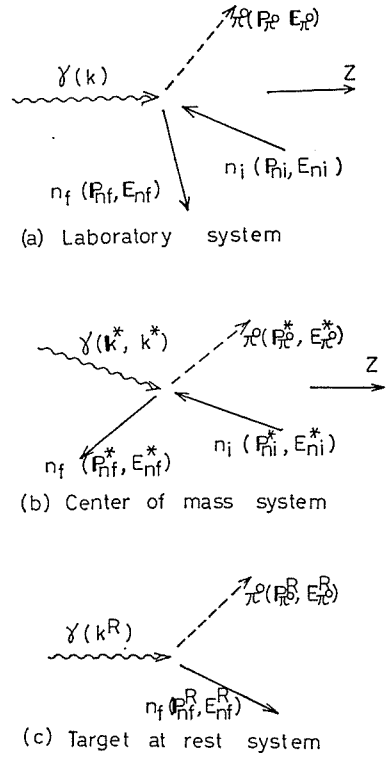

Fig. 44. Kinematical variables (a) in the laboratory system, (b) in the center of mass system and (c) in the targetat-rest system.

is complicated. Kinematical variables at the initial and final states are shown in Fig. 44 and Table 9. Four momentum vectors of the incident photon, the initial nucleon, the π° meson and the recoil nucleon are denoted by (k, k), $(\boldsymbol{P}_{\rm ni}, E_{\rm ni})$, $(\boldsymbol{P}_{\pi^\circ}, E_{\pi^\circ})$ and $(\boldsymbol{P}_{\rm nf}, E_{\rm nf})$, respectively. The upper suffices * and R denote the center of mass system and the target-at-rest system respectively. These coordinate systems are related with each other through the Lorentz trasformation. Among 16 kinematical variables in the laboratory system, four energy and momentum conservation laws and four mass relations reduce the independent variables to 8. In addition, the direction of incident photons is defined as the Z-axis in the laboratory system (two variables are fixed). Therefore, from the only six independent variables, others are all evaluated.

Table 9. Kinematical variables

	Initial state		Final state	
Particle	photon	nucleon	π° meson	nucleon
Mass	0	$M_{\rm i}$	μ	$M_{\rm f}$
Momentum	$\boldsymbol{k}$	$\boldsymbol{P}_{\rm ni}$	$\boldsymbol{P}_{\pi^\circ}$	$\boldsymbol{P}_{\rm nf}$
Energy	k	$E_{\rm ni}$	E_{π°	$E_{\rm nf}$
Total momentum	$\boldsymbol{P}_{\rm i} = \boldsymbol{k} + \boldsymbol{P}_{\rm ni}$		$\boldsymbol{P}_{\rm f} = \boldsymbol{P}_{\pi^\circ} + \boldsymbol{P}_{\rm nf}$	
Total energy	$E_{\rm i} = k + E_{\rm ni}$		$E_{\rm f} = E_{\pi^\circ} + E_{\rm nf}$	

In our experiment, the final state momenta $\boldsymbol{P}_{\pi^\circ}$ and $\boldsymbol{P}_{\mathrm{nf}}$ were measured. From these, the initial state momenta k and $\boldsymbol{P}_{\mathrm{ni}}$ can be evaluated as follows;

$$k=\frac{(\boldsymbol{P}_{\mathrm{nf}})^2-E_{\mathrm{f}}^2+M^2}{2[(\boldsymbol{P}_{\mathrm{f}})_z-E_{\mathrm{f}}]}\ , \tag{A.26}$$

$$\boldsymbol{P}_{\mathrm{ni}}=\boldsymbol{P}_{\mathrm{f}}-\boldsymbol{k}\ , \tag{A.27}$$

where $(\boldsymbol{P}_{\mathrm{f}})_z$ denotes the z-component of the momentum vector $\boldsymbol{P}_{\mathrm{f}}$. The incident photon energy $\boldsymbol{k}$ is expressed as $(0,0,k)$ when the Z-axis is chosen to coincide with the photon beam direction.

Writing the velocity of the c.m. system and the total energy in the c.m. system by;

$$\beta=\frac{\boldsymbol{P}_{\mathrm{f}}}{E_{\mathrm{f}}} \tag{A.28}$$

and

$$E^*=\sqrt{1-\beta^2}\cdot E_{\mathrm{f}}\ , \tag{A.29}$$

the π° momentum in the c.m. system can be evaluated by the Lorentz trasformation;

$$\boldsymbol{P}_{\pi^\circ}{}^*=\boldsymbol{P}_{\pi^\circ}+\frac{\boldsymbol{P}_{\mathrm{f}}}{E^*}\left[\frac{\boldsymbol{P}_{\mathrm{f}}\cdot\boldsymbol{P}_{\pi^\circ}}{E_{\mathrm{f}}+E^*}-E_{\pi^\circ}\right]\ , \tag{A.30}$$

$$\left|\boldsymbol{P}_{\pi^\circ}{}^*\right|=\frac{1}{2E^*}\left[(E^{*2}+\mu^2-M^2)-2E^*\,\mu^2\right]^{1/2}\ . \tag{A.31}$$

Also the incident photon momentum can be expressed as follows;

$$\boldsymbol{k}^*=\boldsymbol{k}+\frac{\boldsymbol{P}_{\mathrm{nf}}}{E^*}\left[\frac{\boldsymbol{P}_{\mathrm{f}}\cdot\boldsymbol{k}}{E_{\mathrm{f}}+E^*}-k\right]\ , \tag{A.32}$$

$$k^*=\frac{1}{E^*}(E_{\mathrm{f}}\cdot k-\boldsymbol{P}_{\mathrm{f}}\cdot\boldsymbol{k})\ . \tag{A.33}$$

From these relations the pion production angle in the c.m. system can be calculated as follows;

$$\cos\theta_{\pi^\circ}^{C}=\frac{\boldsymbol{P}_{\pi^\circ}{}^*\cdot\boldsymbol{k}^*}{|\boldsymbol{P}_{\pi^\circ}{}^*|\cdot k^*}\ . \tag{A.34}$$

The incident photon energy in the target-at-rest system is expressed as follows;

$$k^{\mathrm{R}}=\frac{E^{*2}-M^2}{2M}\ . \tag{A.35}$$

REFERENCES

1) J.T. Beale, S.D. Ecklund, and R.L. Walker: Report CTSL-42 (1966), California Institute of Technology, Synchrotron Laboratory.
2) G. Neugebauer, W. Woles, and R.L. Walker: Phys. Rev. **119** (1960) 1726. Aachen-Berlin-Bonn-Hamburg-Heidelberg-Munchen Collaboration, G.H. Hilbert *et al.*: Nuclear Phys. **B 8** (1968) 535. M. Beneventano *et al.*: Lett. Nuovo Cimento **1** (1969) 113.

ibid. **3** (1970) 840.
P.E. Sheffler and P.L. Walden: Phys. Rev. Letters **24** (1970) 952.
E. Lodi-Rizzini *et al.*: Lett. Nuovo Cimento **3** (1970) 697.
K. Kondo *et al.*: J. Phys. Soc. Japan **29** (1970) 13.
T. Fujii *et al.*: INS-Report-149 (1970), Institute for Nuclear Study, Univ. of Tokyo.
3) G. Cocconi and A. Silverman: Phys. Rev. **88** (1952) 1230.
4) C.R. Clinesmith, G.L. Hatch, and A.V. Tollestrup: *Proc. of the International Symposium on Electron and Photon Interactions at High Energies* (Hamburg, 1965) Vol. II, p. 245.
5) G.C. Bolon, D. Bellenger, W. Lobar, D. Luckey, L.S. Osborne, and R. Switters: *Proc of the IV International Symposium on Electron and Photon Interactions at High Energies* (Daresbury, 1969) p. 280.
6) Y. Yoshimura, S. Hatano, Y. Hemmi, R. Kikuchi, S. Kobayashi, K. Miyake, T. Nakamura, H. Okuno and S. Yasume: J. Phys. Soc. Japan **24** (1969) 1395.
Y. Yoshimura: Memoirs of the Fuculty of Science, Kyoto University, Series of Physics, Astrophysics, Geophysics and Chemistry **33** (1970) 143.
7) K.M. Watson: Phys. Rev. **85** (1952) 852, *ibid.* **95** (1954) 228.
8) M. Roos *et al.* (Particle Data Group): Phys. Letters **33 B** (1970) 1.
9) R.L. Walker: *Proc. of the IV International Symposium on Electron and Photon Interactions at High Energies* (Daresbury, 1969) p. 23.
10) A. Bietti: Phys. Rev. **142** (1966) 1258; *ibid.* **144** (1966) 1289.
11) G.F. Chew, M.D. Goldberger, F.E. Low, and Y. Nambu: Phys. Rev. **106** (1957) 1345.
12) W. Schmidt: Z. Phys. **182** (1964) 76, G. Hohler and W. Schmidt: Ann. Phys. (New York) **28** (1964) 34.
13) F.A. Berends, A. Donnachie, and D.L. Weaver: Nuclear Phys. **B 4** (1968) 54.
A. Donnachie: Phys. Letters **24 B** (1967) 420.
F.A. Berends and A. Donnachie: Phys. Letters **30 B** (1969) 555.
14) K. Kondo, T. Nishikawa, T. Suzuki, K. Takikawa and Y. Kimura: J. Phys. Soc. Japan **29** (1970) 30.
15) A.I. Sanda, and G. Shaw: Phys. Rev. Letters **24** (1970) 1310.
16) M. Gouldin and Ph. Salin: Nuovo Cemento **27** (1963) 193.
Ph. Salin: Nuovo Cimento **28** (1963) 1294.
17) T. Yamaki: Progr. theor. Phys. **38** (1967) 153.
18) Y.C. Chau, N. Dombey and R.G. Moorhouse: Phys. Rev. **163** (1967) 1632.
19) A. Proia and F. Sebastiani: Lett. Nuovo Cimento **3** (1970) 483.
20) R.L. Walker: Phys. Rev. **182** (1969) 1729.
21) R.G. Moorhouse and W.A. Rankin: Nuclear Phys. **B 23** (1970) 181.
22) K. Miyake, K. Baba, S. Hatano, H. Itoh, M. Kihara, A. Masaike, T. Makamura, M. Tamaki, S. Yasumi and Y. Yoshimura, J. Phys. Soc. Japan **20** (1965) 1749.
T. Nakamura, S. Hatano, Y. Hemmi, H. Itoh, M. Kihara, S. Kobayashi, K. Miyake, H. Okuno, T. Yamaki, S. Yasumi and Y. Yoshimura: J. Phys. Soc. Japan **24** (1968) 698.
23) Y. Hemmi, T. Inagaki, R. Kikuchi, A. Maki, K. Miyake, T. Nakamura, A. Sasaki, N. Tamura, S. Yasumi and H. Okuno: Phys. Letters **32 B** (1970) 137.
Y. Hemmi: to be published in Memoirs of the Fuculty of Science, Kyoto University.
24) Y. Hemmi, R. Kikuchi, S. Kobayashi, K. Miyake, T. Nakamura, H. Okuno, S. Yasumi and Y. Yoshimura: Nuclear Instrum. and Methods **56** (1967) 213.
25) K. Takamatsu *et al.*: private communication.
26) T. Miyachi *et al.*: INS-TH-66 (1970), Institute for Nuclear Study, Univ. of Tokyo.
27) T. Kitami, H. Okuno and K. Takamatsu: INS-TH-61 (1969), Institute for Nuclear Study, Univ. of Tokyo.
28) D.B. Chelton and D.B. Mann: UCRL-3421, Cryogenic Data Book, Univ. of California, Radiation Laboratory.
29) L. Tau: Nuclear Instrum. and Methods **34** (1965) 352.
30) R.J. Kurtz: UCRL-11339 (1964), University of California.
31) D.C. Crabb, J.C. Mcewen, E.G. Auld and A. Langsford: Nuclear Instrum. and Methods

48 (1967) 87.
32) J.C. Young, J.L. Romerok, F.P. Brady and J.R. Morales: Nuclear Instrum. and Methods **68** (1969) 333.
33) D.F. Crawford and H. Messel: Nuclear Phys. **61** (1965) 145.
34) D.H. White, R.M. Schectman and B.M. Chasan: Phys. Rev. **120** (1960) 614.
35) J. Chappilier: Phys. Rev. **99** (1955) 254.
36) Y. Sumi: Progr. theor. Phys., **41** (1969) 1227.
37) E.L. Hart and D.H. White: Rev. sci. Instrum. **31** (1960) 33.
38) P. Thieberger: Nuclear Instrum. and Methods **44** (1966) 349.
39) G. Culligan and N.H. Lipman: Rev. sci. Instrum. **31** (1960) 1209.